Experimental Insights into Subglacial Mechanics

By

Dougal D. O. Hansen

A dissertation submitted in partial fulfillment

of the requirements for the degree of

Doctor of

Philosophy

(Geoscience)

at the

UNIVERSITY OF WISCONSIN-MADISON

2022

Date of final oral examination: 6/25/2022

The dissertation is approved by the following members of the Final Oral Committee: Lucas Zoet, Associate Professor, Geoscience
Shaun Marcott, Associate Professor, Geoscience
Kurt Feigl, Professor, Geoscience
Hiroki Sone, Assistant Professor, Geological Engineering

Dedication

To Iza,

for your love, patience, and constant support

and to our cat Sake,

Meow

ACKNOWEDGEMENTS

Luke, thank you for being an exceptional mentor. You have always fostered a welcoming environment within our group, quickly responded to questions, provided thoughtful edits and insight, and encouraged us to think big. I greatly appreciate the wealth of opportunities for personal and professional growth that you facilitated during my years at UW-Madison. I look forward to continuing this relationship in the coming years as we bring the next projects to fruition. Additionally, I thank my committee members (Kurt Feigl, Hiroki Sone, and Shaun Marcott) for their valuable insight and discussions over the years, as they helped steer my thesis in a tractable direction, and Colin Meyer, Alan Rempel, Anders Damsgaard, and Brent Minchew for their support, encouragement, illuminating discussions and scientific acumen.

I very grateful to Peter Sobel and Neal Lord for their invaluable support and insight with these experiments. Not only did they design and build the laboratory systems that made this work possible, but they frequently provided critical advice that enabled the success of our projects. Our group and department are incredibly fortunate to collaborate with them and bring our (sometimes wild) ideas to life.

The rock mechanics group at UW-Madison led by Hiroki Sone has been extremely accommodating to me throughout the years. Maciej Trzeciak, Charlotte Bate, Kate Condon, Ben Jahnke, and Porter Garst have all invested time and energy into my projects—teaching me how to use equipment and prepare samples, supervising my experiments, and operating their machines. Similarly, the Wisconsin Geological and Natural History Survey has provided support for numerous projects. J Elmo Rawling, III, Stef Dodge, and Chelsea Volpano have analyzed the

grain size distribution of sediments and fault gouge on numerous occasions, and Grace Graham provided training and support for hydrologic stream surveys.

To my immediate family (Cindy, Eric and Omar), I appreciate all the support and encouragement you have given me throughout this long academic journey. It means a lot. I also extend a special to thanks to my dad for assisting Nate and I on our field campaigns to Bench Glacier. He transported us to and from Valdez on multiple occasions, showed us the cool local spots (e.g. Thai food truck at Glenallen!), offered advice and equipment, and allowed us to repeatedly cover his lawn in gear as we packed and repacked in preparation for the glacier. These trips enriched the overall experience and saved us a lot of money and headache.

I greatly appreciate my cohort in the Surface Processes group whom I've had the pleasure of knowing these past few years (Nate Stevens, Chelsea Volpano, Stef Dodge, Ian Mcbrearty, Jacob Woodard, Collin Rolland, Jeremy Brooks, Natasha Morgan-Witts, Francisca Nuñez). All of the lively discussions, frequent collaborations, fieldwork shenanigans, jokes, and patient help made my experience here memorable and exciting. I could not ask for a more engaged, inclusive, and talented group of peers. To Lillian Smith and Lindsay Summers, thank you for your exceptional work on the glacial abrasion project and Bench seismic dataset, respectively.

Finally, to my wife, Iza, I could not have accomplished this without you! You had a front row seat to the whole experience, which was not always smooth, and you never wavered in your support as we navigated these years together. I love you and am grateful for everything.

My studies at UW-Madison were supported in part by the Wisconsin Alumni Research Foundation and funding from the National Science Foundation (NSF-2017185, NSF-2013987, and NSF-2048315).

Table of Contents

Dedication i

Acknowledgements ii

Abstract vi

Overview viii

Chapter 1. Characterizing sediment flux of deforming glacier beds 1

Abstract 1

1 Introduction 3

2 Materials and Methods 7
2.1 Experimental design 7
2.2 Variable sliding velocity and effective stress 9
2.3 Digital Image Correlation 11
2.4 Estimating shear band thickness 15
2.5 Estimating sediment flux 17

3 Results 18
3.1 Shear band morphology 18
3.2 Influence of effective stress on sediment flux 20
3.3 Influence of slip speed on sediment flux 22
3.4 Ice-till coupling 24

4 Discussion 25
4.1 Shallow deformation in subglacial environments 25
4.2 Double-valued sediment flux at increasing effective stress 25
4.2 Ice-till coupling scales velocity dependent sediment flux 28
4.4 Glaciological implications 31

5 Conclusions 33

Acknowledgments 34

References 35

Chapter 2. Experimental constraints on subglacial rock friction 46

Abstract 46

1 Introduction 47
1.1 The effect of premelt on debris-bed contact forces 51

2 Methods 54

3 Results 57

3.1 Friction tests **60**

3.2 Temperature gradients in the ice **62**

3.3 Basal melt rate and effective stress influence the contact force **63**

4 Discussion **66**

4. 1 Model Comparisons **69**

4.2 The effect of temperature gradients on debris-bed drag **74**

4.3 Contribution of effective stress to debris-bed contact forces **75**

5 Conclusions **79**

Acknowledgments **80**

References **81**

Appendix **87**

Premelting effects on debris-bed contact forces **87**

Chapter 3. Subglacial abrasion rates scale with rock-frictional energy during basal slip **91**

Abstract **91**

1 Introduction **92**

2 Methods **95**

3 Results **97**

4 Discussion and conclusions **102**

Acknowledgments **104**

References **105**

Supplemental material **109**

S1 Direct Shear: experimental protocol **109**

S2 Ring shear: experimental protocol **111**

S3 Measuring abraded volume **114**

S4 Grain size distribution of rock gouge **117**

S5 Surface Fracture Energy **119**

CCNBD tests methods **120**

Estimating Young's Modulus and Poisson's ratio **122**

S6. Estimating E_a and associated uncertainty with a Monte Carlo Markov Chain approach **125**

ABSTRACT

Ice mass flux for many of the world's most active glaciers and ice streams arises from glacier ice slipping over a lubricated substrate of bedrock or sediment. The physics controlling this "basal slip" fundamentally control glacier dynamics and drive the rapid denudation of alpine landscapes. Many tenets in the field of glaciology related to these processes currently lack a solid empirical basis, yet are repeatedly applied in theory or models of glacier dynamics and landscape evolution. Until these assumptions are thoroughly vetted, our understanding of glacier processes will be limited by this uncertainty. Here, I employ a range of novel experimental techniques to test long-standing hypotheses regarding the mechanics of hard and soft glacier beds. Specifically, I focus on questions related to subglacial rock friction/abrasion, which increases drag at the ice-bed interface and drives erosion, and till deformation, a first-order control on glacier dynamics, landform generation, and erosion. In chapter one, I constrain the influence of two fundamental controls on subglacial sediment transport during till deformation—effective stress and slip speed. Using digital image correlation to quantify flux rates from a photographic time series of the till bed, I demonstrate that sediment flux scales nearly linearly with slip speed when ice and till are coupled, but flux varies non-monotonically with effective stress, contradicting prior assumptions. In chapter two, I test the physical controls on subglacial friction for hard-bedded glaciers under drained hydrologic conditions. Using a modified direct shear apparatus with an insulating sample chamber, I slid limestone slabs beneath slabs of debris-laden ice and assessed the relative influence of basal melt rate, effective stress and ice temperature on frictional resistance during slip. I show that basal drag scales linearly with both melt rate and normal stress in these experiments, confirming they influence the contact force in the presence of efficient drainage.

Lastly in chapter three, I examine physical expression of rock-on-rock friction at glacier beds—subglacial abrasion—and use these observations to test the validity of the basal-power abrasion law. Using a novel cryogenic ring shear device in concert with the direct shear, I produce the most realistic simulations of abrasion to date, quantify abrasion rates from high-resolution 3D models of the eroded surface, and then quantify the energy dissipated through this process during slip. For planar rock beds, I show that i) average rock-frictional shear force at the bed increases linearly with abraded volume (per unit area), ii) abrasion rates increase linearly with basal power, and iii) percentage of slip energy expended through abrasion is one–two orders of magnitude lower than prior estimates.

Overview

The evolution of glaciers in response to a warming climate is increasingly at the forefront of public discourse (IPCC, 2022). Over the past few decades, accelerated climate change has increased ice mass flux from glaciers and continental ice sheets to the oceans, directly contributing to global sea level rise (Rignot et al, 2008; Zemp et. al 2019; Christian et al., 2022). It has also affected the dynamics of smaller alpine glaciers (Stevens et al., 2022) and likely is accelerating erosion and sediment output in alpine environments (Koppes and Hallet, 2002; Koppes and Hallet, 2006; William and Koppes, 2019)—among other myriad other ramifications (Carrivick and Tweed, 2016; Ultee et al., 2021). Many of these processes, including those stated here, are intrinsically linked through the process of "basal slip," in which glacier ice slides over bedrock or sediment beds, aided by pressurized water (Zoet and Iverson, 2020; Henalow et al., 2021). Thus, to a first order, the mechanics controlling slip therefore set the pace and magnitude of large-scale environmental change, including rapid denudation of mountain ranges or global sea level rise.

It is critical to understand the physics that control glacier slip to evaluate its impact on ice sheet stability under future warming scenarios (Gladstone et al., 2017). This process, however, remains a major source of uncertainty in predictive glacier or ice sheet models (Ritz et al., 2015), since many of the fundamental physics lack a sound empirical basis. In this dissertation, I employ a range of novel experimental techniques to interrogate hypotheses related to the mechanics of hard and soft glacier beds. Specifically, I focus on questions related to subglacial rock friction/abrasion, which increases drag at the ice-bed interface and drives erosion, and till deformation, a first-order control on glacier dynamics, landform generation, and erosion. My

results are presented here as three papers, which comprise the three chapters of this dissertation. Of these chapters, one and two are published in peer-reviewed journals, and the third has been submitted for review.

In chapter one, published in the *Journal of Geophysical Research: Earth Surface* (Hansen and Zoet, 2022), I investigate the influence of two hypothesized controls on subglacial sediment deformation (i.e. "till"). When glacier ice slips over till beds, it exerts traction at the interface, which mobilizes grains if the driving stress exceeds sediment strength at grain contacts (Zoet and Iverson, 2020). This flux creates bedforms that impact glacier dynamics (Alley et al., 2007; Bart et al., 2017; Simpkins et al., 2018), and it affects erosion by evacuating sediment from the system or shielding bedrock from wear in areas of net deposition (Alley et al., 2019). Two longstanding assumptions regarding this process are that sediment flux increases with i) ice velocity (due to faster strain rates) and ii) effective normal stress (due to deeper deformation Iverson and Iverson, 2001). I tested the effects of these two parameters by conducting soft-bed deformation experiments in a novel cryogenic ring shear device—sliding rings of temperate ice over saturated tills bed at realistic ice velocities and effective stresses (i.e. ice pressure minus water pressure). To quantify rates of till transport, I used an image processing technique called digital image correlation to derive displacement and strain fields from a photographic time series of the till bed. From these data, I show that when ice and sediment are coupled at their contact, the speed of basal ice scales with grain velocities in the deforming till, and thus sediment flux. Increasing effective stress, however, influenced rates of till transport non-monotonically—first increasing shear band thickness to a threshold value and then localizing strain in contrast with

previous expectation. I frame these observations in the context of current knowledge and speculate on the broader impacts.

In chapter two, published in the *Annals of Glaciology* (Hansen and Zoet, 2019), I examine controls on subglacial rock friction for well-drained glacier beds at two different thermal regimes. Rocks entrained in basal ice that contact the bed increase resistance to basal slip (Iverson et al., 2019) and erode the substrate through abrasion (Bolton, 1974, Hallet 1979). The efficacy of these processes depends on the magnitude of forces pressing clasts into the bedrock, which have long been debated (Bolton, 1974; Hallet, 1979). Sophisticated ring shear experiments by Thompson et al., (2020) show that for temperate ice, these contact forces are primarily controlled by pressure gradients in meltwater films surrounding individual clasts and that ice overburden has minimal influence on subglacial rock friction. While these observations apply to many subglacial environments, their model predicts low stresses, which field observations indicate are not always true (Iverson et al., 2003; Cohen et al., 2005). My work provides a complimentary dataset to their experiments, broadening the scope to encapsulate areas of the bed where drainage is efficient and temperature slightly depressed below the pressure melting point (Robin, 1972). To this end, I used a modified direct shear apparatus to slide limestone beds under fixed slabs of debris-laden ice, varying the basal melt rates, temperature gradients, and cryostatic stresses. I find that basal shear stress scales linearly with both melt rate at the ice-bed interface and applied normal stress, and slight depressions in ice temperature increase the contribution of bed-normal viscous drag. These results suggest effective stress may be a dominant control on debris-bed contact forces in drained conditions, in contrast to the common assumption that it is negligible. Comparing the observed relationships between melt rate and drag to the predictions

of three friction models, we find the data are best described by a model that accounts for the effects of viscous creep and fluid flow in pre-melted film on bed-normal drag force.

In chapter three, submitted to *Geology* (Hansen et al., submitted 2022*)*, I investigate the energy consumed through subglacial abrasion—the physical expression of rock friction at the ice-bed interface—and assess the validity of the "basal-power" abrasion law used in landscape evolution models. Abrasion occurs as rocks entrained in basal ice grind down bedrock through attrition, producing linear wear features called striations (Iverson 1991) and large volumes of particulate at a catchment-wide scale (Hallet, 1996). This process (along with quarrying and, to a lesser extent, fluvial/chemical erosion) drives the rapid denudation of glaciated terrain (Alley et al., 2019; Herman et al., 2021). A new approach to modeling the impact of this process on geologic timescales assumes that bedrock abrasion rates scale linearly with energy expended through rock-on-rock friction during slip (Hallet, 2011; Ugelvig and Egholm, 2018). To provide empirical support for this hypothesis, I simulated abrasion in the lab with both the cryo-ring shear and the direct shear device by sliding debris-laden ice over rock beds at realistic temperatures, pressures, interfacial melt rates, and debris concentrations. Abraded volumes were measured directly from digital elevation models of the eroded surfaces made with a white-light interferometer, and mechanical properties of the rock beds were constrained with rock mechanics experiments to calculate the energy expenditure. With this data, I show the average shear force at the bed induced by rock friction increases linearly with abraded volume per unit area and that abrasion rates increase linearly with basal power. Lastly, I show the percentage of slip energy expended through abrasion is ~10-20x lower than prior estimates.

REFERENCES

Alley, R.B., Cuffey, K.M. & Zoet, L.K., 2019. Glacial erosion: status and outlook. *Annals of Glaciology*, **60(**80), 1-13. doi:10.1017/aog.2019.38

Carrivick, J.L., & Tweed, F.S., 2016. A global assessment of the societal impacts of glacier outburst floods. *Global and Planetary Change*, **144**, 1-16. https://doi.org/10.1016/j.gloplacha.2016.07.001

Christian, J.E., Robel, A.A., & Catania, G., 2022. A probabilistic framework for quantifying the role of anthropogenic climate change in marine-terminating glacier retreats. *The Cryosphere Discussions*, 1-28. https://doi.org/10.5194/tc-16-2725-2022

IPCC, 2022: *Climate Change 2022: Impacts, Adaptation, and Vulnerability.* Contribution of Working Group II to the Sixth Assessment Report of the Intergovernmental Panel on Climate Change [H.-O. Pörtner, D.C. Roberts, M. Tignor, E.S. Poloczanska, K. Mintenbeck, A. Alegría, M. Craig, S. Langsdorf, S. Löschke, V. Möller, A. Okem, B. Rama (eds.)]. Cambridge University Press. In Press.

Gladstone, R. M., Warner, R. C., Galton-Fenzi, B. K., Gagliardini, O., Zwinger, T., & Greve, R.: Marine ice sheet model performance depends on basal sliding physics and sub-shelf melting, The Cryosphere, 11, 319–329, https://doi.org/10.5194/tc-11-319-2017, 2017.

Hallet, B., Hunter, L. & Bogen, J., 1996. Rates of erosion and sediment evacuation by glaciers: A review of field data and their implications. *Global and Planetary Change*, **12**(1-4), 213-235. https://doi.org/10.1016/0921-8181(95)00021-6

Helanow, C., Iverson, N.R., Woodard, J.B. & Zoet, L.K., 2021. A slip law for hard-bedded glaciers derived from observed bed topography. *Science Advances*, **7(**20), p.eabe7798. DOI: 10.1126/sciadv.abe7798

Herman, F., De Doncker, F., Delaney, I., Prasicek, G. & Koppes, M., 2021. The impact of glaciers on mountain erosion. *Nature Reviews Earth & Environment*, **2**(6), 422-435. https://doi.org/10.1038/s43017-021-00165-9

Iverson, N.R., 1991. Morphology of glacial striae: implications for abrasion of glacier beds and fault surfaces. *Geological Society of America Bulletin*, **103**(10), 1308-1316. https://doi.org/10.1130/0016-7606(1991)103<1308:MOGSIF>2.3.CO;2

Iverson, N., & Iverson, R. (2001). Distributed shear of subglacial till due to Coulomb slip. *Journal of Glaciology, 47*(158), 481-488. https://doi.org/10.3189/172756501781832115

Koppes, M.N. & Hallet, B., 2002. Influence of rapid glacial retreat on the rate of erosion by tidewater glaciers. *Geology*, **30**(1), 47-50. https://doi.org/10.1029/2005JF000349

Koppes, M. & Hallet, B., 2006. Erosion rates during rapid deglaciation in Icy Bay, Alaska. *Journal of Geophysical Research: Earth Surface*, **111**(F2). https://doi.org/10.1029/2005JF000349

Rignot, E., Bamber, J., van den Broeke, M. *et al.* Recent Antarctic ice mass loss from radar interferometry and regional climate modelling. *Nature Geoscience* **1,** 106–110 (2008). https://doi.org/10.1038/ngeo102

Ritz, C., Edwards, T.L., Durand, G., Payne, A.J., Peyaud, V., & Hindmarsh, R.C., 2015. Potential sea-level rise from Antarctic ice-sheet instability constrained by observations. *Nature*, 528(7580), 115-118. https://doi.org/10.1038/nature16147

Robin, G.D.Q., 1976. Is the basal ice of a temperate glacier at the pressure melting point?. *Journal of Glaciology*, **16**(74), 183-196. doi:10.3189/S002214300003152X

Ugelvig, S.V. & Egholm, D.L., 2018. The influence of basal-ice debris on patterns and rates of glacial erosion. *Earth and Planetary Science Letters*, **490**, 110-121. https://doi.org/10.1016/j.epsl.2018.03.022

Ultee, L., Coats, S., & Mackay, J. (2022). Glacial runoff buffers droughts through the 21st century. *Earth System Dynamics*, **13**(2), 935-959. https://doi.org/10.5194/esd-13-935-2022

Williams, H., & Koppes, M. (2019). A comparison of glacial and paraglacial denudation responses to rapid glacial retreat. *Annals of Glaciology,* **60**(80), 151-164. https://doi.org/10.1017/aog.2020.1

Zemp, M., Huss, M., Thibert, E., Eckert, N., McNabb, R., Huber, J., Barandun, M., Machguth, H., Nussbaumer, S.U., Gärtner-Roer, I., & Thomson, L., 2019. Global glacier mass changes and their contributions to sea-level rise from 1961 to 2016

Chapter 1. Characterizing sediment flux of deforming glacier beds

D. D. Hansen[1], L. K. Zoet[1]

[1]*Department of Geosciences, University of Wisconsin-Madison, Madison, WI*

ABSTRACT

Deformation of subglacial sediment during basal slip shapes the beds of many fast-flowing glaciers and ice streams. The resultant sediment flux impacts glacier dynamics and rates of subglacial erosion over a range of timescales, but its fundamental dependencies are not well understood. Using a cryogenic ring shear device, we conducted a suite of experiments to investigate the effects of both effective stress and slip speed on rates of till transport. Sediment fluxes were computed using digital image correlation from a photographic time series of the till bed. We find a near linear relationship between sediment flux and slip speed, but a non-monotonic, double-valued dependency of sediment flux on effective stress. Deformation primarily occurred in a thin shear band near the ice sole, the thickness of which could vary with both parameters. Coupling between ice and till increased at higher slip speeds and effective stresses and scaled the magnitude of the flow profile.

1 INTRODUCTION

Rapid motion of many glaciers and ice-streams is facilitated by glaciers sliding over unconsolidated, water-saturated sediment, or “till” (Kamb, 2001). As this weak sediment deforms in response to the overriding ice, it is redistributed at the ice-bed interface or evacuated

from the system, reshaping the evolving subglacial landscape. This sediment flux alters the stability of ice streams (Alley et al., 2007; Bart et al., 2017; Simpkins et al., 2018), affects subglacial hydrology (Damsgaard et al., 2016), and generates many of the iconic glacial landforms exposed by paleo ice sheets (Zoet et al., 2021) and observed beneath modern glaciers (King et al., 2009). Thus, the erosion, transport, and deposition of basal till is an important control on both glacial landform development and ice sheet dynamics, and accurate estimates of till flux are a necessary component of predicting ice sheet stability.

For soft-bedded glaciers, subglacial sediment flux is partitioned between actively deforming till (Iverson, 2010), material entrained in basal ice (Rempel, 2008), and fluvial transport (Alley et al., 2003). The relative contribution of these processes to the overall sediment budget, however, is poorly constrained for many subglacial environments. With respect to sediment in transit through a till bed, which is the focus of this study, till flux is a function of the skin depth of deformation, the magnitude of strain, and its distribution in the sediment column. Deformation is often greatest at the ice-bed interface and decreases monotonically with depth to form a convex-upward profile. Field estimates for skin depth of deformation, however, range from centimeter (Engelhardt and Kamb, 1998) to meter-scale (Boulton and Hindmarsh, 1987), provoking a long-running debate on the dominant controls on the strain profile and, hence, sediment flux. Numerous mechanisms have been proposed as likely candidates, including intrinsic physical properties of the till itself such as the grain size distribution (Tulaczyk, 1999; Zoet and Iverson, 2020); effective stress (Iverson and Iverson, 2001); strain rate (Boulton and Hindmarsh, 1987); transient stress conditions that cause the locus of shear to migrate over time (Iverson et al., 1998; Tulaczyk et al., 2000; Damsgaard et al., 2020); or coupling between ice and

till at their contact (Tulaczyk, 1999; Zoet and Iverson, 2020). However, little physical evidence exists to support or refute these claims, much less isolate their relative influence on the sediment budget.

Nevertheless, despite this uncertainty, two persistent assumptions within the fields of glaciology and glacial geology are that sediment flux, Q_{sed}, scales with ice pressure (Schoof, 2007; Fowler and Chapwanya, 2014) and the slip speed of basal ice, v_{ice} (Clark, 1993). Wide-ranging and, in many instances, conflicting dependencies of Q_{sed} on the effective stress, N, (ice pressure, P_i, minus pore water pressure, P_w) and v_{ice} exist in the literature. The scaling between Q_{sed} and N arises in models that ascribe a viscous rheology to till (Hindmarsh, 1998) or assume till deforms plastically as a Coulomb material (Iverson and Iverson, 2001), and it serves as a foundational component for instability theories relating to the origin and elongation of subglacial bedforms (Fowler, 2010). However, studies that directly investigate the relationship between N and Q_{sed} are few and their results contradictory. Numerical shear experiments with SPHERE, a 3D discrete element model, demonstrated an increase in shear zone width with increasing overburden pressure for the case of idealized spheres, providing support for a positive N–Q_{sed} relationship (Damsgaard et al., 2013). More recent experiments with the same model under different boundary conditions, however, show a "double-valued" trend between N and shear band thickness (and by extension Q_{sed}), in which the depth of deformation increases to maximum around $N = 60$ kPa before decreasing at higher stresses (Kasmalkar et al., 2021). Furthermore, Boulton and Dobbie (1998) reported an inverse trend for split-cell ring-shear experiments on two subglacial tills, though they did not explicity state their boundary conditions or results. Their observation that shear zones were wider at low stresses (and faster strain rates) aligns with the

inverse relationship between stress and shear band thickness commonly reported in the geotechnical literature (Desrues and Viggiani, 2004). Friction between ice and till at their contact adds another layer of complexity as well. During a series of soft-bed deformation experiments beneath Engabreen Glacier, Iverson et al. (2007) investigated the response of a synthetic till wedge to variable N by pumping water through the system and monitoring deformation with buried tilt meters. Minimal deformation (and by extension low Q_{sed}) was inferred at both low and high stresses with a maximum occurring in-between—behavior they attributed to a tradeoff between the frictional strength at the interface as grains became submerged by a thin water layer and the strength of grain-grain contacts in the till bed.

The association of elongate bedforms with areas of fast glacier flow in relic glacier flow fields (Stokes and Clark, 2002) and beneath modern ice streams (King et al. 2009) also led some to suggest a link between Q_{sed} and v_{ice}; however, the Coulomb nature of till renders the mechanism for such a relationship unsubstantiated. Zoet et al. (2021) showed a statistically significant correlation between elongation ratio of subglacial bedforms and cumulative slip displacement for a drumlin field shaped by the Green Bay Lobe of the Laurentide Ice Sheet, providing evidence for a dependence of Q_{sed} on v_{ice},but the process driving this relationship was purely assumed and based on no known mechanism. Couette cell experiments on granular materials show that the maximum velocity in a shear band can scale with the velocity of a shearing boundary (Mueth et al., 2000). However, coupling between ice and till is likely lowest at high basal water pressures—coincidentally when sliding velocities are at their maximum. This would seemingly preclude a one-to-one scaling relationship, meaning the subglacial $Q_{sed}-v_{ice}$ relationship is more nuanced than that of a purely granular system owing to the complexities of

ice-bed coupling. Additionally, Zoet and Iverson (2020) demonstrated a velocity-dependent transition between form drag (i.e., ice sliding around clasts lodged at the interface) and skin friction (i.e., till deforming at depth) that depends on the sliding velocity, the stress state, and the grain size distribution of the till. In their conceptual model, minimal deformation occurs below a threshold slip speed (their equation 2), opening the possibility for nonlinearity in the v_{ice}–Q_{sed} parameter space.

Despite being of central concern for the fields of both glaciology and glacial geology—and in many ways the primary process linking these two fields—the rates and dependencies of subglacial till deformation are very much unresolved. Considered together, the body of prior work presents a conflicting patchwork of hypotheses and observations that offers no clear path forward, despite the high scientific and societal relevance of this problem. Quantitatively linking these two disciplines begins with developing a fundamental understanding of till flux and its dependencies therein. To date, monitoring deformation in glaciogenic sediments in response to systematic variations in slip speed and effective stress has not been possible, largely due to the inaccessibility of the ice-bed interface and the absence of a suitable experimental protocol that allows for a systematic interrogation of the dependence of Q_{sed} on factors such as v_{ice} and N. Consequnetly, only a portion of the full picture has been observable in any one instance, producing a wide array of observations that are seemingly at odds with one another.

We address the uncertainty surrounding the influence of N and v_{ice} on Q_{sed} using a novel, large-diameter, cryogenic ring shear device with a transparent sample chamber, recently constructed at the University of Wisconsin-Madison (Figure 1). To explore the dependencies of

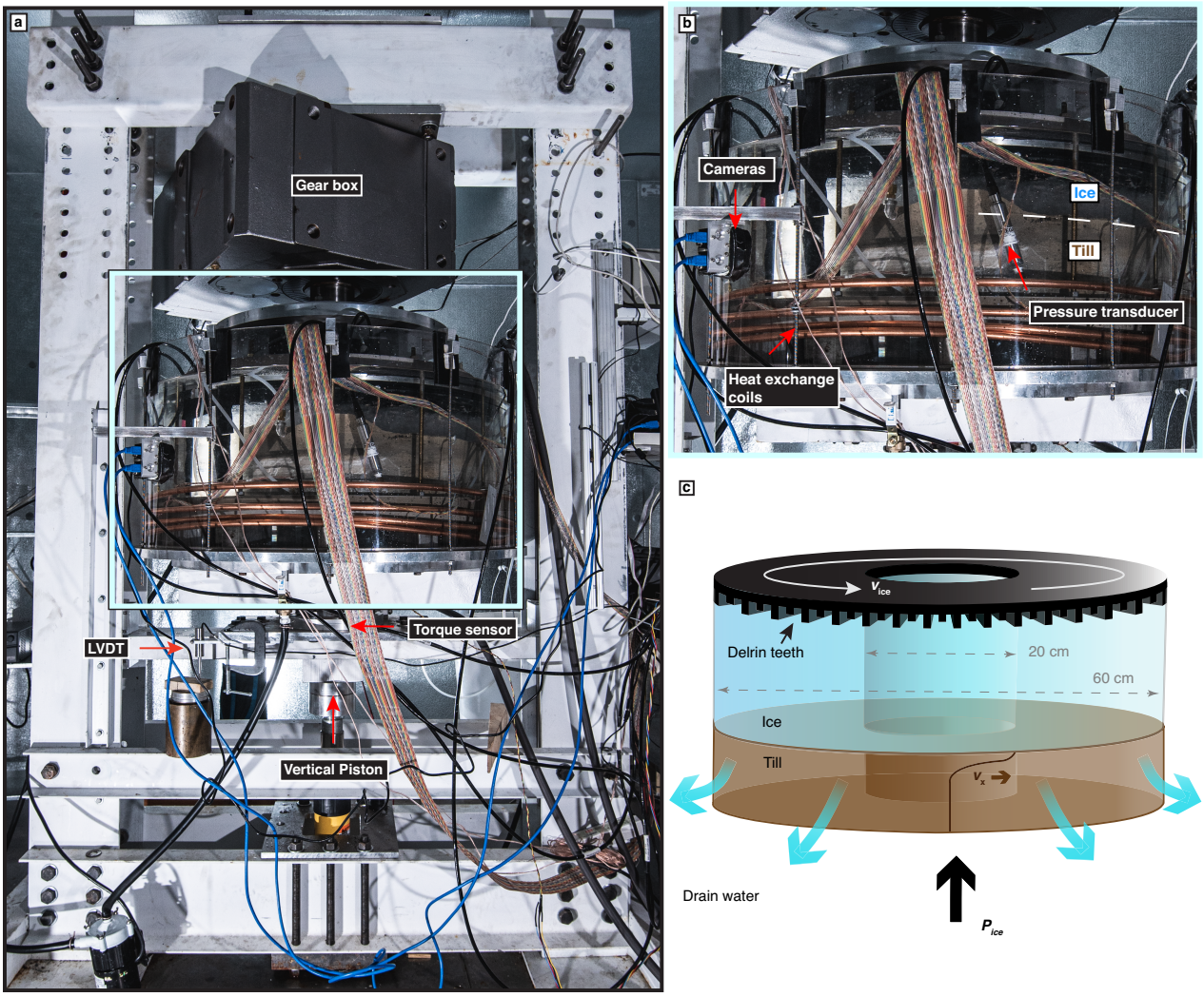

Figure 1. Experimental set up. A) A photograph of the cryogenic ring shear device. The sample chamber is suspended between vertical I-beams that make up the load frame. Pressure, P_i, is applied by a vertical piston that presses the ice ring into a bed of subglacial till. A motor connected to the gear box rotates the top platen at a prescribed velocity, v_{ice}, which grips the ice ring with a series of irregular Delrin teeth. As the ice ring slides over the till bed, a torque sensor attached to the base of the sample chamber measures the resultant drag. B) An enlarged cutaway of the sample chamber showing ice sliding over subglacial till. Cameras mounted to the outer wall monitor movement in the till bed, and three pressure transducers measure pore water pressure, P_w, in the sediment. Twelve drainage lines evacuate water from the pore space in the till throughout the experiments. C) A schematic of the sample chamber illustrating various experimental parameters. Grains in the till move horizontally at speed, v_x, (curved brown line) in response to stress exerted by the overriding ice. (Photo credit: Ethan Parrish)

Q_{sed}, we slid rings of temperate ice over a till bed at realistic subglacial conditions. With this experimental setup, we systematically varied N and v_{ice} by changing the load applied to the ice ring and its rate of rotation respectively. We quantified the resultant deformation using digital image correlation (DIC) on a photographic time series of the till bed. We find clear, though importantly not always monotonic, dependencies of Q_{sed} on N and v_{ice}—thereby experimentally addressing this problem in the coupled ice-sediment system for the first time.

2 MATERIALS AND METHODS

2.1 Experimental design

To simulate basal slip, we used a cryogenic ring shear device (Figure 1) to slide a ring of ice under an axial load (60-cm outer diameter, 20-cm inner diameter, and initially ~15-cm thick) over a ~11-cm-thick bed of till. The annular sample chamber was submerged in a temperature-controlled bath of glycol and water, regulated with a Lauda PRO 245 E circulator capable of $O(10^{-2}$ °C) precision. To create the ice ring, deionized water was frozen and crushed to create an aggregate of ice granules, which were added to the sample chamber as ~five-cm-thick layers, submerged with deionized water, and allowed to freeze. This process was repeated sequentially until the ice reached its target thickness. A single strand of beads was frozen in the ice near the outer perimeter to track cumulative ice deformation throughout the experiment (which was negligible). Once the ice ring was created, it was removed from the sample chamber so the till bed could be built in place.

Prior to loading, sediments were passed through a 9.51 mm mesh sieve, which is less than one-tenth the thickness of the bed in accordance with standard geotechnical protocol (Head, 1989). (The grain size distribution is described in the Supplemental Materials section.) After the

till was added to the sample chamber to the appropriate thickness, we leveled its surface and tamped it firmly with a rubber mallet to minimize excess void space. Four stacks of sequentially numbered beads were installed in the bed to track cumulative strain (two at the centerline and two at the outer perimeter), so that they spanned the full depth of the till and the top bead is roughly level with the ice-bed interface. Deionized water was then added to the sample chamber until the till was completely saturated, and the ice ring was lowered on top of it. A hydraulic press raised the sample chamber in place so that the ice ring contacted the Delrin teeth of the upper platen, and a layer of chilled deionized water was poured onto the top surface of the ice to couple the ice ring to the rotating platen once it froze. One consideration at this stage of the experiment was maintaining a temperature profile in the sample chamber that allowed the ice to freeze to the Delrin teeth while maintaining PMP at the ice-bed interface and till bed. To facilitate this, we dropped the level of the glycol bath to a position midway up the ice ring and held its temperature above freezing, while setting the ambient freezer temperature to -4 °C. Once the ice ring was frozen in place and coupled to the Delrin teeth, the glycol level in the bath was raised to the top of the ice ring and warmed to ~0.04 °C, which ensured that the ice remained temperate and meltwater freely drained from the till without flash freezing in the drainage lines. At this stage, the motor was engaged. Adhesive-backed rubber installed at the base of the sample chamber minimized slip of the till along the bottom boundary during the experiments.

As the top platen rotated, spinning the ice ring over the till bed, axial load was applied via an ISCO 100DM syringe pump, capable of maintaining a pressure within ± 0.2 kPa. Resistance to shear is measured by a custom-built torque sensor mounted at the base of the sample chamber, and pore water pressure in the till was measured with three Omega pressure transducers mounted

~7 cm below the ice-bed interface in the sidewall. Twelve drainage lines connected the sample chamber to atmospheric pressure, and twelve-glass bead thermistors installed in the sidewalls of the sample chamber recorded temperature throughout the experiment. The grain size distribution of the till was measured using laser diffractometry for grains smaller than 1 mm and manually sieved to determine the size fractions between 1 mm–9.51 mm (see Supplemental for details).

2.2. Variable sliding velocity and effective stress

We assessed the influence of effective stress and sliding velocity on deforming Horicon till—a sandy, subglacial diamicton deposited by the Green Bay lobe of the Laurentide ice sheet (Mickelson and Syverson, 1997)—and collected data during two experiments. For the first experiment, we successively applied four effective stresses, $N \sim 8$ kPa, ~22 kPa, ~50 kPa, and ~113 kPa, while implementing velocity steps throughout. In the event that variable water pressure led to slight differences in N between successive steps ($\lesssim 2$ kPa difference), we report the average of the set for clarity when referring to the group (see Table 1).

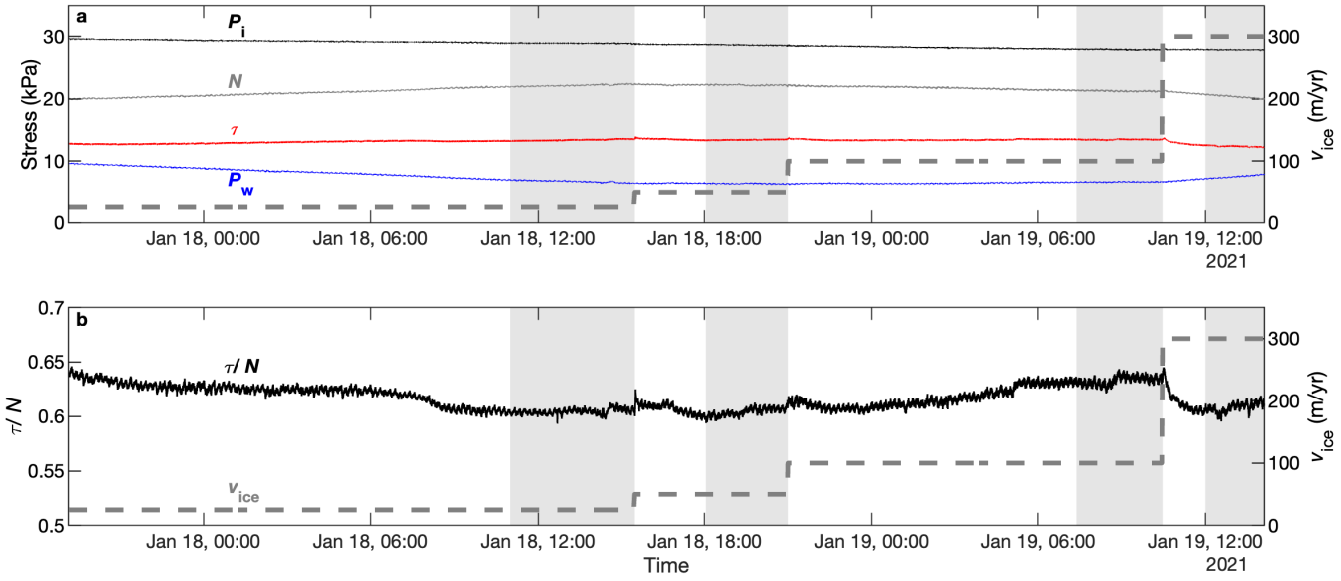

Figure 2. a) Representative time series showing the evolution of four experimental parameters: applied ice pressure (P_i), average water pressure recorded in the till (P_w), effective stress ($N = P_i - P_w$), and basal shear stress, τ, over the course of four different slip speeds (v_{ice} = 25, 50, 100, and 300 m/yr). Dashed grey lines are the prescribed ice velocity in both plots, and the shaded regions indicate windows of data used for subsequent calculations. We select periods in which τ remains relatively constant, assuming critical state deformation. b) The coefficient of friction, presented as τ/N, calculated over this same period.

At $N \sim 22$ kPa, we implemented four velocities sequentially (v_{ice} = 25 m/yr, v_{ice} = 50 m/yr, v_{ice}= 100 m/yr, v_{ice} = 300 m/yr), and for $N \sim 50$ kPa and $N \sim 113$ kPa, we conducted a single velocity step from ~100 m/yr to 300 m/yr. Finally, we measured a single effective stress ($N \sim 199$ kPa) in a second experiment at v_{ice} = 100 m/yr. Reported velocities represent the speed at the outer boundary of the cylindrical sample chamber. After each change in velocity or stress, we allowed the system to reach critical state deformation, at which point shear stress remained relatively constant (Figure 2). Following a change in axial load, the path to critical state could take a day or longer but was generally on the order of one hour following a change in velocity.

Values for *N* reported herein represent the average normal stress over a chosen interval minus the average water pressure recorded by the three transducers installed near the till bed.

2.3 Digital Image Correlation

We estimate rates of till deformation using two-dimensional digital image correlation (2D-DIC), an image processing technique that quantifies displacement occurring in a plane orthogonal to the camera axis (Figure 3). DIC compares the grayscale intensity of two digital images (a "reference image" and a "secondary image") captured at discrete moments in time to identify the position of maximum correlation. For an 8-bit image, pixels are assigned a numerical value between 0 (pure white) and 255 (pure black), and the reference image is then split into a series of subsets of prescribed dimensions. An algorithm then searches a larger region of interest defined on the slave to identify the position of maximum correlation for each subset. Displacement is computed as the difference between the original position of the subset and this correlation maxima, and given the time interval between images, the local velocity vector can be determined.

For this study, we used a Matlab routine developed by Bickel et al. (2018), which is freely available online (https://github.com/bickelmps/DIC_FFT_ETHZ) and implements a fast Fourier transform correlation approach. Images were co-registered to an accuracy of 0.5 pixels (Guizar-Sicairos et al., 2008), and a vector post-processing filter was applied at the conclusion of each DIC run to eliminate spurious results greater than 1/3 the dimension of the interrogation window. DIC algorithms are sensitive to image texture patterns (Crammond et al., 2013), with finer speckles and a high degree of randomness typically producing the best results (Barranger et

al., 2010). Since the till used in these experiments was largely homogenous in color, we seeded it with black sand (~10% by weight) to increase contrast and improve feature tracking.

Digital images, sized 2048 x 1536, were acquired using two vertically stacked FLIR digital cameras, equipped with Edmund Optics F1.4 lenses with a 25 mm focal length. These cameras are mounted against the outer acrylic wall of the glycol/water bath, and two strips of white LED lights angled against the outer wall of the sample chamber illuminated the photographic surface. The field of view of the cameras overlapped by 123 pixels in the first experiment and 330 pixels in the second. All images are acquired at one-minute intervals. For 2D-DIC, the camera's line of site (LOS) should ideally be oriented perpendicular to the field of deformation. However, this was not strictly possible in our experiments due to the cylindrical geometry of the sample chamber. Error introduced by out-of-plane deformation is influenced by the degree of curvature of the deformation field in the camera's field of view. For our setup, the maximum tangent angle between the chamber wall and a plane perpendicular to LOS was ~1.3°, which introduces error on the order of 0.01 pixels (or ~150 nm) (Meng et al., 2006). Given the scope of our experiments, uncertainty at this scale is negligible, and the deformation field can be approximated as planar. Pixel dimensions for each set of images were determined from photographs of a one-mm-scale grid placed flush against the chamber wall in the camera's field of view. For the first and second experiments, the corresponding pixel dimensions were approximately $1.78 \cdot 10^{-5}$ m for both the top and middle cameras. For the second experiment, the pixel dimensions are $1.89 \cdot 10^{-5}$ m and $1.91 \cdot 10^{-5}$ respectively. Differences in pixel dimensions arose due to slightly different positions of the camera mount or focus between the respective experiments. Lens distortion at this scale was negligible.

An important consideration when setting up a DIC run is setting the optimal size of the search window. With respect to the dimensions of this subset, a trade-off exists between the desired accuracy of the estimated displacement and the resolution of the displacement field. Larger search windows ensure a good signal-to-noise ratio but sacrifice accuracy as the estimates are averaged over a larger correlation window, and the converse is true for smaller window sizes. Based on their results using the same algorithm, Bickel et al. (2018) suggest a subset should be selected that is 6–12 times greater than the expected displacement. In our image pairs, displacement is not constant through the field of view, but rather decreases from a maximum near the ice-bed interface with depth to zero and varies with different rotation rates. We implemented windows that were at least 6 times greater than the maximum displacement for most runs, except those conducted at v_{ice} = 300 m/yr, which had a window that was at least 4

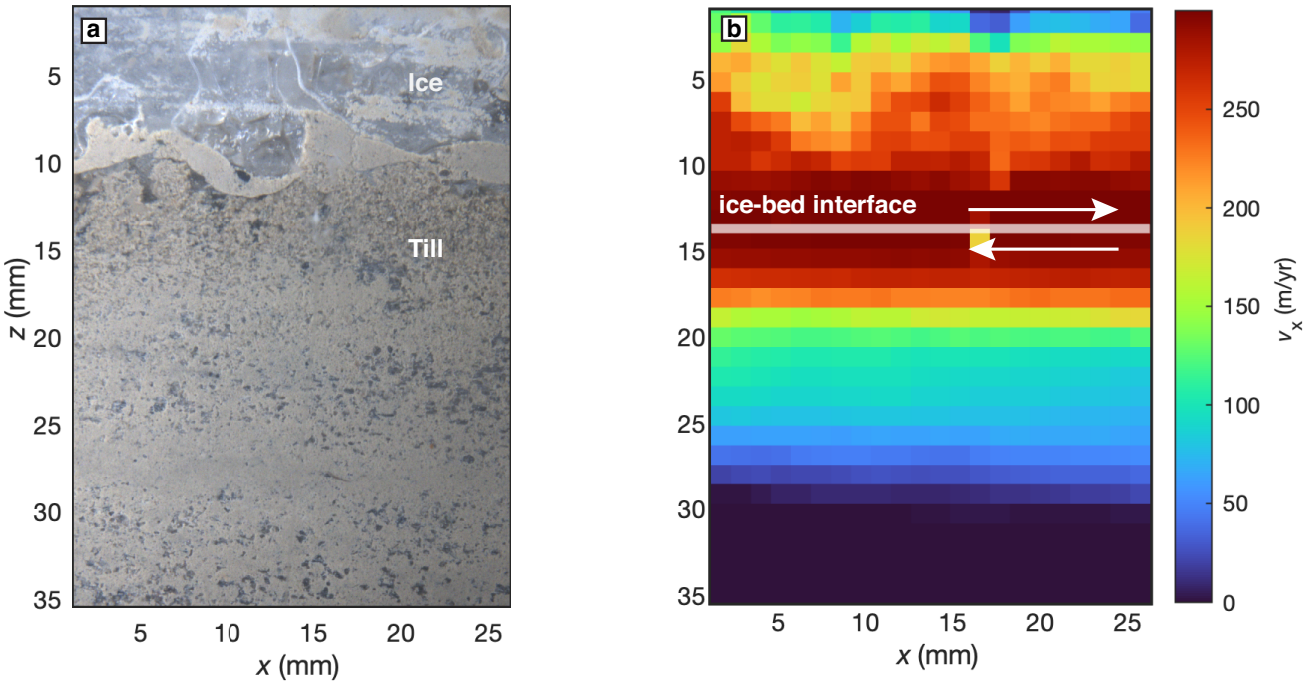

Figure 3. a) Example photograph showing camera field of view. b) Mean horizontal velocities (v_x) computed using digital image correlation from a photographic time series for an interval with $N \sim 50$ kPa and $v_{ice} = 300$ m/yr (see also Supplemental video 1). The white line designates where we infer the position of the ice-bed interface, and the two white arrows convey the sense of shear. (Lower velocities seen above ice-till boundary reflect poor correlation between due to the photographic texture of the ice surface rather than actual ice speed and are not considered in any calculations.)

times greater. Photographs were taken at one-minute intervals throughout the experiments, and appropriate intervals were selected from this time series for each value of v_{ice} to perform DIC analysis. For example, we used a 128-pixel interrogation window for photographs taken at v_{ice} = 100 m/yr that contained the bulk of the shear band deformation, performed the DIC analysis for two sets of two-minute intervals in the same time window, and then averaged both sets to obtain the mean flow profile. This corresponds to a maximum displacement in each two-minute pair

that was approximately 7–8 times smaller than the dimensions of the interrogation window. Data at the first column was discarded from subsequent calculations due to spurious edge effects, as well as negative horizontal displacements measured during shear. During three stages of the experiment ($N \sim 50$ kPa at $v_{ice} = 100$ m/yr, $N \sim 114$ kPa at $v_{ice} = 100$ m/yr, $N \sim 111$ kPa at $v_{ice} = 300$ m/yr), a shutter malfunction produced dark images with low RGB pixel values, which diminished the quality of the correlation. However, recorded data was sufficient for the algorithm to estimate displacement at reasonable correlation criteria, based on the translation invariant normalized root mean squared error (NRMSE) calculated for each displacement value (Guizar-Sicairos et al., 2008). Mean NRMSE for the three darker periods were 0.19 (with corresponding standard deviation, $\sigma_{NMRSE} = 0.019$, and number of samples, $n = 138{,}000$), 0.19 ($\sigma_{NMRSE} = 0.019$; $n = 112{,}320$), 0.19 ($\sigma_{NMRSE} = 0.021$; $n = 67{,}800$) respectively; whereas mean NMSRE for all other intervals ranged between 0.04–0.10.

2.4 Estimating shear band thickness

There is no single agreed upon criterion to determine the thickness of a shear band, t_{sb}, in a granular material (Alshibli, K.A. & Sture, 1999; Rechenmacher and Finno, 2004; Zhu et al., 2016; Rattez et al., 2020; Soltanbeigi et al., 2020). Shear bands are characterized by a loss of homogeneity in the deformation field that concentrates excessive shear strain and dilatancy in a thin band. Thus, attempts to delineate their boundaries using experimental data often focus on how these two parameters vary across a cross section of the shear band with respect to the surrounding medium. Dilatancy is poorly constrained in our experiments. Shear strain rate profiles, however, can be computed from the DIC-derived displacement data, and these provide a

qualitative means to demarcate the boundaries of the shear band without prior knowledge of the void ratio during shear.

We adopt an approach developed by Soltanbeigi et al. (2020), who suggest the boundaries of a shear band can be approximated as the inflection points on a cross-sectional strain profile of the shear band (Figure 4). Our workflow can be summarized as follows: First, we calculate the spatial derivatives of the velocity vectors derived for each image pair in the time series using the central difference for interior data points and a single-sided difference method for gradients at the boundaries. We then calculate the shear strain rate, a component of the 2D small strain rate tensor, for each image pair from the velocity gradient. Median shear strain rate profiles are calculated from the time

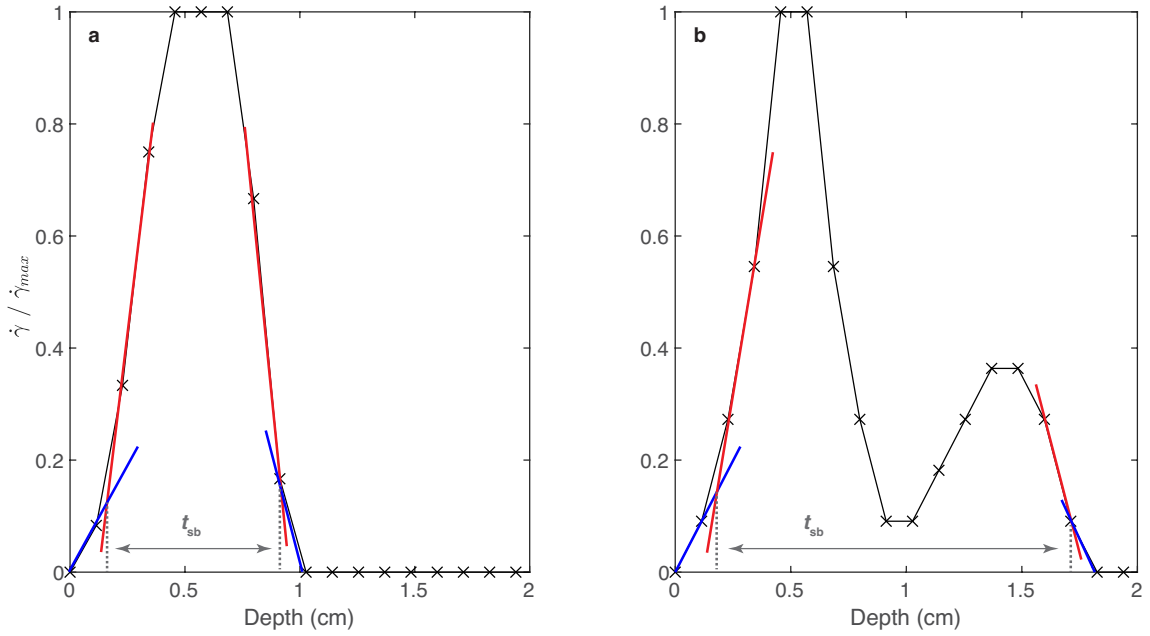

Figure 4. Method for determining shear band thickness, t_{sb} using the shear strain rate intensity profile (i.e. median shear strain rate, $\dot{\gamma}$, normalized by its maximum value, $\dot{\gamma}_{max}$) for both a) single peak and b) bimodal distributions. We identify the intersection between tangents fit to the linear regions between the curve and the peak and the tails of the profile where the rate of change is approximately constant. t_{sb} is the distance between the two intersections. Depth here denotes distance from the inferred ice-bed interface.

series, normalized by their maximum value, and then plotted against depth to form a cross-sectional shear strain rate intensity profile. The criteria for estimating shear band width in this parameter space (i.e. "method II" in Soltanbeigi et al., 2020) can be summarized succinctly as: 1) fitting tangents to the two tails of the profile where the rate of strain change is approximately constant, 2) fitting tangents to the linear regions of the curve between the tails and the peak, 3) locating the points of intersection for both sets of tangent lines, 4) and then measuring the distance between these two points of intersection on either side of the shear band—this value is presumed to be t_{sb}. An advantage of this method with respect to our data is that it doesn't rely on the assumption of a Gaussian distribution of shear strain, since distributions were bimodal at certain stages of the experiments (Figure 4b).

2.5 Estimating sediment flux

We calculate sediment flux by numerically integrating time-averaged 1D horizontal velocity profiles computed from the DIC time series using the trapezoidal rule (Scott, 2011). Unlike our calculations for shear band thickness, we aim to include the totality of grain motion that occurs in response to the overriding ice. A complicating factor in these calculations is that the ice-bed interface is occasionally obscured from the cameras' field of view by a thin layer of sediment squeezed between ice and acrylic at the outer boundary of the sample chamber. For some steps, a clear demarcation between ice and till can be inferred from the flow profiles, due to a sharp inflection point in the horizontal velocities that corresponds to vertical position with zero shear strain rate. For other steps, this distinction is not as apparent from the mean v_x profiles alone, so

we use the optical record in conjunction with these data to clarify the position of the ice-bed interface.

3 RESULTS

3.1 Shear band morphology

Mean horizonal velocity (v_x) profiles computed from the DIC time series show that steady-state deformation in the till bed was primarily concentrated in a thin band near the ice sole ~0.7–2.5 cm thick where particle velocities decreased monotonically with depth (Figure 5 and Figures 8b, d, and f). The morphology of the v_x profiles varied, though most do not resemble the canonical "concave-down" exponential decay in velocity with depth. Rather, many resemble an error function, similar to velocity profiles reported in DEM simulations (Damsgaard, 2013) and numerous soft matter experiments in Couette cell sample chambers (Fenistein et al., 2004; Roy et al., 2019).

Common practice is to normalize shear band thickness, t_{sb}, by the median grain size diameter, D_{50}, of the sediment ($D_{50} \sim 0.53$ mm for the till used in our experiments). Over the parameter range tested, t_{sb}/D_{50} ranged from ~11 to ~ 47. These values fall well within the overall spread recorded for plane strain deformation experiments, which are commonly reported between 5–15 but can vary by up to an order of magnitude or more for different materials and experimental setups (Wu et al., 2008). Rattez et al. (2020), for example, measured the thickness of shear bands produced during triaxial experiments on sediments with different grain size distributions (GSD), and reported significantly higher t_{sb}/D_{50} for sediments with fractal GSD such as till than for sediments with uniform granularity (16.7 compared to 10.3 respectively in their experiment at a confining stress of 275 kPa).

Table 1. Experimental properties for each stress and velocity step†

v_{ice} [m/yr]	P_i [kPa]	P_w [kPa]	N [kPa]	num_{data}	num_{pic}	Q_{sed} [m^3/yr]
100	10.7 ± 0.04z23	2.36 ± 0.0591	8.35 ± 0.0053	6602	111	0.351 ± 0.0238
25	28.9 ± 0.381	5.98 ± 0.152	22.9 ± 0.168	15897	264	0.0752 ± 0.0070
50	28.6 ± 0.0584	5.62 ± 0.0586	23.0 ± 0.0068	10561	176	0.203 ± 0.0154
100	28.0 ± 0.092	5.83 ± 0.070	22.2 ± 0.0134	23041	384	0.510 ± 0.0434
300	27.9 ± 0.0410	6.74 ± 0.208	21.2 ± 0.0449	7681	197	1.51 ± 0.153
100	83.5 ± 0.166	33.2 ± 0.238	50.4 ± 0.0835	27601	260	0.661 ± 0.0434
300	83.8 ± 0.0392	33.6 ± 0.154	50.2 ± 0.0253	8881	149	1.99 ± 0.0959
100	174.4 ± 0.0660	60.8 ± 0.692	113.6 ± 0.4832	23337	389	0.576 ± 0.0425
300	174.4 ± 0.0345	63.0 ± 0.346	111.4 ± 0.1209	6840	104	1.62 ± 0.147
100	241.8 ± 1.060	42.6 ± 0.793	199.2 ± 1.751	25006	418	0.473 ± 0.0334

†Ice velocity, v_{ice}; mean overburden pressure, P_i; mean pore water pressure, P_w; mean effective stress, $N = P_i$-P_w; number of samples (acquired at 1 s intervals), num_{data}; number of photographs used for DIC calculation (acquired at one-minute intervals), num_{pic}; sediment flux, $Q_{sed.}$ We state corresponding standard deviations and propagated uncertainty as "±".

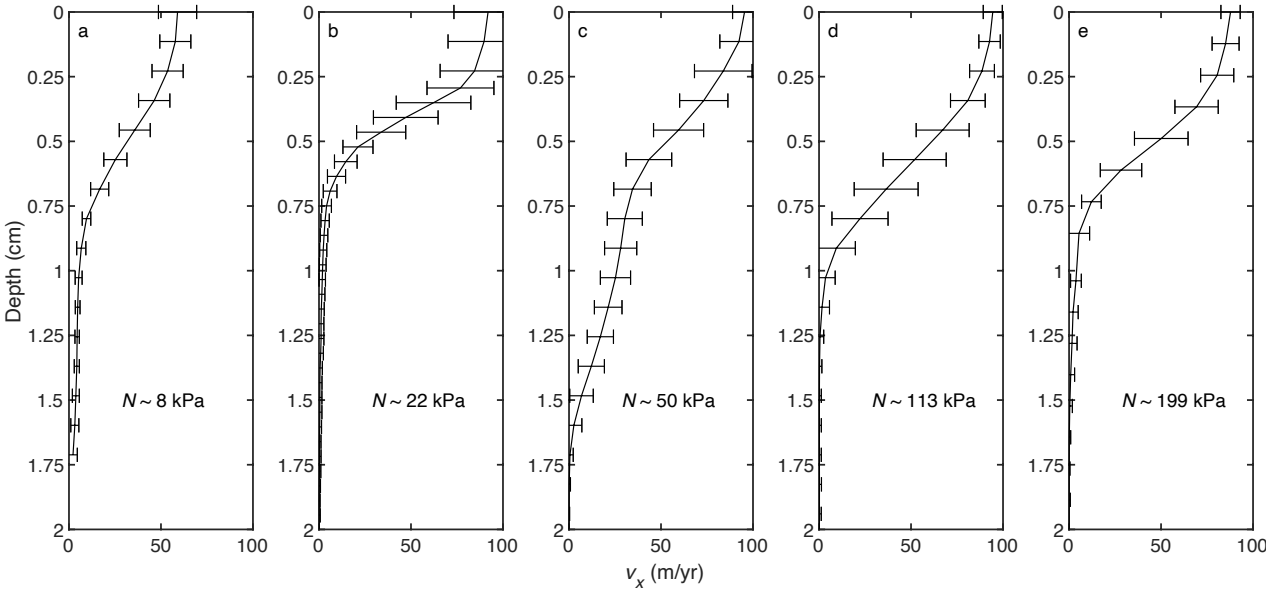

Figure 5. Five mean horizontal velocity profiles (v_x) computed from the digital image correlation time series for different effective stresses (N) at single prescribed ice velocity (v_{ice} = 100 m/yr). Deformation was largely concentrated in thin zone near the ice-bed interface approximately 0.7-2.5 cm wide throughout the experiments. Depth denotes the vertical distance from the ice-bed interface. Error bars show the standard deviation of horizontal velocities at each vertical position.

3.2 Influence of effective stress on sediment flux

Mean v_x profiles computed for different values of N at two sliding velocities, v_{ice} = 100 m/yr and v_{ice} = 300 m/yr initially show a widening zone of deformation with increasing N, but past a threshold value the deforming layer thins (Figure 5). The shear band at $N \sim 8$ kPa (Figure 5a) is the exception to this trend, as deformation is slightly more distributed than the subsequent stage at $N \sim 22$ kPa (Figure 5a). This behavior likely

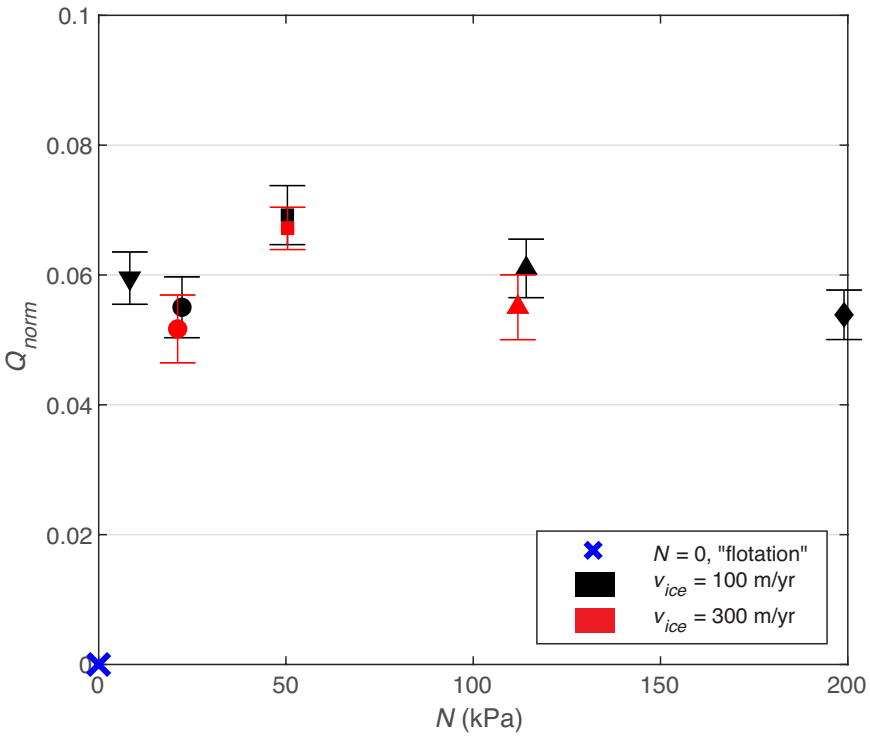

Figure 6: Normalized sediment flux, Q_{norm} varies non-monotonically with effective stress, N, at two different slip speeds, v_{ice}. To obtain (dimensionless) Q_{norm}, mean horizontal velocity profiles (assuming unit width) were normalized by their maximum value and integrated with respect to vertical position, which was normalized by the thickness of the till bed. Error bars represent the normalized standard deviation of the horizontal velocity measurements, propagated through the integration. Horizontal error bars for N are smaller than the marker width. Marker shapes denote the stress state, and colors convey velocity. This classification scheme is maintained in all subsequent plots.

reflects the evolution of the experiment over the first two days, rather than an intrinsic characteristic of the N–Q_{sed} relationship.

We compute the sediment flux at each N by integrating the 1D v_x profiles numerically with respect to depth. For this calculation, we assume unit width radially (directed into the ring away from the outer sample chamber wall) to report Q_{sed} in units of m^3/yr (Table 1). Because the magnitude and vertical distribution of the particle velocities both contribute to Q_{sed}, the variable coupling between ice and till introduces scatter in the N–Q_{sed} relationship, though rates of till transport are clearly elevated at the faster sliding speed. Dividing each velocity profile by its respective maximum v_x prior to integration normalizes the influence of velocity and allows for a direct comparison of the N–Q_{sed} trends at the two sliding speeds. With this correction applied, both sets of N–Q_{norm} data collapse along similar curves (Figure 6), in which Q_{norm} increases with increasing N from the point of flotation ($N = 0$) to a maximum value around $N \sim 50$ kPa, before decreasing at higher stresses. This "double-valued" N–Q_{norm} relationship arises from the evolution of t_{sb} with the stress state. Figure 7a shows the variability of t_{sb}/D_{50} with N at two sliding speeds, v_{ice} = 100 m/yr and 300 m/yr. At v_{ice} = 100 m/yr, t_{sb}/D_{50} initially increases to a maximum ($t_{sb}/D_{50} \sim 32$ at $N \sim 50$ kPa) before reducing at higher stresses.

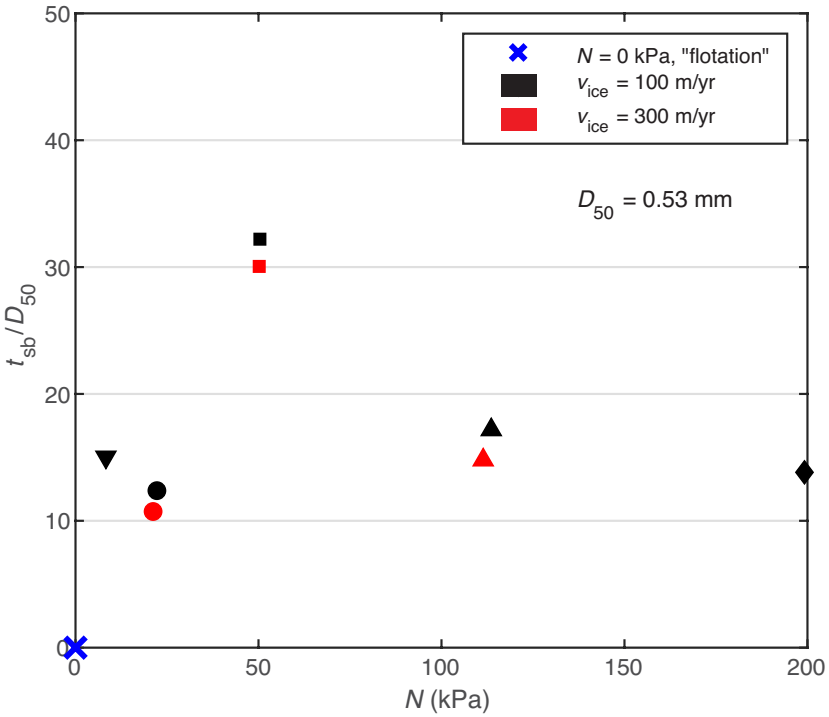

Figure 7. Relationships between estimated shear band thickness, t_{sb} (normalized by the median grain diameter of the sediment, D_{50}) and effective stress, N, plotted for two ice velocities. Horizontal error bars for N are smaller than the marker width.

3.3 Influence of slip speed on sediment flux

Velocity steps conducted at three different effective stresses demonstrate an increase in Q_{sed} with increasing v_{ice} (Figure 8a, c, e). For the velocity steps from 100 m/yr to 300 m/yr, we observed an approximately threefold increase (3.0x, 3.0x, and 2.8x respectively) in Q_{sed} with a threefold increase in sliding speed at all three values of N. This proportionality is clearly reflected in a side-by side comparison of the normalized horizontal velocity profiles (Figure 8b, d, f), which show little change in the relative vertical distribution of v_x at these speeds even though v_{ice} scales the magnitude of the flow profile. For the sliding speeds implemented at $N \sim 22$ kPa, which represent our most complete span of this parameter space, the v_{ice}–Q_{sed} relationship appears

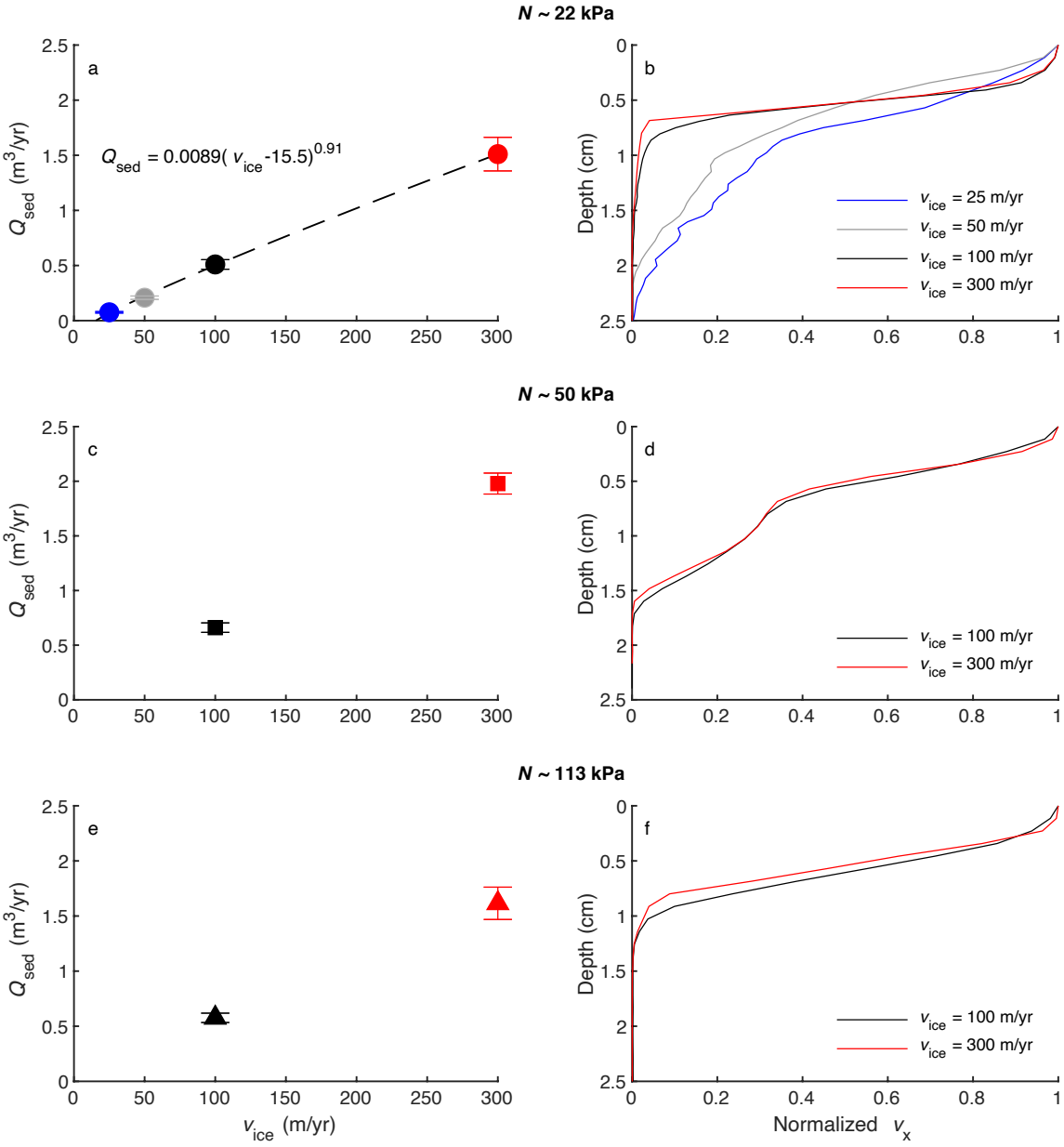

Figure 8. (a, c, e) Sediment flux, Q_{sed}, increases monotonically with slip speed, v_{ice}, at three different effective stresses, N. We integrate mean horizontal velocity, v_x, profiles (assuming unit width) with respect to vertical position to obtain Q_{sed}. Error bars show the standard deviation of the horizontal velocities, propagated through the numerical integration. (b, d, f) Mean horizontal velocity profiles for different slip speeds normalized by their maximum velocity. Depth represents distance from the ice sole. Shared colors between Q_{sed} and normalized v_x plots were computed from the same selection of data. Dashed line and equation in 8a represent the best fit curve computed through linear regression.

weakly non-linear with a trendline that is offset from the origin based its best fit regression (Q_{sed} = 0.008862(v_{ice}-15.48)$^{0.9094}$). Between the windows of data selected for 25 m/yr and 100 m/yr, deformation localized from a zone distributed over ~2.5 cm with slightly irregular flow profiles to a thin shear band.

3.4 Ice-till coupling

Coupling between ice and till, presented here as the ratio between the maximum v_x in each flow profile and the slip speed of basal ice (v_{max}/v_{ice}), changed nonlinearly in response to both changing N and v_{ice} (Figure 9a and b). Increased N at a single slip speed (v_{ice} = 100 m/yr) resulted in a steep increase in v_{max}/v_{ice} from 0–22 kPa followed by a nearly coupled interface at subsequent higher stresses (Figure 9a). Velocity steps implemented at N ~ 22 kPa produced a nonlinear increase in v_{max}/v_{ice} as well (Figure 9b). For steps at N ~ 50 kPa and N ~ 113 kPa, the constrained, but coupling appears to have reached a maximum at 100 m/yr within estimated uncertainties.

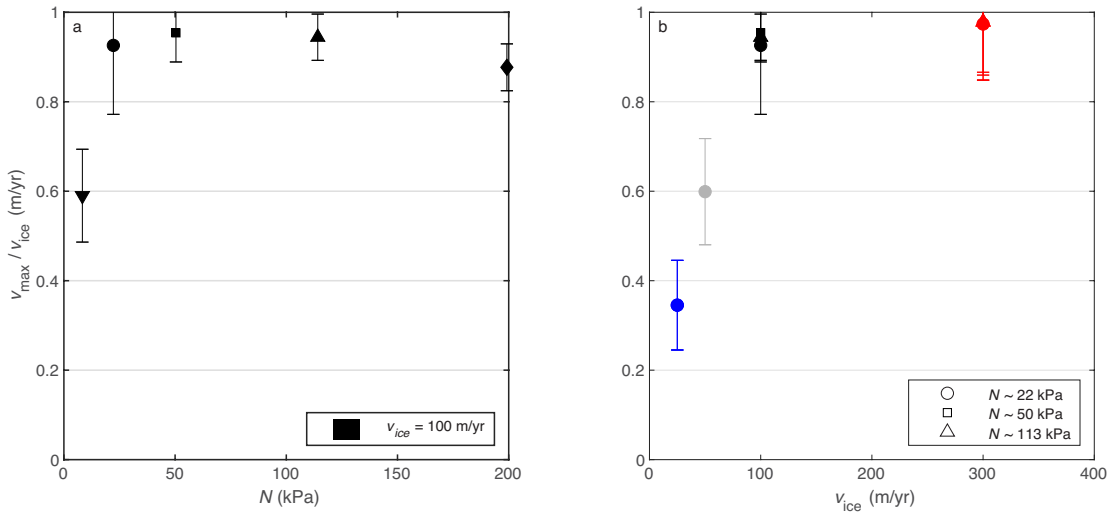

Figure 9. Observed relationships between a) effective stress, N, and b) ice velocity, v_{ice}, and the coupling between ice and till, expressed as the maximum horizontal velocity of till at the ice-bed interface, v_{max}, normalized by the speed of the ice, v_{ice}. Error bars denote standard deviation associated with each v_{max} normalized by the v_{ice}. Horizontal error bars for N are smaller than the marker width.

4 DISCUSSION

4.1 Shallow deformation in subglacial environments

Till deformation in glacial settings occurs at depths spanning orders of magnitude (Evans et al., 2006); however, the propensity for pervasive shearing to occur at steady state conditions or solely in response to transient forcing is controversial. This uncertainty is further exacerbated by the lack of evidence for distributed deformation in the glacial geologic record, which suggests that shallow deformation dominates in subglacial environments (Piotrowski et al., 2001). Our results add further support to the hypothesis that steady-state deformation in fine-grained or sandy subglacial till is largely accommodated in a thin shear band near the ice sole. Additional factors—such as a coarser grain size distribution (Rattez et al., 2020), the presence of ploughing clasts or ice keels at the ice-bed interface (Tulaczyk et al., 2001), or a migrating failure plane due to a transient evolution in N (Iverson et al. 1998; Damsgaard et al., 2020)—may drive deformation deeper, but in their absence, shallow deformation dominates. This finding is consistent with Engelhardt and Kamb's (1998) inference of a thin shear band beneath an Antarctic ice stream where significant variation in N is uncommon and the ice slides over fine-grained till (Tulacyzk et al., 1998).

Because our results pertain to a single GSD, it is instructive to consider how trends may vary for tills with contrasting granulometry. Few data exist regarding the scaling relationship between t_{sb} and D_{50} for sediments with fractal GSD (Tulacyzk, 1999; Rattez et al., 2020). Our expectation for deforming till, based on recent experimental work by Rattez et al. (2020), is that t_{sb} covaries with $D_{50,}$ but the magnitude of t_{sb}/D_{50} correlates inversely with the degree of grain uniformity. A caveat with respect to the subglacial system, however, is that this relationship may

break down for tills where ice velocities are too slow to mobilize sediment particles at the interface (Zoet and Iverson, 2020). Future work exploring the variability of t_{sb}/D_{50} for a range of tills under similar stress conditions would further bolster our understanding of subglacial till flux.

4.2 Double-valued sediment flux at increasing effective stress

The "double-valued" trend we observe between N and t_{sb} contradicts the common assumption for subglacial settings that Q_{sed} increases monotonically with N. Although the rising limb occurs over a range of N that is particularly relevant to the dynamics of modern ice streams (Meyer et al., 2018), these stresses are substantially lower than pressure concentrations possible on the stoss side of bedform obstacles (Alley et al., 2021), which would fall within the decreasing limb of the relationship. This overall behavior, however, is consistent with the double-valued trend Kasmalkar et al. (2021, Figure 3) reported from recent DEM experiments investigating till dynamics, and it aligns with the inverse relationship between N and t_{sb} reported for numerous physical and numerical experiments within the fields of civil engineering and soft matter physics (Desrues and Viggiani, 2004; Gu et al., 2014, Figure 10a), since the minimum stresses applied in these studies are generally too high to capture the rising limb we observe at low stresses ($N \sim 0$–50 kPa).

Presumably, the disparity between our results and the assumptions of prevailing glaciological models exists because the constitutive laws commonly used to parameterize till deformation do not adequately capture the micromechanics controlling strain distribution at the grain scale. Current understanding is that the frictional response of glacial till to an applied load fits a Mohr Coulomb rheology, in which till strength is linearly proportional to the effective stress and independent of strain rate past a threshold sliding velocity (Kamb, 1991; Iverson et al.,

1998). Conceptual models of till deformation conceived in a continuum framework capture these well-documented bulk frictional properties and suggest that depth of deformation scales with effective stress (Iverson and Iverson, 2001). They do not, however, account for the mechanics of strain localization—a complex and ubiquitous process in geomaterials that defies simple parameterization (Tordesillas, 2007).

Heterogeneity in the stress field of granular materials, perhaps due to variable packing density or particle geometry, promotes instability and localized failure, which concentrates deformation in thin shear bands (Schall and Hecke, 2010). Once shear banding initializes, subsequent deformation can occur entirely within its confines, while the adjacent granular matrix remains static or moves as a rigid block (Rechenmacher et al., 2010). Strain distribution in a shear band is largely driven by formation and buckling of grain columns (or "force chains") that span its width (Rechenmacher, 2006). When a column fails, grains move past each other through the combined actions of sliding and rolling, depending on the force and torque applied. However, rotation rather than sliding appears to be the dominant style of movement within shear band boundaries once the residual state is reached, with little rotation occurring in the adjacent granular matrix (Oda and Kazama, 1998). Simulations with 2D DEMs that parameterize rolling resistance at particle contacts (Iwashita and Oda, 2000; Tang et al., 2016) and experimental observation (Amirrahmat et al., 2019) show that this rotation is a first-order control on shear band geometry. Free rolling particles produce wider shear bands with diffuse edges; whereas increased rotational resistance leads to thin zones of deformation characterized by steep rotational gradients at the boundaries. Rotational resistance is controlled by particle interlocking, which in turn is determined by the particle shape, surface texture, and the void ratio in the shear band

(Hasan and Alshibli, 2010; Tian et al. 2020). Greater void ratio corresponds to a smaller number of contact points between interlocked grains and a decreased resistance to rolling. This point is particularly relevant in the context of our experimental results, since the critical state void ratio in a shear band is greater at low effective stresses (Imseeh et al., 2020). These particle kinematics suggest that the decreasing limb of the double valued N–Q_{sed} relationship we observe may arise due to suppressed grain rotation along shear band boundaries past the threshold N. This would lead to a decrease in shear band thickness with increasing effective stress, which is precisely the behavior we observe.

On the other hand, too much void space inhibits the transmission of forces across an unstable particle network since rotational resistance stabilizes particle columns (Gardiner and Tordesillas, 2004). This could explain the initial rise in t_{sb} and Q_{sed} with increasing N, since the larger void ratio and lower rolling resistance at low values of N would limit the length of the stable particle columns. As rolling resistance increases with N, we anticipate the number of particles in a column—and thus t_{sb}—to increase concomitantly until a threshold N, at which point the balance between particle column stability and grain movement at the boundaries is conducive for a maximum thickness of the deforming layer. Further work is required to test this hypothesis.

4.2 Ice-till coupling scales velocity dependent sediment flux

Boulton and Dobbie (1998) reported that shear bands thickened at faster strain rates in split-cell ring shear experiments; however, we observe no such velocity-dependent increase in t_{sb}. Conversely, t_{sb} decreased at faster velocities for some steps (Figure 7), but the difference in normalized flow profile is subtle for all stages with a well-developed shear band (Figure 8b, d,

and f). The above implies that friction at the contact between ice and till controls the positive relationship we observe between v_{ice} and Q_{sed}. This finding aligns with previous soft matter physics research that suggest that the flow profile in granular material deforming in response to an overriding solid is nearly rate independent when normalized by the imposed shearing rate (Howell et al., 1999). Shear speed, however, influences the magnitude of the flow profile due to friction at the particulate-continuum interface. Coupling at this boundary has been shown to increase with the surface roughness and hardness properties of the continuum material (Frost et al, 2002). In the case of a perfectly coupled interface, grains at the boundary move at the speed of the contacting solid, and particle velocities decay with distance from the boundary. A perfectly smooth boundary on the other hand facilitates pure slip at the interface with no grain motion. Between these end member scenarios, grains at the boundary are mobilized at a slower rate than the contacting medium, which is where our experiments largely reside.

Assuming a planar ice sole, roughness at the ice-bed interface is primarily controlled by the grain size distribution of the till (Tulaczyk, S., 1999) and, if present, the thickness of a water film between ice and till, which submerges grains smaller than its depth (Creyts and Schoof, 2009). During basal slip, ice moves past exposed clasts through a combination of regelation and viscous creep, inducing a drag force against the stoss side of the particles that scales with slip speed, effective stress, and clast radius (Zoet and Iverson, 2020). For ice to mobilize a given clast, this drag must exceed the frictional strength of the till at grain contacts, at which point the mechanism accommodating forward motion shifts from slip to ploughing. The velocity at which this transition occurs, u_t, is given by Zoet and Iverson's equation 2. Larger clasts mobilize at slower speeds, and thus, for a given effective stress, an increasing number of grains at

increasingly smaller diameters begin to plough as ice velocity surpasses each grain's respective u_t. Their formulation (using the physical parameters they list for the same till) predicts that the minimum slip speed that will mobilize grains in our till (which has maximum clast radius of ~4.7 mm) will be ~23.5 m/yr at $N \sim 22$ kPa and increase with increasing N. Notably this prediction is ~1.5x greater than the speed at which we infer sediment flux to initiate for this value of N based on the x-intercept of the aforementioned power law fit in v_{ice}–Q_{sed} space (i.e. ~15.5 m/yr).

A larger percentage of ploughing clasts at the ice-bed interface effectively increases the number of asperities protruding from the ice sole, and thus one anticipates a corresponding increase in coupling between ice and till, qualitatively similar to the velocity steps implemented at $N \sim 22$ kPa (Figure 9b). For velocity steps at $N \sim 50$ kPa and $N \sim 113$ kPa, the observation that coupling appears to have reached a maximum at 100 m/yr conflicts with Zoet and Iverson's model, which suggests that the transition velocity for a given clast size, and by extension v_{max}/v_{ice}, should occur at higher slip speeds for greater values of N. Furthermore, the interface was nearly coupled at $N \sim 22$ kPa and $v_{ice} = 100$ m/yr, which coincides with a minimum mobilized clast radius of 3 mm in Zoet and Iverson's model—a small portion of the overall volume (<3 % of the grains in our till by weight). A confounding factor here could be the influence of sediment entrainment due to regelation infiltration or premelting effects (Meyer et al., 2018) on the frictional properties of the ice-bed interface. Both processes are more effective at higher values of N and could potentially alter the system beyond the mechanics explicitly considered in their formulation by progressively incorporating debris into basal ice. This seems possible since we intermittently observed a thin layer of debris-laden ice ($O(10^{-3}$ m)) in the photographic time series (see Supplement Video 2).

4.4 Glaciological implications

The style of deformation recorded in these experiments illuminates key processes controlling till flux in modern subglacial environments and in relict glacial landscapes. Our main findings—a double-valued relationship between N and Q_{norm} and a positive monotonic relationship between v_{ice} and Q_{sed}—provide a valuable metric to reassess long-standing assumptions regarding the redistribution of sediment at the ice-bed interface during basal slip. Barachyn et al. (2016), for example, suggested that the elongation of soft-sediment bedforms is more efficient at faster sliding velocities due to increased rates of sediment transport from the stoss side (up-glacier) to the lee side (down-glacier) of the feature. In their heuristic model, this association arises due to the influence of two processes working in concert: i) increased pressure on the stoss side of the bump, which causes till to deform faster at higher shear stresses due to an assumed viscous rheology for till, and ii) increased rates of sediment entrainment on the stoss side and melt out on the lee. Our results point to a similar relationship between bedform elongation and slip speed, albeit through a different mechanism. If ice and till are coupled, our results suggest that the slip speed of basal ice is the dominant control on sediment flux in a deforming till bed. Though variations in effective stress influence the flow profile, the difference in Q_{sed} at low and high stresses is subtle compared to changes with slip speed. Rates of till transport along areas of the bed with sustained low effective stresses or slower ice velocities will be depressed, due to the reduced coupling at the interface and slower ice speeds. Conversely, areas of the bed that experience sustained high stresses and fast velocities, such as the stoss side of bedform obstacles, will have elevated Q_{sed}, so long as the driving stress exceeds the shear strength of the till. This should occur even at values of N past the point where shear bands begin to thin, since increased

pressure induced on the adverse slope of the feature dewaters the ice-bed interface (Creyts and Schoof, 2009) and routes water around the bump (Alley et al. 2021). The corresponding reduction in film thickness increases the contact between ice and till on the stoss side, facilitating the transport of sediment near the ice sole down-glacier at a rate proportional to v_{ice}. In the lee, coupling would likely decrease due to the drop in ice pressure, perhaps accentuated by the presence of a water-filled cavity. This process would result in faster rates of till transport and deposition across the obstacle in response to faster slip speeds. Operating in conjunction with the entrainment/melt out hypothesis offered by Barachyn et al. (2016), this mechanism may set up the necessary conditions for v_{ice} to drive bedform elongation.

This tradeoff between areas with contrasting rates of subglacial till transport also has important implications for sliding dynamics. Basal friction is set by the composition of the bed (i.e. till versus bedrock) and its topography, meaning these two parameters dictate the timing and rate of glacier retreat. Glaciers can be underlain by bedrock or completely mantled by a layer of till. However, most likely exist on a continuum between these two end members with some subset of the bed exposed rock and other parts partially covered with sediment (Muto et al, 2019). Empirical sliding laws that relate basal shear stress to slip speed for both hard and soft beds share a similar functional form (Zoet and Iverson, 2020; Helanow et al., 2021) but lead to very different predictions for drag at a given velocity due to the unique physics operating in each. Accounting for variable bed conditions is a necessary level of complexity when parameterizing basal friction (Koellner et al., 2019) but to do so, requires constraint on the percentage of the ice-bed interface overlain by till. This question intrinsically rests on rates at which subglacial till can be deposited or evacuated from the system, which is set by the

relationships we report here, as well as fluvial or debris entrainment processes. Increased rates of transport on the stoss side of obstacles or depressed rates in their lee imply that adverse facing slopes will be swept free of debris, rendering them hard-bedded, and areas in the lee may experience net deposition—in accordance with myriad field observations. The balance of these processes is effectively what determines if an area of the bed is hard or soft.

5 CONCLUSIONS

Soft-bed deformation experiments conducted with subglacial till show clear relationships between sediment flux and both effective stress and sliding velocity. In our experiments, changes in effective stress vary the thickness of a shear band near the ice sole in a double-valued manner, in which sediment flux increases with increasing effective stress to a maximum before reducing at higher stresses. When coupled at the ice-bed interface, the slip speed of basal ice scales the magnitude of the flow profile in deforming till and, by extension, rates of till transport past a threshold slip speed. Increases in both effective stress and sliding velocity both increase the coupling between ice and till. With respect to the influence of sliding velocity, this behavior appears to reflect a transition from form drag to skin friction, in accordance with Zoet and Iverson's (2020) sliding law for glaciers on deformable beds. At steady state, deformation was largely accommodated in a thin band near the ice sole, ~0.7–2.5 cm thick, indicating strain localization is an important consideration when parameterizing till deformation.

Acknowledgments

The work was supported by NSF 2048315. We thank Peter Sobel and Neal Lord for their work designing and constructing the ring shear apparatus. We thank the Wisconsin Geologic and Natural History Survey for conducting the laser diffraction analysis on the till used in these experiments.

Open Research

The data and model files for these experiments are archived at the University of Wisconsin-Madison's Minds@UW repository and can be obtained from the following link: http://digital.library.wisc.edu/1793/82882

REFERENCES

Alley, R. B., Anandakrishnan, S., Dupont, T. K., Parizek, B. R., & Pollard, D. (2007). Effect of sedimentation on ice-sheet grounding-line stability. *Science*, **315**, 1838-1841. https://doi.org/10.1126/science.1138396

Alley, R. B., Holschuh, N., MacAyeal, D. R., Parizek, B. R., Zoet, L., Riverman, K., Stevens, N & GHOST Collaboration. Bedforms of Thwaites Glacier, West Antarctica: Character and Origin. *Journal of Geophysical Research: Earth Surface*, e2021JF006339. https://doi.org/10.1029/2021JF006339.

Alley, R., Lawson, D., Evenson, E., & Larson, G. (2003). Sediment, glaciohydraulic supercooling, and fast glacier flow. *Annals of Glaciology, 36*, 135-141. https://doi.org/10.3189/172756403781816121

Alshibli, K. A., & Sture, S. (1999). Sand shear band thickness measurements by digital imaging techniques. *Journal of computing in civil engineering*, *13*(2), 103-109. https://doi.org/10.1061/(ASCE)0887-3801(1999)13:2(103)

Amirrahmat, S., Druckrey, A. M., Alshibli, K. A., & Al-Raoush, R. I. (2019). Micro shear bands: Precursor for strain localization in sheared granular materials. *Journal of Geotechnical and Geoenvironmental Engineering*, **145**(2), 04018104. https://doi.org/10.1061/(ASCE)GT.1943-5606.0001989

Barranger, Y., Doumalin, P., Dupré, J. C., & Germaneau, A. (2010). Digital image correlation accuracy: influence of kind of speckle and recording setup. In *EPJ web of conferences* (Vol. 6, p. 31002). EDP Sciences. https://doi.org/10.1051/epjconf/20100631002

Barchyn, T. E., Dowling, T. P., Stokes, C. R., & Hugenholtz, C. H. (2016). Subglacial bed form morphology controlled by ice speed and sediment thickness. *Geophysical Research Letters*, **43**(14), 7572-7580. https://doi.org/10.1002/2016GL069558

Bart, P.J., Krogmeier, B. J., Bart, M.P., & S. Tulacyzk, S. (2017). The paradox of a long grounding during West Antarctic Ice Sheet retreat in Ross Sea. *Scientific reports*, **7**, 1-8. https://doi.org/10.1038/s41598-017-01329-8

Bickel, V. T., Manconi, A., & Amann, F. (2018). Quantitative assessment of digital image correlation methods to detect and monitor surface displacements of large slope instabilities. *Remote Sensing*, **10**(6), 865. https://doi.org/10.3390/rs10060865

Boulton, G. S., & Dobbie, K. E. (1998). Slow flow of granular aggregates: the deformation of sediments beneath glaciers. *Philosophical Transactions of the Royal Society of London. Series A: Mathematical, Physical and Engineering Sciences*, *356*(1747), 2713-2745. https://doi.org/10.1098/rsta.1998.0294

Boulton, G. S., & Hindmarsh, R. C. A. (1987). Sediment deformation beneath glaciers: rheology and geological consequences. *Journal of Geophysical Research: Solid Earth*, **92**(B9), 9059-9082. https://doi.org/10.1029/JB092iB09p09059

Clark, C. D. (1993). Mega-scale glacial lineations and cross-cutting ice-flow landforms. *Earth surface processes and landforms*, **18**(1), 1-29. https://doi.org/10.1002/esp.3290180102

Crammond, G., Boyd, S. W., & Dulieu-Barton, J. M. (2013). Speckle pattern quality assessment for digital image correlation. *Optics and Lasers in Engineering*, **51**(12), 1368-1378. https://doi.org/10.1016/j.optlaseng.2013.03.014

Creyts, T. T., & Schoof, C. G. (2009). Drainage through subglacial water sheets. *Journal of Geophysical Research: Earth Surface*, **114**(F4). https://doi.org/10.1029/2008JF001215

Damsgaard, A., Egholm, D. L., Beem, L. H., Tulacyzk, S., Larson, N. K., Piotrowski, J.A., & Siegfried, M. R. (2016). Ice flow dynamics forced by water pressure variations in subglacial granular beds. *Journal of Geophysical Research*, **43**, 12-165. https://doi.org/10.1002/2016GL071579

Damsgaard, A., Egholm, D. L., Piotrowski, J. A., Tulaczyk, S., Larsen, N. K., & Tylmann, K. (2013). Discrete element modeling of subglacial sediment deformation. *Journal of Geophysical Research: Earth Surface*, **118**(4), 2230-2242. https://doi.org/10.1002/2013JF002830

Damsgaard, A., Goren, L., & Suckale, J. (2020). Water pressure fluctuations control variability in sediment flux and slip dynamics beneath glaciers and ice streams. *Communications Earth & Environment*, **1**(1), 1-8. https://doi.org/10.1038/s43247-020-00074-7

Desrues, J., & Viggiani, G. (2004). Strain localization in sand: an overview of the experimental results obtained in Grenoble using stereophotogrammetry. *International Journal for Numerical and Analytical Methods in Geomechanics*, **28**(4), 279-321. https://doi.org/10.1002/nag.338

Evans, D. J. A., Phillips, E. R., Hiemstra, J. F., & Auton, C. A. (2006). Subglacial till: formation, sedimentary characteristics and classification. *Earth-Science Reviews*, **78**(1-2), 115-176. https://doi.org/10.1016/j.earscirev.2006.04.001

Fenistein, D., van de Meent, J.W. & van Hecke, M. (2004). Universal and wide shear zones in granular bulk flow. *Physical review letters*, **92**(9), p.094301.

Fowler, A. C. (2010). The instability theory of drumlin formation applied to Newtonian viscous ice of finite depth. *Proceedings of the Royal Society A: Mathematical, Physical and Engineering Sciences*, **466**(2121), 2673-2694. https://doi.org/10.1098/rspa.2010.0017

Fowler, A. C., & Chapwanya, M. (2014). An instability theory for the formation of ribbed moraine, drumlins and mega-scale glacial lineations. *Proceedings of the Royal Society A: Mathematical, Physical and Engineering Sciences*, **470**(2171), 20140185. https://doi.org/10.1098/rspa.2014.0185

Frost, J. D., DeJong, J. T., & Recalde, M. (2002). Shear failure behavior of granular–continuum interfaces. *Engineering Fracture Mechanics*, **69**(17), 2029-2048. https://doi.org/10.1016/S0013-7944(02)00075-9

Gardiner, B. S., & Tordesillas, A. (2004). Micromechanics of shear bands. *International Journal of Solids and Structures*, **41**(21), 5885-5901. https://doi.org/10.1016/j.ijsolstr.2004.05.051

Gu, X., Huang, M., & Qian, J. (2014). Discrete element modeling of shear band in granular materials. *Theoretical and Applied Fracture Mechanics*, **72**, 37-49. https://doi.org/10.1016/j.tafmec.2014.06.008

Guizar-Sicairos, M., Thurman, S. T., & Fienup, J. R. (2008). Efficient subpixel image registration algorithms. *Optics letters*, **33**(2), 156-158. https://doi.org/10.1364/OL.33.000156

Hasan, A., & Alshibli, K. A. (2010). Experimental assessment of 3D particle-to-particle interaction within sheared sand using synchrotron microtomography. *Géotechnique*, **60**(5), 369-379. https://doi.org/10.1680/geot.2010.60.5.369

Helanow, C., Iverson, N. R., Woodard, J. B., & Zoet, L. K. (2021). A slip law for hard-bedded glaciers derived from observed bed topography. *Science Advances*, **7**(20), eabe7798. https://doi.org/ 10.1126/sciadv.abe7798

Hermann, E., & Barclay, K. (1998). Basal sliding of Ice Stream B, West Antarctica. *Journal of Glaciology, 44*(147), 223-230. https://doi.org/10.3189/S0022143000002562

Hindmarsh, R. (1998). Drumlinization and drumlin-forming instabilities: Viscous till mechanisms. *Journal of Glaciology,* **44**(147), 293-314. https://doi.org/10.3189/S002214300000263X

Howell, D. W., Behringer, R. P., & Veje, C. T. (1999). Fluctuations in granular media. *Chaos: An Interdisciplinary Journal of Nonlinear Science*, **9**(3), 559-572. https://doi.org/10.1063/1.166430

Imseeh, W. H., Alshibli, K. A., & Al-Raoush, R. I. (2020). Discrepancy in the critical state void ratio of poorly graded sand due to shear strain localization. *Journal of Geotechnical and Geoenvironmental Engineering*, **146**(8), 04020066. https://doi.org/10.1061/(ASCE)GT.1943-5606.0002280

Iverson, N. R. (2010). Shear resistance and continuity of subglacial till: hydrology rules. *Journal of Glaciology*, **56**(200), 1104-1114. https://doi.org/10.3189/002214311796406220

Iverson, N., Hooyer, T., Fischer, U., Cohen, D., Moore, P., Jackson, M., Lappegard, G., & Kohler, J. (2007). Soft-bed experiments beneath Engabreen, Norway:regelation infiltration, basal slip and bed deformation. *Journal of Glaciology*, **53**(182), 323-340. https://doi.org/10.3189/002214307783258431

Iverson, N., & Iverson, R. (2001). Distributed shear of subglacial till due to Coulomb slip. *Journal of Glaciology, 47*(158), 481-488. https://doi.org/10.3189/172756501781832115

Iverson, N., Hooyer, T., & Baker, R. (1998). Ring-shear studies of till deformation: Coulomb-plastic behavior and distributed strain in glacier beds. *Journal of Glaciology,* **44**(148), 634-642. https://doi.org/10.3189/S0022143000002136

Iwashita, K., & Oda, M. (2000). Micro-deformation mechanism of shear banding process based on modified distinct element method. *Powder technology*, **109**(1-3), 192-205. https://doi.org/10.1016/S0032-5910(99)00236-

Kamb, B. (1991). Rheological nonlinearity and flow instability in the deforming bed mechanism of ice stream motion. *Journal of Geophysical Research: Solid Earth*, **96**(B10), 16585-16595. https://doi.org/10.1029/91JB00946

Kamb, B., (2001). Basal zone of the West Antarctic ice streams and its role in lubrication of their rapid motion. *The West Antarctic ice sheet: behavior and environment* **77**, 157-199. https://doi.org/10.1029/AR077p0157

King, E. C., Hindmarsh, R.C., & Stokes, C.R. (2009). Formation of mega-scale glacial lineations observed beneath a West Antarctic ice stream. *Nature. Geoscience*, **2**(8), 585-588. https://doi.org/10.1038/ngeo581

Koellner, S., Parizek, B. R., Alley, R. B., Muto, A., & Holschuh, N. (2019). The impact of spatially-variable basal properties on outlet glacier flow. *Earth and Planetary Science Letters*, **515**, 200-208. https://doi.org/10.1016/j.epsl.2019.03.026

Meng, L., Jin, G., & Yao, X. (2006). Errors caused by misalignment of the optical camera axis and the object surface in the DSCM. *Journal of Tsinghua University*, **46**(11), 1930. https://doi.org/CNKI:SUN:QHXB.0.2006-11-034

Meyer, C. R., Downey, A. S., & Rempel, A. W. (2018). Freeze-on limits bed strength beneath sliding glaciers. *Nature communications*, 9(1), 1-6. https://doi.org/10.1038/s41467-018-05716-1

Mickelson, D. M., & Syverson, K. M. (1997). *Quaternary geology of Ozaukee and Washington counties, Wisconsin* (Vol. 91). University of Wisconsin—Extension, Wisconsin Geological and Natural History Survey.

Muto, A., Anandakrishnan, S., Alley, R. B., Horgan, H. J., Parizek, B. R., Koellner, S., ... & Holschuh, N. (2019). Relating bed character and subglacial morphology using seismic data from Thwaites Glacier, West Antarctica. *Earth and Planetary Science Letters*, **507**, 199-206. https://doi.org/10.1016/j.epsl.2018.12.008

Mueth, D. M., Debregeas, G. F., Karczmar, G. S., Eng, P. J., Nagel, S. R., & Jaeger, H. M. (2000). Signatures of granular microstructure in dense shear flows. *Nature*, **406**(6794), 385-389. https://doi.org/10.1038/35019032

Niedostatkiewicz, M., Lesniewska, D., & Tejchman, J. (2011). Experimental analysis of shear zone patterns in cohesionless for earth pressure problems using particle image velocimetry. *Strain*, **47**, 218-231. https://doi.org/10.1111/j.1475-1305.2010.00761.x

Oda, M., & Kazama, H. (1998). Microstructure of shear bands and its relation to the mechanisms of dilatancy and failure of dense granular soils. *Geotechnique*, **48**(4), 465-481. https://doi.org/10.1680/geot.1998.48.4.465

Piotrowski, J. A., Mickelson, D. M., Tulaczyk, S., Krzyszkowski, D., & Junge, F. W. (2001). Were deforming subglacial beds beneath past ice sheets really widespread?. *Quaternary International*, **86**(1), 139-150. https://doi.org/10.1016/S1040-6182(01)00056-8

Rattez, H., Shi, Y., Sac-Morane, A., Klaeyle, T., Mielniczuk, B., & Veveakis, M. (2020). Effect of grain size distribution on the shear band thickness evolution in sand. *Géotechnique*, 1-14. https://doi.org/10.1680/jgeot.20.P.120

Rechenmacher, A. L. (2006). Grain-scale processes governing shear band initiation and evolution in sands. *Journal of the Mechanics and Physics of Solids*, **54**(1), 22-45. https://doi.org/10.1016/j.jmps.2005.08.009

Rechenmacher, A., Abedi, S., & Chupin, O. (2010). Evolution of force chains in shear bands in sands. *Géotechnique*, **60**(5), 343-351. https://doi.org/10.1680/geot.2010.60.5.343

Rechenmacher, A. L., & Finno, R. J. (2004). Digital image correlation to evaluate shear banding in dilative sands. *Geotechnical Testing Journal*, **27**(1), 13-22. https://doi.org/10.1520/GTJ11263J

Rempel, A. W. (2008). A theory for ice-till interactions and sediment entrainment beneath glaciers. *Journal of Geophysical Research: Earth Surface*, **113**(F1). https://doi.org/10.1029/2007JF000870

Roy, S., Scheper, B.J., Polman, H., Thornton, A.R., Tunuguntla, D.R., Luding, S. & Weinhart, T., 2019, Surface flow profiles for dry and wet granular materials by Particle Tracking Velocimetry; the effect of wall roughness. *The European Physical Journal E*, **42**(2). pp.1-14.

Scott, L. Ridgeway. (2011) Numerical Analysis. *Princeton University Press*. p. 204.

Schall, P., & Van Hecke, M. (2010). Shear bands in matter with granularity. *Annual Review of Fluid Mechanics*, **42**, 67-88. https://doi.org/10.1146/annurev-fluid-121108-145544

Schoof, C. (2007). Pressure-dependent viscosity and interfacial instability in coupled ice–sediment flow. *Journal of Fluid Mechanics,* **570**, 227-252. https://doi.org/10.1017/S0022112006002874

Simkins, L.M., Greenwood, S.L. & Anderson, J.B. (2018). Diagnosing ice sheet grounding line stability from landform morphology. *The Cryosphere*, **12**(8), 2707-2726. https://doi.org/10.5194/tc-12-2707-2018

Soltanbeigi, B., Altunbas, A., Gezgin, A. T., & Cinicioglu, O. (2020). Determination of passive failure surface geometry for cohesionless backfills. *Periodica Polytechnica Civil Engineering*, **64**(4), 1100-1110. https://doi.org/10.3311/PPci.14241

Stokes, C. R., & Clark, C. D. (2002). Are long subglacial bedforms indicative of fast ice flow?. *Boreas*, **31**(3), 239-249. https://doi.org/10.1111/j.1502-3885.2002.tb01070.x

Tang, H., Dong, Y., Chu, X., & Zhang, X. (2016). The influence of particle rolling and imperfections on the formation of shear bands in granular material. *Granular Matter*, **18**(1), 12. https://doi.org/10.1007/s10035-016-0607-3

Tian, J., Liu, E., & He, C. (2020). Shear band analysis of granular materials considering effects of particle shape. *Acta Mechanica*, **231**(11), 4445-4461. https://doi.org/10.1007/s00707-020-02771-y

Tordesillas, A. (2007). Force chain buckling, unjamming transitions and shear banding in dense granular assemblies. *Philosophical Magazine*, **87**(32), 4987-5016. https://doi.org/10.1080/14786430701594848

Tulaczyk, S., Kamb, B., Scherer, R.P., & Engelhardt, H.F. (1998). Sedimentary processes at the base of a West Antarctic ice stream; constraints from textural and compositional properties of subglacial debris. *Journal of Sedimentary Research*, **68**(3). pp.487-496.

Tulaczyk, S. (1999). Ice sliding over weak, fine-grained tills: dependence of ice-till interactions on till granulometry. *Special Papers of the Geological Society of America*, 159-178. https://doi.org/10.1130/0-8137-2337-X.159

Tulaczyk, S., Kamb, W. B., & Engelhardt, H. F. (2000). Basal mechanics of ice stream B, West Antarctica: 1. Till mechanics. *Journal of Geophysical Research: Solid Earth*, **105**(B1), 463-481. https://doi.org/10.1029/1999JB900329

Tulaczyk, S. M., Scherer, R. P., & Clark, C. D. (2001). A ploughing model for the origin of weak tills beneath ice streams: a qualitative treatment. *Quaternary International*, **86**(1), 59-70. https://doi.org/10.1016/S1040-6182(01)00050-7

Wu, P. K., Matsushima, K., & Tatsuoka, F. (2008). Effects of specimen size and some other factors on the strength and deformation of granular soil in direct shear tests. *Geotechnical Testing Journal*, **31**(1), 45-64. https://doi.org/ 10.1520/GTJ10077

Zheng, H., Wang, D., Tong, X., Li, L., & Behringer, R. P. (2019). Granular scale responses in the shear band region. *Granular Matter*, **21**(4), 1-6. https://doi.org/10.1007/s10035-019-0958-7

Zhu, H., Nguyen, H. N., Nicot, F., & Darve, F. (2016). On a common critical state in localized and diffuse failure modes. *Journal of the Mechanics and Physics of Solids*, **95**, 112-131. https://doi.org/10.1016/j.jmps.2016.05.026

Zoet, L. K., & Iverson, N. R. (2020). A slip law for glaciers on deformable beds. *Science*, **368**(6486), 76-78. https://doi.org/10.1126/science.aaz1183

Zoet, L. K., Rawling III, J. E., Woodard, J. B., Barrette, N., & Mickelson, D. M. (2021). Factors that contribute to the elongation of drumlins beneath the Green Bay Lobe, Laurentide Ice Sheet. *Earth Surface Processes and Landforms* **46**(13) *2540-2550*. https://doi.org/10.1002/esp.5192

Chapter 2. Experimental constraints on subglacial rock friction

D. D. Hansen[1], L. K. Zoet[1]

[1]*Department of Geosciences, University of Wisconsin-Madison, Madison, WI*

ABSTRACT

Subglacial rock friction is an important control on the sliding dynamics and erosive potential of hard-bedded glaciers, yet it remains largely unconstrained. To explore the relative influence of basal melt rate, effective stress, and ice temperature on frictional resistance, we conducted abrasion experiments in which limestone beds were slid beneath a fixed slab of ice laden with granitic rock fragments. Shear stress scales linearly with melt rate and cryostatic stress, confirming that both viscous drag and effective stress are first order controls on the contact force in drained conditions. Furthermore, temperature gradients in the ice increase the contribution of viscous drag on shear stresses. In all experiments, the relationship between melt rate and shear stress is best explained by a model that accounts for regelation and viscous creep on the bed-normal drag force. We interpret this to mean fluid flow around entrained clasts contributed to basal drag even at subfreezing temperatures. Incorporating premelting dynamics into the Watts/Hallet model for subglacial rock friction, we find that the predicted debris-bed drag decreases by approximately an order of magnitude, with a corresponding ~3.5x increase in the transition radius. This is lower than we observe for ice slightly below the pressure melting point.

1 INTRODUCTION

Friction between entrained basal debris and the bed affects the erosion rates (Schweizer and Iken, 1992; Hallet and others, 1996; Koppes and Hallet, 2006; Herman and others, 2015; Koppes and others, 2015), sliding speed (Hallet, 1981; Shoemaker, 1988), and slip stability of glaciers (Zoet and others, 2013; McCarthy and others 2017; Lipovski and others, 2019). Basal ice is typically assumed to be debris-free in glacier flow models, meaning basal resistance arises solely from ice deformation around bedrock obstacles (Lliboutry, 1968; Iken, 1981; Nye, 1969; Zoet and Iverson, 2015, 2016). However, observation shows that glaciers transport substantial bedload (Kirkbride, 2002), and theory and field measurements indicate subglacial rock friction may be significant, albeit poorly constrained (Iverson and others, 2003; Cohen and others, 2005; Iverson and others, 2019 in this issue).

A central assumption in theories describing subglacial rock friction is that inclusions in ice are surrounded entirely by a thin water film (Boulton, 1974; Hallet 1979b, 1981; Hindmarsh, 1996; Cohen and others, 2005; Emerson and Rempel, 2007). For temperate ice, classic regelation and creep theory predicts the presence of a film due to ice pressure melting along grain boundaries (Nye, 1969, 1973; Kamb, 1970). However, considerations of premelting indicate a liquid film exists even at subfreezing temperatures (Gilpin, 1979; Dash and others, 1995; Rempel and Worster, 1999; Rempel and others, 2001; Rempel and others, 2004; Dash and others, 2006). Since ice is nowhere in contact with the clast, stresses in the ice must be transmitted to the rock through the fluid surrounding the clast. Fundamentally, discrepancies between interfacial models stem from their assumptions regarding the distribution of water pressure along the clast boundary and its controlling mechanisms.

To date, the competing models of Boulton (1974) and Hallet (1979b, 1981) have driven theoretical framing of subglacial rock friction (Fig. 1). Boulton (1974) first proposed that the bed-normal contact force beneath an abrading clast, F_c, is the product of the effective pressure in the film, N (i.e. cryostatic pressure, P_i, minus the water pressure, P_l) and the surface area of the particle, A, such that

$$F_c = F_{eff} = AN. \quad (1)$$

where F_{eff} is the contact force due to effective stress acting on the clast. For a spherical particle in contact with the bed, $A = \pi(2tr\text{-}t^2)$, where r is the radius and t is the thickness of a water film that separates the ice from the bedrock. However, as Hallet (1979b, 1981) recognized, this model neglects the contribution of the buoyant force due to gravity, F_b, and the drag force, F_d, induced as ice creeps and/or regelates around suspended particles. Accounting for these additional components, the bed-normal contact force is more completely expressed:

$$F_c = F_b + F_d + F_{eff}. \quad (2)$$

In this later formulation, $F_{eff} = 0$ is implicitly assumed, implying that deviatoric stresses arise only from the combined influence of F_b and F_d and that cryostatic stress (and by extension glacier thickness) has no bearing on the erosive potential or frictional properties of basal debris. For small clasts ($r < 0.5$ m), F_b is negligible (Hallet, 1979b). To quantify the drag force, Hallet adapted Watts's (1974) analytic solution for a spherical inclusion moving through temperate "Newtonian" ice by regelation and creep to a half space, such that

$$F_d = \frac{\Phi 4\pi\eta_i u_v r^3}{r_*^2 + r^2} \quad (3)$$

where Φ is a bed influence factor, η_i is the viscosity of ice, u_v is the bed-normal ice velocity, r is the radius of the particle, and r_* is a transition radius analogous to the controlling wavelength in glacier sliding. Watts (1974) defines the transition radius as

$$r_* = \left(\frac{3\eta_i\, CK}{\rho_i \mathcal{L}}\right)^{\frac{1}{2}} \tag{4}$$

where C is the Clapeyron slope, K is the mean thermal conductivity of ice and rock, and $\rho_i \mathcal{L}$ is the volumetric latent heat of fusion for ice.

The prefactor Φ in Equation 3 corrects for the influence of a bed on the viscous flow field around a clast. Hallet (1981) based his initial estimate of $\Phi = 2.4$ on the analysis of Goren (1970). However, the boundary conditions prescribed therein are not characteristic of the subglacial environment (Cohen and others, 2005), and empirical evidence regarding the magnitude of this parameter is limited and often contradictory. For example, Iverson (1990) observed Φ = 0-5 for non-idealized granite clasts during laboratory abrasion experiments. Byers and others (2012) found that for the case of a stationary spherical inclusion in contact with the bed, F_d was approximately twice the Stokes drag force induced by the flow of Newtonian ice around a slippery sphere (i.e. $\Phi = 1.8$). And Lee and Rutter (2004) found $\Phi \approx 10$ was necessary to reconcile their observations with theory when comparing experimental rock-on-rock wear data with the suspended sediment yield in a proglacial stream.

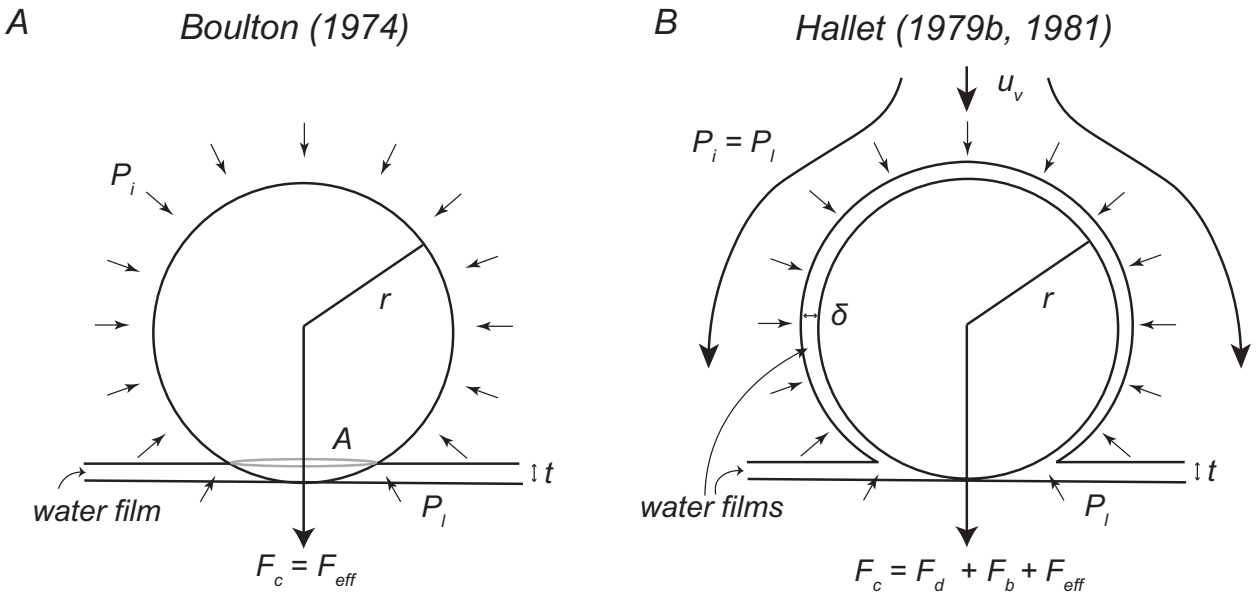

Fig. 1. Conceptual models developed by A) Boulton (1974) and B) Hallet (1979b, 1981) to describe the bed-normal contact-force beneath an abrading clast. A water film of thickness t separates ice from bed, and a second film envelopes the clast with thickness δ in Hallet's (1979b, 1981) model. In Boulton's (1974) model (A), the film around the clast is assumed to be sufficiently thin so that liquid pressure in it is effectively zero. F_{eff} is the force due to effective stress, F_d is the viscous drag force, F_b is the buoyant force due to gravity, P_l is the water pressure in the films, P_i is the cryostatic stress, r is the radius of the clast, u_v is the vertical ice velocity and A is the cross sectional area of the clast at height t. The schematic is adapted from Byers and others (2012).

In subsequent years, Hallet's model (1979b, 1981) has been widely implemented in glacier erosion models (Anderson, 2014; Beaud and others, 2014; Herman and others, 2011; Egholm and others, 2017; Ugelvig and Egholm, 2018), and available experimental data supports a linear relationship between F_c and u_v as predicted (Iverson, 1990; Byers and others, 2012). Although Hallet's model identified key controls on debris-bed friction, numerous lines of evidence indicate the problem remains unresolved. As Hindmarsh (1996) and Morris (1979) address in considerable detail, mathematical inconsistencies arise when Watts's (1974) analytic solution is considered in the context of common subglacial boundary conditions. Myriad

complicating factors, including the presence of a far field lubricating film, bed transmissivity, the formation of cavities along clast boundaries, impurities in the ice, incomplete refreezing during regelation, high debris concentrations, temperature fluctuations in basal ice, and interfacial melting are pervasive in nature and likely preclude this model from being universally applicable. Moreover, not all available data agrees with this model's predictions. Experiments conducted by Emerson and Rempel (2007) show a statistically significant relationship between cryostatic stress and basal drag for sand-sized particles in a melt-dominated regime, and pressure sensors emplaced beneath Engabreen Glacier recorded anomalously high shear stresses that also covaried with effective stress (Iverson and others, 2003; Cohen and others, 2005). Thus, it seems that a more nuanced treatment of subglacial rock friction is needed in order to capture the complexities of this system.

This lingering uncertainty provides an impetus to revisit this classic problem and better constrain the mechanisms controlling debris-bed drag. To this end, we designed laboratory experiments to simulate glacial abrasion under a range of realistic subglacial conditions, such as variable cryostatic stresses, basal melt rates, and ice temperatures. We tested the relative influence of these controlling parameters on basal shear stress using non-idealized clasts. In the following sections, we incorporate the effects of premelting into the existing Watts/Hallet model for subglacial abrasion and then present our methodology and experimental results. Finally, we weigh our results against theory.

1.1 The effect of premelt on debris-bed contact forces

Recently, Rempel and Meyer (2019) postulated that premelting increases both the rate of regelation by an order of magnitude and the controlling obstacle size in glacier sliding by a factor

of ~3.5. Given that basal drag in the Watts/Hallet model is a function of the regelation rate, this may have important implications for the drag force imparted against an entrained clast. Incorporating the same premelting condition into Watts' (1974) original analysis, we find that it predicts a significant decrease in F_d. The steps of this derivation are detailed in the Appendix, Equations A1-A10. We obtain a modified expression for drag force, F_d, imparted against the sphere,

$$F_d = \frac{4\pi\eta_i u_v r^3}{r_*^2 + r^2}, \tag{5}$$

where

$$r_* = \left(\frac{\rho_l}{\rho_l - \rho_i}\frac{3\eta_i CK}{\rho_i \mathcal{L}}\right)^{\frac{1}{2}}. \tag{6}$$

Here ρ_l represents the density of liquid water, and ρ_i is the density of ice.

Notably, we find that the transition radius, r_*, is approximately $\sqrt{\rho_l/(\rho_l - \rho_i)} \approx 3.5$ times larger than the transition radius predicted by Watts's (1974) original analysis (Equation 4). Fig. 2 juxtaposes the relationship between clast radius and drag force predicted for both solutions, assuming $\eta_i = 3.15 \times 10^{12}$ Pa s, u_v = 500 mm a^{-1}, ρ_l = 1000 kg m^{-3}, ρ_i = 917 kg m^{-3}, $\mathcal{L}$ =3.3 x 10^5 J kg^{-1}, C = 0.074 K MPa^{-1}, K = 2.5 W m^{-1} K^{-1}.

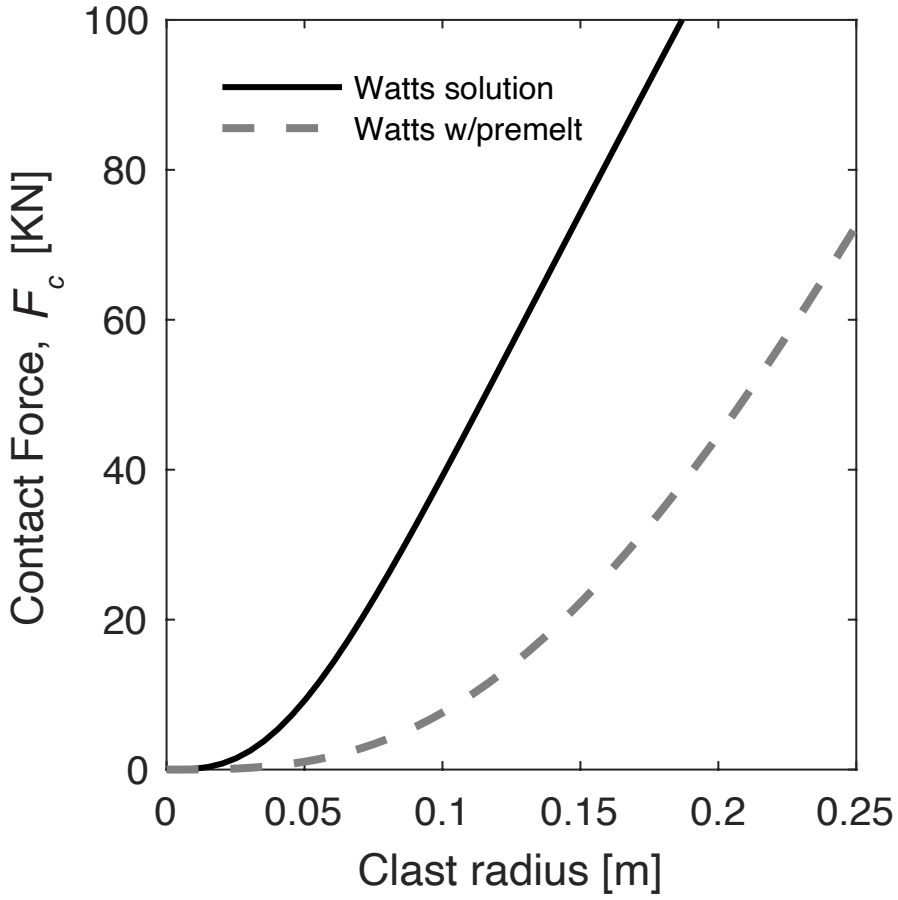

Fig. 2. A comparison of clast radius versus contact force for the Watts/Hallet model and a solution that accounts for the effects of premelting on regelation. Incorporating premelting dynamics into the Watts/Hallet model significantly decreases the expected viscous drag force imparted against an abrading clast below the transition size radius.

A decrease in the drag force due to premelting may have major implications for the capacity of entrained debris to resist glacier sliding or erode bedrock, especially if $F_{eff} = 0$. Hallet's model predicts relatively low shear stresses for typical bed loads and subglacial conditions (Hallet, 1979b; 1981; Cohen and others, 2005); however, as seen Fig. 2, debris-bed drag decreases significantly when the scaling factor is introduced. Furthermore, a ~3.5x increase in the transition radius would limit the number of available bed tools capable of imparting

significant force to the bed. For example, the transition radius for a granite clast increases from $r_* \approx 11$ cm to $r_* \approx 38.5$ cm. Given a typical size distribution, a large percentage of basal debris would fall below this size class (Haldorsen, 1981; Baltrunas and others, 2009).

2 METHODS

We simulated glacial abrasion with a direct shear device (Fig. 3A) by sliding a 10 cm x 10 cm limestone bed beneath a fixed slab of ice laden with twelve granitic rock fragments. To construct the ice slab, de-ionized (DI) water was first frozen, crushed, and sieved to obtain a mixture of ice granules ranging in size from 2.0-6.3 mm. Encasing these granules in an ice matrix (Fig. 3B), we approximated a randomly oriented agglomeration of interlocking ice crystals, analogous to glacier ice. Granitic rock fragments selected based on size and overall shape (Fig. 3E). Standard operating procedure dictates that particles must be sufficiently small to inhibit wall effects, which typically corresponds to a diameter one-tenth the width of the sample chamber (Iverson, 1990) and at least half its height (Gudmundsson, 1997; Zoet and Iverson, 2016). We chose angular clasts with a relatively high sphericity and mean diameters between 9-11 mm. The rock fragments were arrayed in a square insulating fiberglass sample chamber wrapped in foam tape; ice granules were layered on top; chilled DI water was added to fill in the void space; and the arrangement was frozen in a deep freezer. In the bottom half of the sample chamber, a smooth, flat limestone bed was emplaced, so that its top surface was flush with the adjacent edges and the overriding section can slide freely over it (Fig. 3C). The height of these beds varied slightly (generally less than +/-0.5 mm) between experiments, due to their construction or as a result of sanding their surface between runs. If the height of the bed was lower than the walls of the sample chamber, paper spacers were placed beneath the limestone bed to make its edges flush

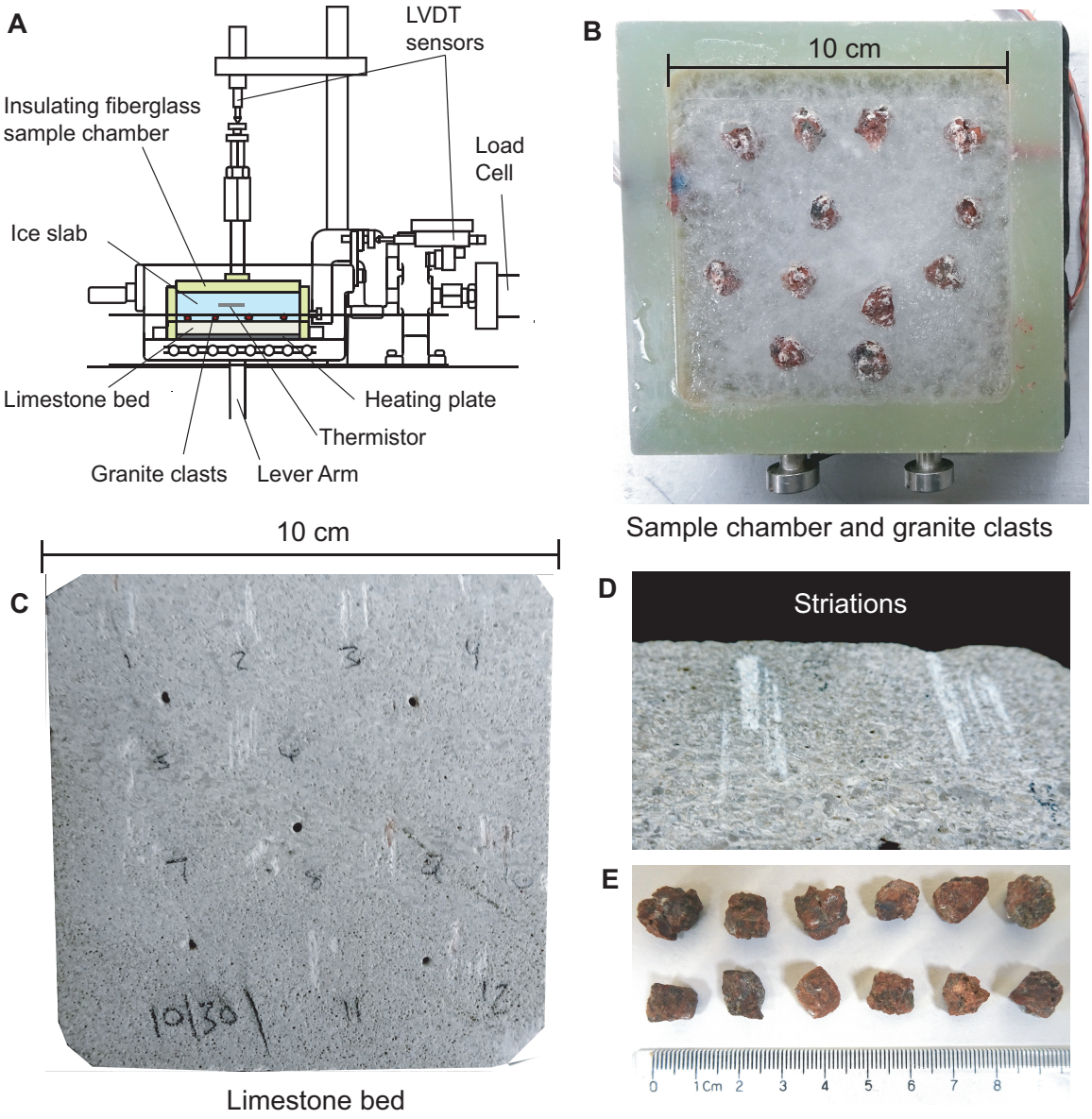

Fig. 3. A) A schematic of the modified direct shear device, B) debris-laden ice within the insulating sample chamber, C) a typical limestone bed at the conclusion of an experiment (Note that multiple striations are common for a single abrading rock), D) striations, and E) twelve representative granite clasts used in our experiments.

with the adjacent walls. Five small holes (< 4mm) were drilled into the bed to facilitate drainage of melt water during the experiment.

Once the sample chamber was assembled, it was loaded into the direct shear device. Vertical stress was applied to the top pressure plate by weights hung from the lever arm. The apparatus was then left to sit overnight, allowing the clasts to fully indent the bed and the ice to adjust under the load. To set the melt rate at the ice-bed interface (and by extension the vertical flow of ice toward the bed), we varied the power output to a heating plate installed into the bed. A glass bead thermistor, installed in the ice ~1 cm from the ice-bed interface, recorded the temperature of the ice as it warmed, and a linear variable displacement transducer (LVDT) measured the downward vertical displacement of the pressure plate as the ice melted at the interface. Because the heat flux was concentrated at the base of the ice and the ambient temperature of the freezer was held below the pressure melting point (PMP), we assume the total vertical displacement to approximately equal the thickness of the ice melted at the interface. Once the melt rate reached a relative steady state (> 3 hours), the shear ram was engaged at a prescribed velocity of 0.1 mm min^{-1} for a distance of ~1 cm.

The relative influence of vertical ice velocity and effective stress on basal drag was assessed by conducting experiments at four normal stresses, σ_N, (four runs at 118 kPa, five runs at 294 kPa, five runs at 588 kPa, and three runs at 784 kPa) over a range of melt rates. During the experiments conducted at 294 kPa, 588 kPa, and 784 kPa, the ambient freezer temperature was set to approximately -0.9 ºC (±0.7 ºC). However, for the runs conducted at 118 kPa, an insulating case was built to house the direct shear in order to achieve smaller temperature gradients in the ice. The freezer temperature was set slightly colder at approximately -1.5 ºC (±0.7 ºC) to

compensate for heat retention within the insulating box. We set the melt rates between ~580-3000 mm a^{-1}, on the order (O(10^2 mm a^{-1}) to O(10^3 mm a^{-1})) expected for high rates of convergence expected on the stoss side of small bedrock obstacles (Hallet, 1979b; Iverson, 1990).

The shear stresses measured in our experiments represent friction between granite clasts and the bed and friction between clean ice and the bed. To assess the relative contribution of these two factors to the overall drag, we conducted experiments using only clean ice or only granite clasts respectively. The background drag exerted by clean ice was determined by running experiments over a range of normal stresses, following the experimental protocol outlined above. We note that all σ_N =118 kPa and σ_N =784 kPa runs used the same limestone slabs as their respective background stress test, whereas the background stress for σ_N = 294 kPa and σ_N = 588 kPa was estimated using different beds. To determine the rock-on-rock frictional coefficient, twelve granite clasts were cast in epoxy resin and slid over a limestone bed at three normal stresses. Only the individual points of the indenting clasts contacted the bed in the rock-on-rock runs.

3 RESULTS

During each experiment, shear stresses increased rapidly to a maximum before reaching a relative steady state or gradually declining for the duration of the run (Fig. 4). Fluctuations in shear stress occurred at timescales ranging from seconds to minutes, likely representing individual stick slip cycles or transient changes bed-normal contact forces, F_c (Emerson and Rempel, 2007; Zoet and others, 2013). Similarly, the rate of vertical displacement of the top platen could vary on comparable timescales. Shear stresses presented in this study represent

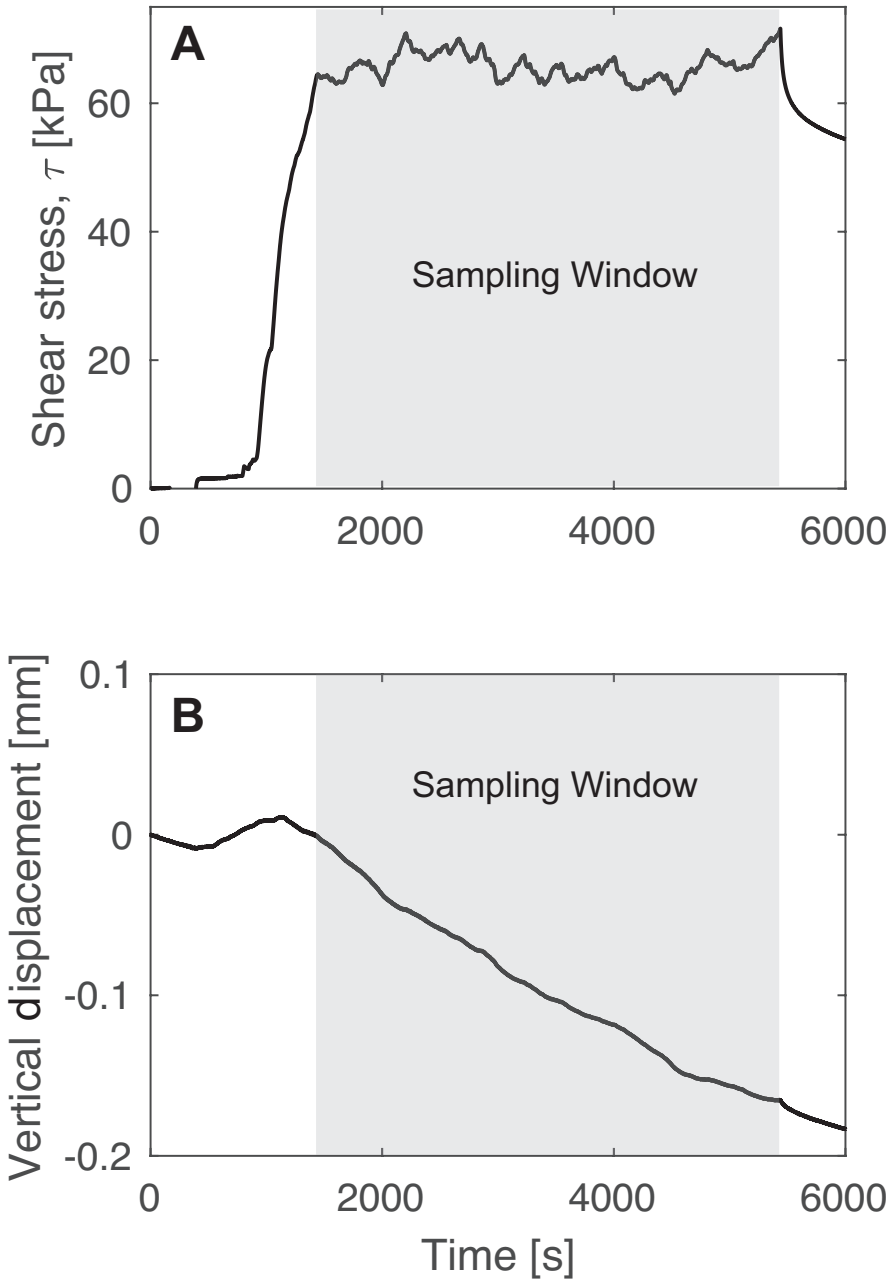

Fig 4. a) Sample shear stress data for a representative experiment. The applied normal load was σ_N = 118 kPa. We calculate the average shear stress from 1500 s to the end of the experiment for most runs. The sampling window here consists of ~3800 unique datum. Corresponding displacement data for the top platen of the sample chamber is shown in 4B. Melt rate is calculated as the average vertical rate of displacement over the same sampling window using an ordinary least squares regression.

mean values calculated from 1500 s to the conclusion of the experiment when possible (Fig. 4A). Melt rates are calculated as the slope of a linear regression through vertical displacement data over the same time window (Fig. 4B). The number of independent data points used for each calculation varied between runs, but generally the sample size was greater than 3500, which ensured small standard errors (Table 1)

Cavities formed sporadically in the lee of clasts in numerous experiments (0-3 per run; Fig. 5), but they were not a dominant feature and did not appear to affect the drag appreciably under our specific experimental conditions. Iverson (1990) reached a similar conclusion after noting comparable features in his experiments. However, this does not preclude the possibility that cavities may be more significant when they occur with greater frequency—merely that their impact on the force balance on a couple clasts did not dominate the overall drag. At higher melt rates, warmer ice temperatures, or longer displacements, we anticipate these features would be more pervasive and could potentially have a greater impact on basal shear stress. In several runs at very high melt rates, we observed large cavities that appeared to have a more significant impact; however, we do not include them in our results as the experimental conditions during those runs are outside the scope of the present study.

Fig. 5. The morphology of a typical cavity that formed along the lee side of an abrading clast, cast in clay. In the experiments presented herein, similar cavities formed sporadically but did not significantly impact basal drag.

3.1 Friction tests

We obtained the frictional coefficients for the clean ice-on-limestone and granite-on-limestone tests by computing the slope of a linear regression through each dataset in $\sigma_N - \tau$ space. For both sets of experiments, shear stress increased linearly with increasing normal stress in a manner characteristic of Coulomb friction. For the granite-on-limestone runs, the frictional coefficient is $\mu_{G\text{-}L} = 0.72$ ($R^2 = 0.99$), which reflects the large hardness contrast between the two lithologies (Drewry, 1986, p.52-53). For the clean ice-on-limestone experiments, the background coefficient of friction is taken to be $\mu_{I\text{-}L} = 0.14$ ($R^2 = 0.86$) for the runs conducted at σ_N = 294-784 kPa and $\mu_{I\text{-}L} = 0.19$ ($R^2 = 0.99$) for the runs at σ_N = 118 kPa. These values are high given that drag

between clean, temperate ice and a level bed is typically assumed to be zero. However, a number of factors likely contributed to these elevated values: 1) the friction between sample chamber walls, 2) edge effects, 3) micro-roughness elements on the rocks surface, and 4) the relatively short displacements in our experiments. Care was taken to ensure that the edges of the limestone bed were flush with the sample chamber. However, in some experiments, the bed remained slightly lower than the surrounding walls (< ~0.5 mm), introducing a component of viscous drag to the resistive stresses as ice overrode this lip. Furthermore, as the ice sat overnight under load, it could creep into available void spaces around the edges of the slabs such that when the ram was engaged, the ice in the void space would initially shear, adding another small viscous drag component.

The maximum height of the micro-roughness elements on the surface of the limestone bed, imaged using a white-light interferometer, was on the order of ~10^2 microns. If the amplitude of these features exceeded the thickness of the lubricating film at the ice-bed interface, they would act as asperities to resist sliding. We estimate an upper bound for film thickness by calculating the thickness of a film separating temperate ice from an impermeable disc at the melt rates and normal stresses used in our experiments (Equation A7 in Emerson and Rempel (2007)). Film thickness in our experiments were likely thinner due to the permeability of the rock. We find that for all experimental conditions, the estimated thickness of the lubricating film (O(10^{-6} - 10^{-7} m) is likely smaller than the amplitude of the larger micro-roughness elements. Therefore, regelation past these features likely contributed to the measured background shear stress. Finally, we note that in the clean ice runs, the shear stress occasionally decreased from a maximum value toward a lower steady state, causing the calculated averages to potentially represent a value

slightly higher than a true steady state. We attempt to account for the influence of all these mechanisms in all our experiments by subtracting a background drag from the observed shear stresses to isolate the drag, τ, imparted by the entrained clasts against the bed (i.e. $\tau = \tau_{observed} - \mu_{IL} \sigma_N$).

3.2 Temperature gradients in the ice

As stated, experiments were conducted under two thermal regimes, in which 1) the sample chamber was exposed to the ambient freezer temperature (T_{amb}=-0.9 ±0.7 ºC for σ_N = 294-784 kPa), or 2) the direct shear was housed in an insulating box (σ_N = 118 kPa) to minimize temperature gradients in the ice sample (σ_N = 118 kPa). Figure 6 shows how basal melt rate changes in response to the vertical temperature gradient, *dT/dz*, in the ice for runs where temperature data were available. The thermal gradient reflects the change in temperature, *dT*, per unit distance, *dz*, from the PMP at a given σ_N using the Clapeyron slope for air-free ice, C = 0.074 °K MPa^{-1}. At the ice-bed interface, the ice temperature was at PMP in our experiments, as evidenced by the visible melt observed along the boundaries of the sample chamber and the continuous vertical displacement of the top pressure plate once the heating plate warmed. We calculate the gradient as the difference between PMP and the mean temperature recorded over the duration of the experiment at a known position in the ice divided by the distance of the thermistor from the interface. We achieved shallower thermal gradients in the ice by insulating the sample chamber. Equipment malfunctions with the thermistor prevented us from collecting temperature data during all experiments, but 65% of runs were successfully recorded. Regression models show that the melt rates recorded in our experiments scale linearly with *dT/dz* for both thermal regimes (Fig. 6).

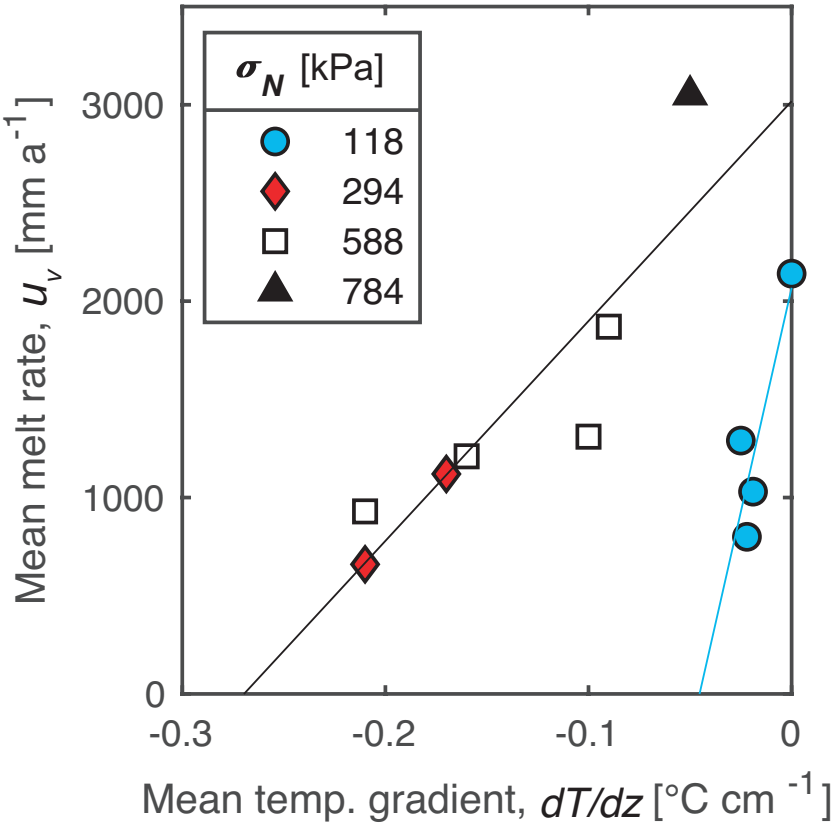

Fig. 6. Vertical temperature gradients, *dT/dz*, observed in the ice slab scale linearly with basal melt rate, u_v. When the sample chamber was exposed to the ambient freezer temperature (σ_N = 294-784 kPa), the two parameters covary according to the relationship u_v = 11194 *dT/dz* +3018 (R^2 = 0.82). With the addition of the insulating box (σ_N = 118 kPa), a linear regression model predicts u_v = 45621 *dT/dz* +2068 (R^2 = 0.77). Standard errors for both parameters are smaller than the bounds of the plotted data points (Table 1).

3.3 Basal melt rate and effective stress influence the contact force

In all experiments shear stress, τ, appears to scale linearly with basal melt rate, u_v (Fig. 7A), indicating the viscous drag force, F_d, is a control on debris-bed friction. For runs conducted at σ_N = 294-784 kPa, (steeper *dT/dz)* data conform to single linear trend, where $\tau = 0.057u_v + 35$ (R^2 = 0.85). However, the slope of the linear regression computed for the σ_N = 118 kPa data (shallower

dT/dz) is notably smaller ($\tau = 0.016\ u_v + 20$; $R^2 = 0.90$). Table 1 lists our measurements and associated uncertainty. Because the calculated standard errors for u_v and τ are approximately 2-3 orders of magnitude smaller than the actual reported measurements, we assume their influence on the fit is negligible and therefore neglect to propagate these uncertainties in the regression.

Given that the contact force, F_c represents the contribution of both effective stress, F_{eff}, and the drag force, F_d, (Equation 2) one anticipates that if F_{eff} is measurable, 1) the y-intercept of a regression in u_v–τ space at a given overburden will represent the contribution of F_{eff} to the observed shear stress (hereafter referred to as τ_{eff}) and 2) that this intercept should scale with increasing σ_N. This trend, however, is not obvious in our data. Table 2 lists the y-intercepts (given as τ_{eff}) calculated for linear regressions at each cryostatic stress. Though we cannot be certain of the statistical significance given the small sample sizes ($n \leq 5$), the data imply effective stress contributed meaningfully to basal drag. We also observe a weak relationship ($\tau = 0.14\sigma_N + 37$; $R^2 = 0.49$) between the applied normal load and basal drag (Fig. 7B), further indicating that effective stress influences debris-bed friction in our drained experiments. Scatter in this plot reflects the influence of basal melt rate for a given σ_N.

Table 1. Data table showing the applied normal load (σ_N), basal melt rate (u_v), mean debris-bed shear stress (τ), the sample standard deviation of the measured shear stresses (STD τ), the vertical temperature gradients in the ice (dT/dz), the standard error of the mean for τ and dT/dz (SEM τ and SEM dT/dz respectively) and the standard error of the model for u_v (SEM u_v). N/A denotes a lack of data due to equipment malfunction.

σ_N (kPa)	u_v (mm a^{-1})	SEM u_v (kPa)	τ (kPa)	STD τ (kPa)	SEM τ (kPa)	dT/dz (°C cm^{-1})	SEM dT/dz (°C cm^{-1})
294	802	0.9	65	7	0.2	N/A	N/A
294	1174	3.0	95	8	0.1	N/A	N/A
294	670	0.7	92	4	0.1	-0.21	0.0002
294	630	0.9	67	7	0.1	N/A	N/A
294	1074	3.0	104	11	0.2	-0.17	0.0003
588	1473	3.0	104	13	0.2	N/A	N/A
588	1829	2.0	138	12	0.2	-0.09	0.0002
588	1188	2.0	127	9	0.1	-0.16	0.0006
588	1315	2.0	96	9	0.1	-0.10	0.0003
588	925	2.0	76	5	0.1	-0.21	0.0006
784	2105	2.0	187	24	0.3	N/A	N/A
784	3048	2.0	201	25	0.4	-0.04	0.00009
784	1245	0.7	108	6	0.1	N/A	N/A
118	2075	2.0	53	6	0.1	0.0	0.00002
118	1061	2.0	33	4	0.1	-0.02	0.00002
118	1295	2.0	43	2	0.03	-0.03	0.00008
118	819	2.0	35	1	0.02	-0.02	0.00007

Table 2. Estimated contribution of effective stress to the observed debris-bed drag, τ_{eff}, based on the y-intercepts of linear regressions calculated for each applied normal stress σ_N in u_v–τ space. The values given for $d\tau/du_v$ are the slopes of the linear fit. We neglect associated uncertainties for these estimates due to small sample sizes ($n \leq 5$).

τ_{eff} (kPa)	σ_N (kPa)	τ_{eff}/σ_N	$d\tau/du_v$ (kPa mm^{-1} a)
20	118	0.17	0.015
43	294	0.15	0.047
34	588	0.06	0.054
56	784	0.07	0.051

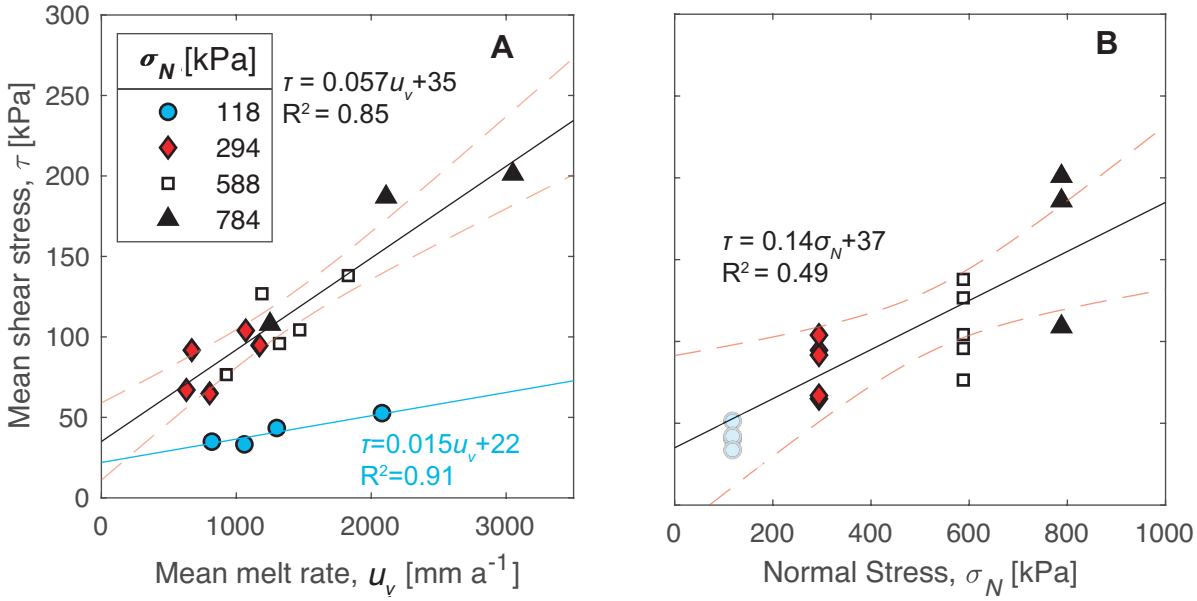

Fig. 7. A) Shear stress, τ, scales linearly with basal melt rate, u_v, but the rate of change is different between the two respective thermal regimes. B) A statistically significant correlation is observed between the applied normal stress, σ_N, and τ as well, indicating that effective stress influences basal drag in our experiments. In 7B, the σ_N = 118 kPa runs are excluded from the σ_N–τ regression, as they were conducted at different dT/dz. Standard errors for both u_v and τ are significantly smaller than the bounds of the plotted data points (Table 1) and are not included in the regression analysis.

4 DISCUSSION

To frame our experimental results against theory, we first consider the viscosity and rheology of the ice used in our experiments. These parameters exert first-order controls on the viscous drag force (Equations 3 and 4) yet represent significant sources of uncertainty in the experiments. Initial treatments of abrasion assumed ice to be a linear viscous fluid with a power law exponent n = 1 (Watts, 1974; Hallet, 1979b, 1981; Shoemaker, 1988; Iverson, 1990). However, the deformation behavior of ice is variable depending on the stress state, timescale, temperature, water content and dominant deformation mechanism (Duval, 1979; Weertman, 1983; De La

Chapelle and others, 1998; Goldsby and Kohlstedt, 2001). Therefore, it is instructive to explore how debris-bed contact forces vary with melt rate over a range of possible stress exponents (n = 1-3) and viscosity values.

Determining the creep exponent, n, and effective viscosity directly from the data is not possible due to uncertainty regarding the stress field around an abrading clast. To calculate effective viscosity, the effective shear stress acting in the immediate vicinity of a clast must be reasonably well-constrained (Iverson, 1990). However, this depends sensitively on the amount of melt produced along clast boundaries (*see* Equation A7), which is unknown in the experiments. It is not obvious if difference in basal drag observed between the two temperature regimes corresponds to a change in ice viscosity, a change in regelation rate, or both. According to classic regelation and creep theory, regelation will not occur at temperatures below PMP. However, the presence of a premelt film may allow fluid flow to influence the drag force at subfreezing temperatures.

To address this, we compare our experimental results against the predictions of three different models using a range of possible viscosity values and creep exponents (n = 1-3). First, the drag force induced by viscous creep around a slippery sphere is calculated (Lliboutry and Ritz, 1978). In this formulation, slip is assumed to occur along clast boundaries (i.e. shear stresses are not supported on the surface). This model (henceforth referred to as "L & R") serves as an analog for ice deforming around a suspended clast encased in a premelt film with negligible regelation. Treating ice as a power law fluid and neglecting regelation, the drag force F_d can be expressed

$$F_d = \alpha r^2 \frac{\eta_i}{2} \left(\frac{u_v}{r}\right)^{\frac{1}{n}} \quad (7)$$

where n is the creep exponent and α is a prefactor that varies with both n and particle geometry. (Lliboutry and Ritz, 1978; Byers and others, 2012). When n = 1, Lliboutry and Ritz (1978) give the prefactor $\alpha = 4\pi$ and for n = 3, $\alpha = 8\pi$.

Secondly, we implement the Watts/Hallet model (Watts, 1974; Hallet, 1979b, 1981) that accounts for the effects of both regelation and viscous creep on the drag force at PMP. As stated previously, this formulation (referred to as "W/H") assumes boundary conditions typical of classic regelation and creep theory. To account for nonlinear effective viscosities with the W/H, we use the extension derived by Watts (1974) and Cohen and others (2005; *see* Equations 16-20). Finally, we compare our experimental results against our modified Watts/Hallet solution (Section 1.1; Appendix) that scales the drag force to account for premelting effects at PMP. We denote this model as "PM."

For each model, we calculate how τ, exerted by twelve idealized granite spheres (r = 5 mm) against a limestone bed varies with u_v. Shear stress, τ, is calculated as

$$\tau = \mu D_c \Phi F_d \tag{8}$$

where D_c = 12 clasts per 0.01 m^2 is the areal debris concentration, μ= 0.72 is the coefficient of friction, and F_d is the drag force given by Equation 3, 5, or 7, respectively. (Note the prefactor Φ in Equation 3 is neglected since it is included in Equation 8). To calculate τ, following nominal values are used: ρ_l = 1000 kg m^{-3}, ρ_i = 917 kg m^{-3}, $\mathcal{L}$ = 3.3 x 10^5 J kg^{-1}, C = 0.074 K MPa^{-1}, K = 2.5 W m^{-1} K^{-1}. We also set the bed influence factor to Φ = 1.8 (Byers and others, 2012). For calculations involving a linear viscous rheology (n = 1), η_i = 5.9 x 10^{10} Pa s was used as a lower bound (Cohen, 2000) and 3.1 x 10^{12} Pa s was used as the upper bound (Watts, 1974; Hallet, 1979b, 1981; Shoemaker, 1988; Iverson, 1990). For nonlinear models, the viscosity values span

an order of magnitude (i.e $O(10^8$ Pa $s^{1/2})$ and $O(10^7$ Pa $s^{1/3})$ for $n = 2$ and $n = 3$, respectively), which generally encompasses the range of published values (review in Cohen, 2000).

4. 1 Model Comparisons

Figures 8 A-D compare the data collected at the colder temperature regime against the predictions of the L & R and W/H models with an assumed bed influence factor $\Phi = 1.8$. For nonlinear W/H, we consider how the form of the curve calculated for the upper and lower viscosity bounds fits the data, using the y-intercept as a free variable (Table 3). For nonlinear L & R, we find the best fit for each exponent. W/H models require a y-intercept greater than zero to fit the data, whereas the best fit nonlinear L & R curves intercept the origin. For linear viscosities, we compare how the slope of the calculated u_v–τ relationship compares to the slope of a best fit linear regression through the data: $\tau = 0.057u_v + 35$ ($R^2 = 0.85$; Table 4).

Table 3. Goodness of fit statistics for the various models. We calculate a correlation coefficient, R^2, and the root mean squared error of the residuals (RMSE) for each curve with respect to the data. Lin. Reg. St refers to the linear regression models for the steeper *dT/dz* experiments. Models designated "lower" or "upper" refer to calculations using the lower and upper viscosity bounds.

Model	*n*	R^2	RMSE
Lin. Reg. St.	1	0.85	17
W/H lower	2	0.41	32
W/H upper	2	0.83	17
W/H lower	3	0.03	41
W/H upper	3	0.79	19
L & R best fit	2	0.78	20
L & R best fit	3	0.61	26

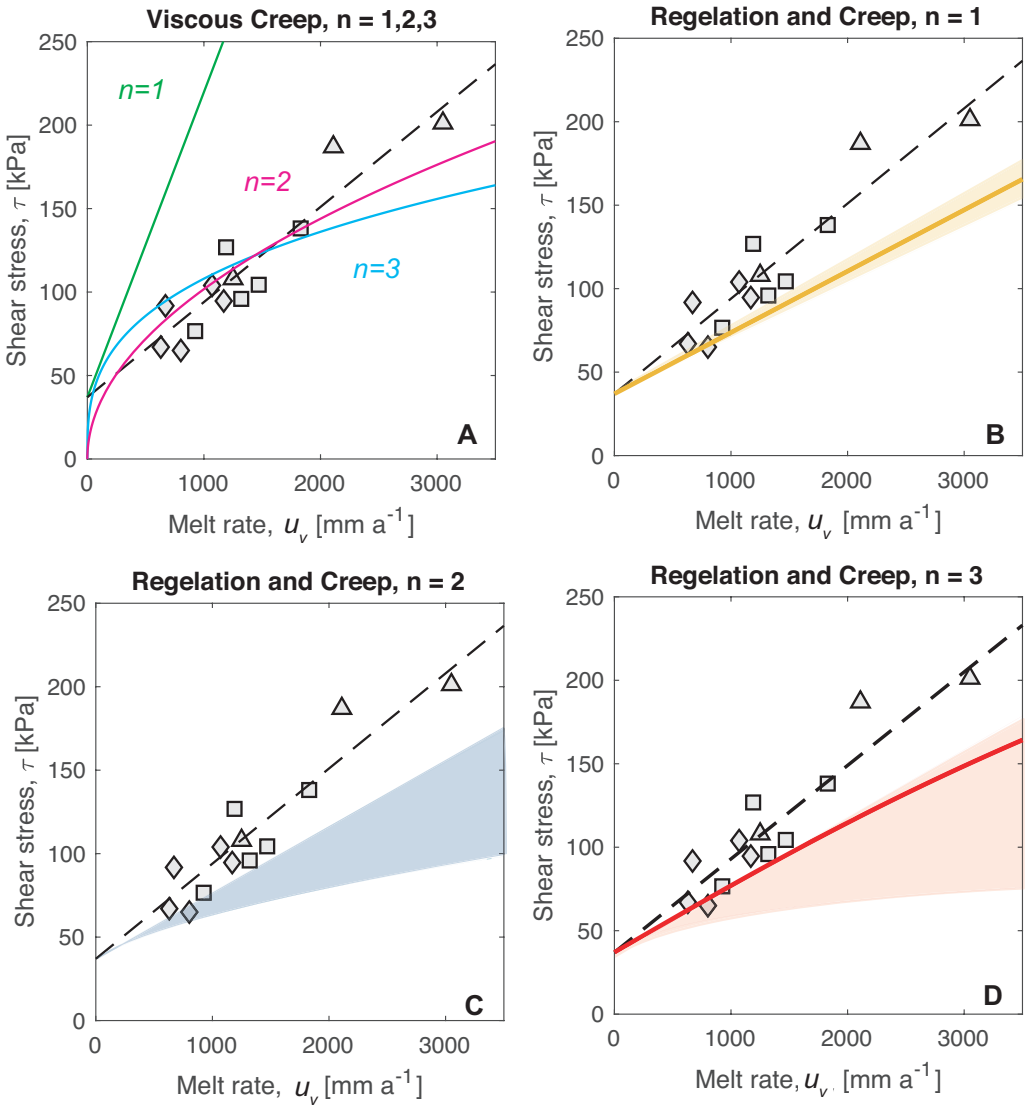

Fig. 8. A comparison of how shear stress, τ, varies with basal melt rate, u_v, in regimes dominated by viscous creep (A) or a combination of regelation and viscous creep (B-D) for different power law exponents (n = 1, 2, 3). Plot A displays best fit lines using Lliboutry and Ritz's (1978) model for viscous creep around a slippery sphere for n = 2 and n = 3, as well as a line calculated using a linear viscosity of 5.9 x 10^{10} Pa s. In B-D, shaded areas represent the range of values calculated for using the Watts/Hallet (Watts, 1974; Hallet 1979b) model and an assumed bed influence factor Φ = 1.8. Lower and upper bounds correspond to the smallest and largest viscosity values used in the calculation. In plots B and D, the darker lines represent curves calculated using preferred viscosity values published for similar experimental ice (Byers and others, 2012 for n = 1 and Zoet and Iverson, 2015 for n = 3 respectively). Black dashed lines in all plots represent a linear regression model (τ =0.057u_v + 35; R^2 = 0.85) through the larger dT/dz data (grey circles). The y-intercept is assumed to be 35 in plots B-D to compare the Watts/Hallet predictions with a best fit linear model

Estimating basal drag using nonlinear exponents (i.e. viscous creep with no regelation) (Fig 8A) produces a suboptimal fit compared to the linear model in our experiments (*see* Table 3 for goodness of fit statistics) indicating the ice in our experiments can be assumed to behave linearly. Although the magnitudes of observed τ lie within range of the possible computed outcomes for the viscous creep model, the form of the L & R curves for $n = 2$ and $n = 3$ qualitatively do not conform to the data using realistic physical parameters (Lliboutry and Ritz, 1978; Watts, 1974; Hallet, 1979b, 1981; Cohen and others, 2005). Furthermore, using the lower bound for linear viscosity (B = 5.9 x 1^{10} Pa s; Cohen, 2000), the Newtonian case is still greater than the slope of the modelled regression by a factor of ~3.2 (Fig. 8A). Pronounced misfit of the viscous model with our observations suggests the drag force is not controlled solely by viscous creep.

Table 4. Calculated slopes in u_v–τ space and the corresponding linear viscosities, η_i, used for the various models. Lin. Reg. St. and Lin. Reg. Sh. refer to the linear regression models for the steeper *dT/dz* and the shallower *dT/dz* experiments respectively. Models designated "lower" or "upper" refer to calculations using the lower and upper viscosity bounds. Slopes were calculated assuming a bed influence factor $\Phi = 1.8$.

Model	***n***	$\boldsymbol{\eta_i}$ **(Pa s)**	$\boldsymbol{d\tau/du_v}$ **(kPa mm^{-1} a)**
Lin. Reg. St.	1	N/A	0.057
Lin. Reg. Sh.	1	N/A	0.016
L & R Lower	1	5.9 x 10^{10}	0.18
L & R Upper	1	3.12 x 10^{12}	9.3
W/H Lower	1	5.9 x 10^{10}	0.033
W/H Upper	1	3.12 x 10^{12}	0.040
PM Lower	1	5.9 x 10^{10}	0.0033
PM Upper	1	3.12 x 10^{12}	0.0034

Accounting for the effects of regelation in conjunction with viscous creep improves model fits overall. A stress exponent of $n = 1$ best approximates the observed relationship between u_v and τ (*see* Table 3). For linear ice viscosities using the W/H model, a bed influence factor of $\Phi = 2.5$ - 3 was found to match the slope of the modeled regression (Fig 8B). These values closely align with Hallet's (1981) initial estimate of $\Phi = 2.4$ and prior experimental results. Furthermore, using the viscosity reported by Byers and others (2012) for Newtonian ice results in a bed influence factor of $\Phi = 2.7$ for our data. We favor this linear viscosity, as their ice was created using a similar protocol to ours and likely shared similar physical properties. However, it is important to note that the W/H model assumes fully temperate ice, whereas we observed vertical temperature gradients ($O(\text{-}10^{-2}$ °C cm^{-1})) during all experiments with available temperature data (Fig. 6), indicating a direct comparison may not be appropriate.

For higher order stress exponents (n = 2-3) in the W/H model, the form of the curve transitions from a power law with exponent less than 1 to a straight line as ice viscosity increases (Fig. 8 C-D). This shift reflects a trade-off between the two competing flow mechanisms—viscous creep and regelation—on the overall drag force, as regelation and shear stress are linearly related (Equation A7; Fig. 8 C-D). The dominance of regelation is further illustrated in our modified version of the Watts/Hallet model, which incorporates premelting effects (Fig. 9A). For the physical parameters implemented in this calculation, the rate of regelation is amplified to the point where the influence of ice rheology on the drag force is effectively negated. For all three stress exponents, n = 1-3, the u_v–τ relationship for the premelt model can be approximated as a straight line with slope of $d\tau/du_v \sim 0.0034$ kPa a mm^{-1}—at least 10 times smaller than what the original W/H model would predict (Fig. 9A).

Because the curves in the W/H and PM model converge to a straight line for nonlinear stress exponents at high viscosities, an n value cannot be confidently stated based on observed trends (Table 3; Fig. 8 and Fig. 9). However, $n = 1$ is likely a fair approximation. For example, if $n = 3$ with a viscosity of $B = 6.3 \times 10^7$ Pa $s^{1/3}$ is chosen, as Zoet and Iverson (2015) determined for similarly constructed ice, the expected u_v–τ relationship can be estimated for comparison (Fig. 8D). Using these values and fitting the result to the data collected under the larger dT/dz experiments also results in a nearly linear power law function ($\tau = 0.076u_v^{0.91} + 56$; $R^2 = 0.77$). This leads us to infer that the ice in the experiment can be represented as a linear viscous fluid, in agreement with other ice deformation and subglacial contact-force experiments (Mellor and Testa, 1969; Dahl-Jensen and Gundestrup, 1987; Duval and Castelnau, 1995; Byers and others, 2012).

On timescales and stresses comparable to our experiments, ice crystals creeping past an entrained clast are exposed to a constantly changing stress field, giving rise to a transient creep regime in which ice behaves as a Newtonian fluid (Jacka, 1984). In the context of prior abrasion/contact force experiments, Iverson (1990) observed a direct relationship between u_v–τ, and Byers and others (2012) reasoned a linearly proportional relationship between stress and strain rate for their ice. This lends credence to our interpretation that the y-intercepts of regressions through the data in u_v–τ space represent a contribution of effective stress to basal drag.

4.2 The effect of temperature gradients on debris-bed drag

The results at shallower *dT/dz* fall below the lower bound of the W/H curves and the upper bound of the PM solution (Fig. 9A). A linear u_v–τ relationship is likely for these experiments as well because they were conducted using the same ice as the colder runs, but with even lower deviatoric stresses and warmer temperatures, which would facilitate more melt along clast boundaries. Importantly, the slope of a linear regression through the data, $d\tau/du_v$ = 0.016 kPa a mm^{-1} is ~2.1 times smaller than the lower bound of the W/H model for n = 1 ($d\tau/du_v$ = 0.033 kPa mm^{-1} a) and ~4.7 times larger than the PM version ($d\tau/du_v$ = 0.0034 kPa a mm^{-1}).

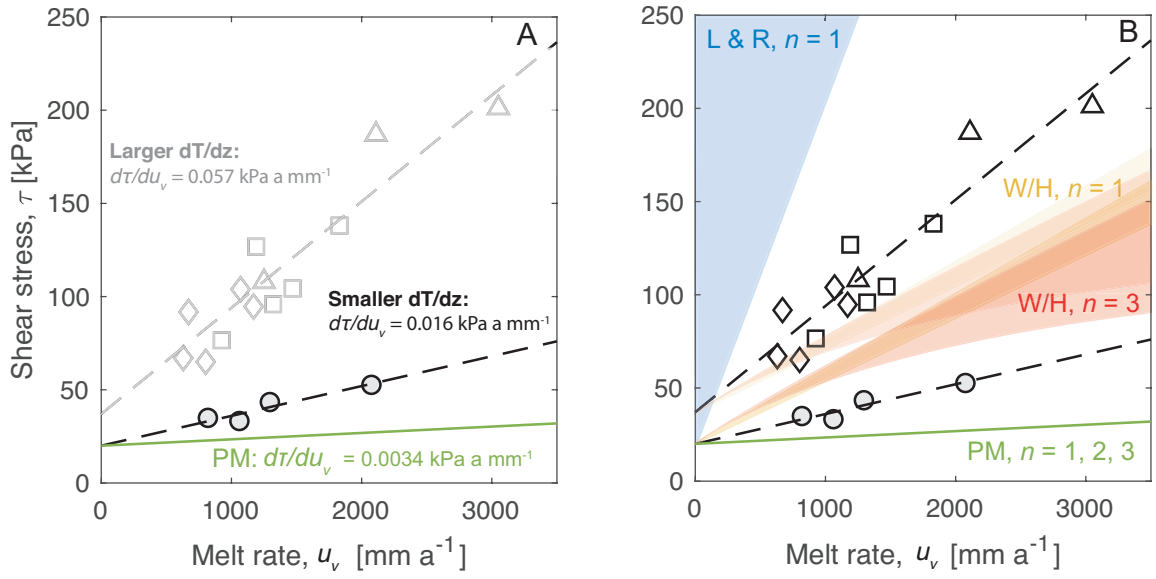

Fig. 9. Relationships between basal melt rate, u_v, and shear stress τ. Fig. 9A juxtaposes the data against the Watts solution with premelt assuming a y-intercept of 20. In 9B, the blue shaded area represents the bounds calculated for the Lliboutry and Ritz (1978) model with n = 1, using the viscosities in listed Table 4. Yellow bounds are the values calculated using the Watts/Hallet model with exponent n = 1 and red is n = 3. The green line is the modified Watts/Hallet model that accounts for premelting for all three stress exponents. Dashed lines are linear regressions through data collected at the two different *dT/dz*.

Melt along clast boundaries appears to influence basal drag in our experiments—even when ice temperatures are below PMP— since a purely viscous model overpredicts our data. We infer that the observed temperature gradients in the ice influence the u_v–τ relationship in part by changing the rate of fluid flow in the interfacial film surrounding the clast. This process likely happens in concert with temperature dependent changes in viscosity. However, current models are unable to accurately capture the complex interplay between these two mechanisms at subfreezing temperatures. Basal melting occurred when heat flow to the ice-bed interface exceeded heat flow into the ice and out the boundaries. This flux produced larger temperature gradients in the sample than would occur in a thick, fully temperate section of ice beneath a glacier, but it might simulate local deviations in temperature within basal ice. Essentially, heat transfer along the boundary of the clast—whether produced by the heating plate, frictional heating, or refreezing—was sufficient to melt ice at a rate similar to the original W/H model for the experiments conducted at larger *dT/dz*. However, at smaller *dT/dz*, the melt rate along the clast boundaries exceeded the W/H model but not PM.

Although the W/H model fits the data well to the order of magnitude, it predicts slightly larger shear stresses than what we observe for experiments near PMP. This suggests that decreasing the vertical temperature gradient in the ice may further reduce τ for a given u_v. Potentially, the u_v–τ relationship may even converge toward the premelt solution when clasts are fully encased in temperate ice. However, achieving similar melt-rates with fully temperate ice is beyond the capabilities of the experimental setup.

In the W/H and scaled PM models, the primary heat source along the clast boundary is assumed to be latent heat released when ice refreezes along zones of low pressure. However, the presence of a bed may inhibit refreezing and initiate cavity growth (Morris, 1979). Incomplete refreezing was observed to a degree in our experiments when cavities were present and in prior work (Iverson, 1990; Byers and others, 2012), but whether or not refreezing occurred in our experiments is not readily apparent. The fact that most clasts were fully encased in ice at the conclusion of each run speaks to its likelihood. However, even if refreezing is prevented in the vicinity of a clast, the process of regelation on a larger scale may still contribute meaningfully to the heat budget of entrained debris in a glacier. If debris-laden ice regelates around a bedrock obstacle, it releases heat on the lee side, which will diffuse through the bump into any abrading clasts in contact with the stoss face. Given that most abrasion is predicted to occur on the stoss side of bumps (Hallet 1981, 1996; Shoemaker, 1988), the process of regelation is likely an important source of heat for abrading clasts lodged in temperate ice.

4.3 Contribution of effective stress to debris-bed contact forces

The influence of effective stress on debris-bed contact forces relates to the presence of a lubricating film at the ice-bed interface, assumed to exist everywhere ice is in contact with the bed (Nye, 1973; Emerson and Rempel, 2007; Dash and others, 2006). If such a film exists and is hydrologically connected to the water film around the clast, a potential drainage pathway exists for melt produced along the clast's surface. Though Hallet's (1979b; 1981) model implicitly assumes that $N = 0$ in the film surrounding the clast, it does not take into account the presence of a far field lubricating film. For this theory to be consistent, the pressure in both films must equal the cryostatic stress and remain constant in space and time. This assumption holds when the

transmissivity at the bed is zero or if the ice/clast film is completely isolated from the far field water film. However, in drained conditions, such as our experiments, this assumption is likely not appropriate.

Although hydraulically isolated regions are common along glacial beds (Nye, 1973b; Hallet, 1979a; Fountain, 1994, Engelhardt and Kamb, 1997; Andrews and others, 2014), fluctuating basal water pressure is routinely observed at hard-bedded glaciers (Fountain, 1994; Hubbard and others, 1995; Sugiyama and Gudmundsson, 2004). For example, Fountain (1994) observed that while water pressures in approximately 50% of the boreholes drilled at South Cascade glacier were at floatation, a subset was near atmospheric pressure in the vicinity of a conduit. If the hydraulic transmissivity of the bed is greater than zero, as we designed it to be in our experiments, the magnitude of effective stress around the clast will then be controlled by 1) fluid potential in the far field film, 2) the vertical stress components driving flow around the clast (i.e. N, F_d, and F_b), 3) the relative thickness of the two films (Emerson and Rempel, 2007), and 4) the geometry of the clast.

The component of drag we attribute to effective stress in our experiments ranges from ~6%- 17% of the overburden (Table 2). For comparison, we calculate the expected drag due to effective stress, τ_{eff}, using Boulton's (1974) theory for 12 idealized spheres (Equation 1). (We neglect the viscous drag here to focus on τ_{eff}.) Shear stress is given

$$\tau_{eff} = \mu D_c F_{eff} , \tag{9}$$

where D_c = 12 clasts per 0.01 m^2 is the areal debris concentration, and μ= 0.72 is the coefficient of friction determined empirically for granite against limestone. Even when considering an unrealistic, end-member scenario that has thick far field film (t = 1 mm) and negligible water

pressure ($P_l = 0$), the maximum expected shear stress is ~2.4%; for a more realistic film thicknesses on the order of microns, the expected drag is less than 1%. The shear stresses predicted by Boulton's theory are much smaller than we observe.

We propose two possible explanations for this discrepancy: 1) non-idealized clast geometry and 2) an uneven distribution of normal stress at the ice-bed interface. For a spherical particle, cryostatic stress is distributed uniformly across its surface due to symmetry, with vertical stresses balanced above and below the clast. A more angular or blocky clast, however, may have a greater contact area with the bed, and vertical stresses applied to the top surface will outweigh opposing, upward-facing stresses, leading to higher contact forces. Given that single clasts in our experiments commonly left multiple striations, this scenario is feasible (Fig. 3C, 3D, 3E). In the context of the subglacial environment, it implies that 1) blocky clasts in transport along drained areas of a glacier's bed can impart significant force to the bed, and 2) the capacity for debris to impart force to the bed will decrease as it gets rounded in transport.

Another mechanism that could potentially increase the contribution of effective stress is an uneven distribution of normal stress at the ice-bed interface. Boulton's model (1974) assumes that pressure is evenly distributed across the bed due to the presence of the water film and that fluid pressure in that film bears a large portion of the normal load. If the thickness of this film was smaller than the dominant roughness elements along the bed's surface, stress would be transferred to the ice-on-rock contacts and the abrading clasts, which would act as isolated asperities (Zoet and Iverson, 2018). Decreasing the real area of contact corresponds to an increase in the normal force exerted on each clast to maintain the same shear stress, resulting in greater contact forces than Boulton's model predicts.

5 CONCLUSION

We conducted drained laboratory abrasion experiments to investigate the relative influence of basal melt rate and effective stress on subglacial rock friction in two thermal regimes. Basal shear stress scales linearly with both melt rate at the ice-bed interface and applied normal stress, and slight depressions in ice temperature increase the contribution of bed-normal viscous drag. We estimate the contribution of effective stress to basal drag to be between ~6%-17% of the overburden in our experiments, larger than predicted by Boulton's (1974) model for subglacial abrasion. These results suggest effective stress may be a dominant control on debris-bed contact forces in drained conditions for temperate ice, in contrast to the common assumption that it is negligible.

Comparing the observed relationships between melt rate and drag to the predictions of three friction models, we find the data are best described by a model that accounts for the effects of viscous creep and regelation on the bed-normal drag force. Observed shear stresses are lower than expected if viscous creep alone set the drag force, and the Watts/Hallet model (Watts 1974; Hallet, 1979b, 1981) provides the best fit to our data overall, even for experiments conducted at temperatures below the pressure melting point. We interpret this to mean that melt along clast boundaries influenced the contact force even at subfreezing temperatures due to the presence of an interfacial film. Incorporating premelting dynamics into the Watts/Hallet model (W/H) for debris-bed friction predicts a nearly an order-of-magnitude decrease in shear stress and a corresponding ~3.5x increase in the transition radius with respect to the original model. This model underpredicts our data by at least a factor of ~4, but it may provide a better fit for fully temperate ice.

ACKNOWLEDGEMENTS

The authors thank the reviewers for their enlightening comments and the following people for their valuable insight and conversation: N. Lord, P. Sobol, C. Meyer, N. Iverson, N. Stevens, J. Woodard, and K. Feigl. N. Lord and P. Sobol were instrumental in the success of this project, constructing key pieces of our experimental setup and providing invaluable technical support and advice. E. Parrish provided the photograph of the clast. D. D. Hansen was supported by funding from Wisconsin Alumni Research Association awarded to L. K. Zoet.

REFERENCES

Anderson RS (2014) Evolution of lumpy glacial landscapes. *Geology* 42(8), 679–682

Andrews LC and 7 others (2014). Direct observations of evolving subglacial drainage beneath the Greenland Ice Sheet. *Nature*, 514(7520), 80–83

Baltrūnas V, Šinkūnas P, Karmaza B, Česnulevičius A, and Činkūnė E (2009) The sedimentology of debris within basal ice, the source of material for the formation of lodgement till: an example from the Russell Glacier, West Greenland. *Geologija*.

Beaud F, Flowers GE and Pimentel S (2014). Seasonal-scale abrasion and quarrying patterns from a two-dimensional ice-flow model coupled to distributed and channelized subglacial drainage. *Geomorphology* 219, 176–191.

Boulton GS (1974) Processes and pattern of glacial erosion. In *Glacial geomorphology*, p. 41-87.

Byers, J, Cohen D, and Iverson NR (2012), Subglacial clast/bed contact forces, *J. Glaciol.,* 58(207), 89–98

Cohen D, Iverson N, Hooyer T, Fischer U, Jackson M and Moore P (2005) Debris–bed friction of hard-bedded glaciers. *J. Geophys.Res*., 110(F2), F02007

Dash JG, Fu H and Wettlaufer JS (1995). The premelting of ice and its environmental consequences. *Rep. Prog. Phys.*, 58(1), 115

Dash JG, Rempel AW and Wettlaufer JS (2006) The physics of premelted ice and its geophysical consequences. *Rev. Mod. Phys.*, 78(3), 695–741

De La Chapelle S, Castelnau O, Lipenkov V, and Duval P (1998) Dynamic recrystallization and texture development in ice as revealed by the study of deep ice cores in Antarctica and Greenland. *J. Geophys Res. Solid Earth*, 103(B3), 5091-510

Drewry D. (1986) *Glacial geologic processes*. London, Edward Arnold.

Duval P (1979) Creep and recrystallization of polycrystalline ice. *Bull. Mineral. 102*(2), 80-85

Egholm DL and 7 others (2017) Formation of plateau landscapes on glaciated continental margins. *Nat. Geosci.*, 10, 592–597

Emerson LF and Rempel AW (2007) Thresholds in the sliding resistance of simulated basal ice. *Cryosphere*, 1(1), 11–19

Engelhardt H. and Kamb B, 1997. Basal hydraulic system of a West Antarctic ice stream: constraints from borehole observations. *J. Glaciol.*, 43(144), 207-230

Fountain AG (1994) Borehole water-level variations and implications for the subglacial hydraulics of South Cascade Glacier, Washington State, USA. *J. Glaciol.*, 40(135), .293-304

Gilpin RR (1979) A model of the "liquid-like" layer between ice and a substrate with applications to wire regelation and particle migration. *J. Colloid Interface Sci.*, 68(2), 235-251

Goldsby DL and Kohlstedt DL (2001) Superplastic deformation of ice: Experimental observations. *J. Geophys Res. Solid Earth*, 106(B6), 11017-11030

Goren SL (1970) The normal force exerted by creeping flow on a small sphere touching a plane. *J. Fluid Mech.*, 41(3), 619–625

Gudmundsson GH (1997) Basal-flow characteristics of a non-linear flow sliding frictionless over strongly undulating bedrock. *J. Glaciol.*, 43(143), 80–89

Haldorsen S (1981) Grain-size distribution of subglacial till and its relation to glacial crushing and abrasion. *Boreas*, 10(1), pp.91-105

Hallet B. (1979a) Subglacial regelation water film. *J. Glaciol.*, 23(89), 321-334

Hallet B (1979b) A theoretical model of glacial abrasion. *J. Glaciol.*, 23(89), 39–50

Hallet B (1981) Glacial abrasion and sliding: their dependence on the debris concentration in basal ice. *Ann. Glaciol.*, 2, 23–28

Hallet B, Hunter L and Bogen J (1996) Rates of erosion and sediment evacuation by glaciers: A review of field data and their implications. *Global Planet. Change*, 12(1-4), 213-235

Herman F, Beaud F, Champagnac JD, Lemieux JM and Sternai P (2011) Glacial hydrology and erosion patterns: a mechanism for carving glacial valleys. *Earth Planet. Sci. Lett.*, 310(3-4), 498-508

Herman F and eight others (2015) Erosion by an Alpine glacier. *Science*, 350(6257), 193-195

Hindmarsh RCA (1996) Cavities and the effective pressure between abrading clasts and the bedrock. *Ann. Glaciol.*, 22, 32–40

Hoffman MJ and nine others (2016) Greenland subglacial drainage evolution regulated by weakly connected regions of the bed. *Nat Commun.*, 7, 13903

Hubbard B and Sharp M (1995) Basal ice fades and their formation in the western Alps. Arct. *Antarct. Alp. Res.*, 27(4) 301-310

Iken A (1981) The effect of the subglacial water pressure on the sliding velocity of a glacier in an idealized numerical model. *J. Glaciol.*, 27(97), 407–421

Iverson NR (1990) Laboratory simulations of glacial abrasion: comparison with theory. *J. Glaciol.*, 36(124), 304–314

Iverson NR and 6 others (2003) Effects of basal debris on glacier flow. *Science*, 301(5629), 81–84

Kamb B (1970) Sliding motion of glaciers: theory and observation. *Rev. Geophys.*, 8(4), 673–728

Kirkbride, M. (2002), 6 – Processes of glacial transportation, in Modern and Past Glacial Environments, pp. 1–24, Butterworth-Heinemann, Woburn, MA.

Koppes M. and Hallet B (2006) Erosion rates during rapid deglaciation in Icy Bay, Alaska. J. *Geophys Res. Earth Surf.*, 111(F2)

Koppes M, Hallet B, Rignot E, Mouginot J, Wellner JS and Boldt K (2015) Observed latitudinal variations in erosion as a function of glacier dynamics. *Nature*, 526(7571), 100

Lee AGG and Rutter EH (2004) Experimental rock-on-rock frictional wear: Application to subglacial abrasion. *J. Geophys Res. Solid Earth*, 109(B9)

Lliboutry L (1968) General theory of subglacial cavitation and sliding of temperate glaciers. *J. Glaciol.*, 7(49), 21-58

Lipovsky BP and 5 others (2019) Glacier sliding, seismicity, and sediment entrainment. *Ann. Glaciol.* (doi: 10.1017/aog.2019.24)

McCarthy C, Savage H and Nettles M (2017) Temperature dependence of ice-on-rock friction at realistic glacier conditions. *Phil. Trans. R. Soc. A*, 375(2086), 20150348

Morris EM (1979) The flow of ice, treated as a Newtonian viscous liquid, around a cylindrical obstacle near the bed of a glacier. *J. Glaciol.*, 23(89), 117-129

Nye JF (1969) A calculation on the sliding of ice over a wavy surface using a Newtonian viscous approximation. *Proc. R. Soc. Lond. A*, 311(1506), 445–467

Nye JF (1970) Glacier sliding without cavitation in a linear viscous approximation. *Proc. R. Soc. London, Ser. A*, 315(1522), 381–403 (doi: 10.1098/rspa.1970.0050)

Nye JF (1973) Water at the bed of a glacier, in *Symposium on the Hydrology of Glaciers*, *IAHS Publ.*, 95, 189-194

Rempel AW and Worster MG (1999), The interaction between a particle and an advancing solidification front, *J. Cryst. Growth*, 205(3), 427– 440

Rempel AW, Wettlaufer J and Worster MG (2001) Interfacial premelting and the thermomolecular force: thermodynamic buoyancy. *Phys. Rev. Lett.*, 87(8), 088501

Rempel AW, Wettlaufer J and Worster MG (2004) Premelting dynamics in a continuum model of frost heave. *J. Fluid. Mech.*, 498, 227–244

Rempel AW and CR Meyer (2019) Premelting icreases the rate of regelation by an order of magnitude. *J. Glaciol.,* 65(251) 518–521

Shoemaker EM (1988) On the formulation of the basal debris drag for the case of sparse debris. *J. Glaciol.*, 34(118), 259–264

Schweizer J and Iken A (1992) The role of bed separation and friction in sliding over an undeformable bed. *J. Glaciol., 38*(128), 77-92

Sugiyama S and Gudmundsson GH (2004) Short-term variations in glacier flow controlled by subglacial water pressure at Lauteraargletscher, Bernese Alps, Switzerland. *J. Glaciol.*, 50(170, 353-362

Ugelvig SV and Egholm DL (2018) The influence of basal-ice debris on patterns and rates of glacial erosion. *Earth Planet Sci. Lett.*, 490, 110-121

Watts, PA (1974) Inclusion in ice. (PhD thesis, University of Bristol)

Weertman J (1983) Creep deformation of ice. *Annu. Rev. Earth Planet. Sci.*, 11(1), 215-240

Zoet L and 6 others (2013) The effects of entrained debris on the basal sliding stability of a glacier. *J. Geophys. Res.: Earth Surf.*, 118(2), 656–666

Zoet LK and Iverson NR (2015) Experimental determination of a double-valued drag relationship for glacier sliding. *J. Glac.*, 61(225), 1–7

Zoet LK and Iverson NR (2016) Rate-weakening drag during glacier sliding. *J. Geophys. Res.: Earth Surf*., 121(7), 1206–1217

APPENDIX

Premelting effects on debris-bed contact forces

Closely following the rationale outlined in Rempel and Meyer (2019), we incorporate the same premelting condition into Watts' (1974) original analysis of temperate ice moving past a sphere through a combination of regelation and viscous creep. For brevity's sake, we touch on the major points of their argument and refer the reader to Equations 1-9 in Rempel and Meyer (2019) for an in-depth discussion of their justifications. Equations from Rempel and Meyer (2019) are referenced with "RM" preceding the number; equations from Watts are preceded by "W."

Watts (1974) considers the case of a spherical inclusion forced through an infinite body of temperate ice, in which motion is accommodated through a combination of regelation and viscous creep. A thin film of water surrounds the clast, and the temperature at the ice-liquid interface is approximated as

$$\Delta T = \rho_i \mathcal{L} K^{-1} r v_r \tag{A1}$$

where $\Delta T = T_m - T$, T_m is the bulk melting temperature at ambient pressure, T is the temperature at the ice-liquid interface, $\rho_i \mathcal{L}$ is the volumetric latent heat of fusion for ice, K is the mean thermal conductivity of ice and rock, r is the radius of the sphere, and v_r is the regelation rate (*see* W15-16). Normal stresses imparted against the clast through the water film are assumed to covary with temperature (*see* W16), such that

$$\Delta T = -C \Delta \sigma_{rr} \tag{A2}$$

where C is the Clapeyron slope, and $\Delta\sigma_{rr}$ is the corresponding change in radial stress in polar coordinates relative to ambient hydrostatic pressure, σ_{amb} or P_{amb} (i.e. $\Delta\sigma_{rr} = \sigma_{rr} - \sigma_{amb}$). Though Watts (1974) expresses the radial stress in polar coordinates, Cauchy's law shows that $\Delta\sigma_{rr}$ is

equivalent to the change in water pressure in the film, $\Delta P_l = P_l - P_{amb}$, which is assumed to equal the stresses imparted by the ice, $\Delta P_i = P_i - P_{amb}$. Therefore, by eliminating ΔT from equating Equations 6 and 7, we obtain an expression for v_r in terms of the pressure gradient in the film (*see* W17), whereupon

$$v_r = -\frac{KC\Delta P_l}{\rho_i \mathcal{L} r}. \tag{A3}$$

Water movement through the thin film surrounding the clast can be approximated as Poiseuille flow between two parallel plates. Likewise, conservation of mass dictates that the pressure gradient driving fluid flow through the film is a function of the regelation rate (*see* RM5), expressed as

$$\Delta P_l = \frac{12\rho_i \eta_w v_r r}{\rho_l \delta^2} \tag{A4}$$

where δ is the thickness of the film surrounding the clast, and η_w is the viscosity of liquid water. Combining Equation A3 with Equation A4 and solving for δ using textbook values for the various physical constants (*see* RM5-RM6 in Rempel and Meyer (2019) and parameter values listed therein) implies a film thickness of ~3.1 nm for the case where $\Delta P_i = \Delta P_l$. This result essentially forms the crux of Rempel and Meyer's (2019) argument: 1) A nm-scale film thickness is unlikely to occur in nature; 2) on that scale, premelting dynamics enable significant changes in effective stress within the film (i.e. $\Delta N \neq 0$); 3) therefore, regelation by pressure melting alone is unlikely for the case of water flowing through a thin film bounded by impermeable solids. Instead, it is necessary to invoke the generalized Clapeyron equation to describe temperature changes with respect to both ΔP_l and ΔN (Rempel, 2008; RM7 in Rempel and Meyer 2019), in which

$$\Delta T \approx -C\left(\Delta P_l + \frac{\rho_l}{\rho_l - \rho_i}\Delta N\right). \quad \text{(A5)}$$

and $\Delta N = \Delta P_i - \Delta P_l$.

Substituting the expression for ΔT in Equation A5 into Equation A1 and considering the typical case where $\Delta P_i >> \Delta P_l$ (*see* RM8 and RM9) leads to

$$v_r \approx \frac{\rho_l}{\rho_l - \rho_i}\frac{KC\Delta P_i}{\rho_i \mathcal{L} r}. \quad \text{(A6)}$$

This expression for the regelation rate replaces W5 in Watts's (1974) analysis. Watts gives the radial pressure imparted by the ice through the film (*see* W18) as

$$\Delta P_i = \frac{3\eta_i(u_v cos\theta - v_r)}{r}, \quad \text{(A7)}$$

where η_i is the viscosity of ice.

Following Watts's (1974) steps, we substitute the right side of Equation A7 into Equation A6 and solve for v_r to find

$$v_r = \frac{\rho_l}{\rho_l - \rho_i} \cdot \frac{3\eta_i C u_v cos\theta}{\rho_i \mathcal{L} K^{-1} r^2 + \frac{\rho_l}{\rho_l - \rho_i} 3\eta_i C}. \quad \text{(A8)}$$

Finally, by replacing v_r in Equation A7 with the equivalent expression in Equation A8 and then integrating across the sphere's surface, we obtain the drag force, F_d, imparted against the sphere, given as

$$F_d = 2\pi r^2 \int_0^\pi \Delta P_i \, cos\theta sin\theta d\theta = \frac{4\pi\eta_i u_v r^3}{r_*^2 + r^2}, \quad \text{(A9)}$$

where

$$r_* = \left(\frac{\rho_l}{\rho_l - \rho_i}\frac{3\eta_i CK}{\rho_i \mathcal{L}}\right)^{\frac{1}{2}}. \quad \text{(A10)}$$

Notably, we find that r_* is approximately $\sqrt{\rho_l/(\rho_l - \rho_i)} \approx 3.5$ times larger than the transition radius predicted by Watts's (1974) original analysis.

Chapter 3. Subglacial abrasion rates scale with rock-frictional energy during basal slip

DD Hansen[1], J Brooks[1], LK Zoet[1,2], NT Stevens[1], L Smith[1], C Bate[2], B Jahnke[2]

[1]*Department of Geoscience, University of Wisconsin-Madison, 1215 W. Dayton St., Madison, Wi, 53715*

[2]*Department of Geological Engineering, University of Wisconsin-Madison, 1415 Engineering Dr., Madison, Wi, 53706*

ABSTRACT

Subglacial abrasion drives erosion for many glaciers, inundating forefields and proglacial marine environments with glaciogenic sediments. Theoretical treatments of this process suggest that bedrock abrasion rates scale linearly with the energy expended through rock-on-rock friction during slip, but this assumption lacks a physical basis for general implementation. To test this approach, we simulated abrasion by sliding debris-laden temperate ice over rock beds under subglacial conditions in two experimental devices. Miniscule volumes of erosion that occurred during each run were mapped with a white-light profilometer, and we measured other variables needed to constrain the energy expenditure. From these data, we infer the relationship between abrasion rates, the work done during slip, and the energy dissipated through abrasion. We find that average shear force at the bed increases linearly with abraded volume per unit area and that abrasion rates increase linearly with basal power for planar beds. This confirms that landscape evolution models can parameterize abrasion rates based on basal power, rather than common

formulations using sliding speed. Lastly, a small percentage (<1 %) of the energy partitioned to basal slip is dissipated by abrasion.

1 INTRODUCTION

Glaciers and ice sheets erode bedrock at rates faster than most natural systems (Hallet 1996). Throughout the Quaternary to present, glaciers have sculpted the morphology of mid- to high-latitudes, exposing their iconic bedforms as they recede (Benn and Evans, 2009). This persistent denudation modulates earth's climate through a series of feedbacks linking climate, tectonics, and erosion (Molnar and England, 1990; Raymo and Ruddiman, 1992), and some suggest it created the enigmatic concentration of geologic unconformities below Cambrian strata, collectively known as the Great Unconformity (White, 1972; Keller et al., 2018). Nevertheless, simulating glacial erosion using physically motivated erosion laws in landscape evolution models (LEMs) is challenging due to the difficulty of constraining its phenomenological controls.

Fundamentally, glacial erosion arises from the gravitationally driven motion of ice, which is set by the distribution of ice mass and underlying catchment topography (Andrews, 1972). As glaciers move from high to low elevations, stored potential energy dissipates at first order through the internal deformation of ice (Nye, 1957), the melting of snow and ice (Nye, 1976), and basal slip (Weertman, 1957). Energy partitioned to basal slip facilitates the mechanical wear of bedrock through the combined actions of abrasion (when ice-embedded rock fragments gouge underlying rock) and quarrying (when blocks are removed along cracks) (Drewry, 1986). Thus,

the total power available to erode the substrate is some fraction of the work done by ice slipping over rock (W_b) per unit time per unit area sometimes termed "basal power,"

$$\dot{W}_b \equiv \frac{dW_b}{dt} = u_s \tau_b, \quad (1)$$

where u_s is slip speed of ice, t is time, and τ_b is basal shear stress (Hallet, 2011). Expressed differently, the energy dissipated through abrasion and quarrying limits the finite amount of energy available for the physical processes that facilitate slip (regelation and viscous deformation), though the extent of energy dissipation is largely unconstrained.

Previous estimates suggest that ~30–40% of $\dot{W}_b$ is dissipated through subglacial abrasion (e.g. Metcalf, 1979), which would have considerable ramifications for slip dynamics. However, these studies are based on field data with large uncertainties, and their results seemingly contradict modern observations of energy partitioning in active faults, which often report on the order of ~1% (Fulton and Rathbun, 2011, and references therein). Given the physics governing rock-on-rock friction at the ice-bed interface are identical to a typical fault system (Zoet et al., 2013a), one might expect these energy expenditures to fall within the same order of magnitude.

Currently the relationship between abrasion rates and basal power is tenuous and therefore so is the proper form of the abrasion law. A link between these two variables is implicitly reflected in Hallet's (1979) widely used model for glacial abrasion. He proposed a simple wear law of the form:

$$\dot{A} = \alpha C {F_n}^l u_p, \quad (2)$$

where $\dot{A}$ is the fractional areal abrasion rate, α represents the erodibility of the rock and relates to clast angularity and the hardness contrast with the bed, C is the areal concentration of debris, l is an empirical constant typically assumed to be unity, u_p is the particle velocity, and F_n is the

average bed-normal contact force between clasts and the bed (Bolton, 1974; Hallet, 1979). Assuming Coulomb friction, the drag, τ_r, arising from subglacial rock friction equals μF_n, implying that $\dot{A}$ scales with the work expended through rock frictional energy per unit time, $\mu F_n u_s$ (Hallet, 2011). From this follows a simple abrasion rule that can be implemented in LEMs:

$$\dot{A} = KC\tau_r u_s, \quad (3)$$

where K is an erodibility constant. A clear benefit of this basal power approach is that it does not assume specific controls on F_n, which are often uncertain and can deviate from Hallet's (1979, 1981) conceptual model (Hansen and Zoet 2019; Thompson et al., 2020). Linearity between $\dot{W}_b$ and $\dot{A}$, as implemented in LEMs (Hallet, 2011; Ugelvig and Egholm, 2018), assumes a linear relationship between τ_r and τ_b. Paired with a quarrying rule in LEM runs, Eq. 3 has produced realistic and spatially heterogeneous erosion rates characteristic of natural systems (Ugelvig and Egholm, 2018), but the empirical basis for its use remains unverified. This uncertainty stems in part from difficulty in measuring $\dot{A}$ in the field given the myriad complicating factors and the difficulty in measuring abrasion in the laboratory due to the complexity of replicating in-situ conditions and the miniscule amounts of erosion that occur over the short duration (days–weeks) of these experiments.

In this study, we use a novel cryogenic ring-shear device to create the most realistic laboratory simulations of glacial abrasion to date and a high-precision profilometer to measure erosion that occurred during basal slip. With this data, we examine the relationships between abrasion, the work done during slip, and the energy dissipated through striating rock to assess the viability of the basal power approach to modeling abrasion.

2 METHODS

To quantify the relationship between rock frictional energy and $\dot{A}$, we used a cryogenic ring shear device (hereafter RS) (Hansen and Zoet, 2022) and an ELE International direct shear with a custom sample chamber (DS) to slide temperate ice laden with granitoid clasts over beds of marble and limestone following previously published methods (see Supplemental S1–S2 for further details). We prescribed a range of sliding velocities, normal stresses, debris concentrations, and basal melt rates (Table 1)—known controls on debris-bed friction and $\dot{A}$ (Thompson et al., 2020, references therein). For the limestone-bed experiments, twelve very angular, granitic rock fragments with high sphericity were encased in ice at roughly equidistant spacing in contact with the bed. Both the angularity of these clasts and their hardness contrast (relative to the soft limestone) are greater than most glacier settings and therefore serve as an end member case. For the marble runs, we sourced subangular–subrounded granitic clasts from subglacial till. We intentionally selected hard clasts to minimize comminution and isolate the effects of abrasion. Striations were scanned with a JR25 Nanovea white-light interferometer (resolution: 10 μm by 10 μm at 31 nm wavelength) to create digital elevation models (DEMs) of the abraded surface. From these DEMs, we calculated total eroded volume, V, by fitting a plane to the surface and quantifying the volume enclosed between the abraded surface and this plane (workflow described in S3).

The energy consumed through abrasion is defined as

$$E_A = \gamma \Delta S, \quad (4)$$

where γ is the specific surface fracture energy of the rock, and ΔS is the difference between the initial surface area of the bed and the surface area post-shear (Fulton and Rathbun, 2011). We

derived γ for both lithologies from measurements of fracture toughness obtained with cracked-chevron, notched Brazilian disc tests (CCNBD), as well as Young's modulus, E, and Poisson's ratio, v, measured in uniaxial unconfined compression tests, (UCT) (see S5 for derivation, methods, and CCNBD/UCT results).

The change in surface area following abrasion is defined as

$$\Delta S = S_{\mathrm{surf}} - S_{proj} + S_{\mathrm{p}}, \quad (5)$$

where S_{surf} is the surface area of the void contained within the striation, S_{proj} is the projected area of the striation, and S_{p} is the surface area of the gouge particles. S_{p} is defined

$$S_{\mathrm{p}} = R \sum_i \frac{6}{d_i} \partial V_{\mathrm{i}} V, \quad (6)$$

where d and ∂V are the grain diameter and fractional volume respectively for a given size fraction i, and R is a roughness factor correcting for the deviation of particle surface area from a sphere, which we set to be 4 ± 1 in line with previous work (Fulton and Rathbun, 2011). We do not include $S_{\mathrm{surf}} - S_{\mathrm{proj}}$ in our calculations as it was >2 orders of magnitude smaller than S_{p}. To constrain d_i, we slid clasts encased in epoxy slabs over both rock types and measured the grain-size distribution of the resulting gouge using laser diffraction analysis (S4).

We employ a simple Monte Carlo Markov Chain error propagation scheme to estimate the posterior distribution of E_{a}, using Eq. 4–6 and Eq. S1–S4 for 20,000 randomly perturbed simulations (see S6, Stevens et al. 2022). We characterize linear trends by computing the regression coefficients and their associated standard error with an ordinary or weighted least-squares solution.

3 RESULTS

The striations produced in these experiments spanned the range of common forms in nature (Fig. 1) but often shallowed with increasing displacement in RS runs (Iverson, 1991). Both RS experiments began with approximately the same number of clasts in contact with the bed, but the total number of striations created during shear varied between the two experiments (Table 1). Numerous clasts stopped abrading the bed before ice ring rotation ceased in both experiments, though average striation length in RS1 was a smaller fraction of the total displacement than RS2. For DS experiments, indenting clasts generally ploughed for the full displacement (~1 cm).

Boundary conditions implemented in these experiments are purposefully diverse (Table 1), yet when normalized by bed area, measured shear force (F_s) scales linearly with abraded volume (V) for the same clast/bed combinations (~0.35 and ~1.53 kN/μm)—implying a simple intrinsic relationship between the two parameters. Contextualizing this with Eq. 3 using parameters in Table 1 (assuming C is best represented by n_{stria}/A), $\dot{A}$ increases linearly with $C\tau_r u_s$ with erodibility constants for the limestone/granite and marble/granite runs, $K_{ls} \sim (1.6 \times 10^{-10}) \pm 1.7 \times 10^{-11}$ Pa^{-1} and $K_m \sim (5.8 \times 10^{-12}) \pm 7.4 \times 10^{-13}$ Pa^{-1} respectively. Notably, these values are >10x smaller than prior estimates (Ugelvig and Egholm, 2018)

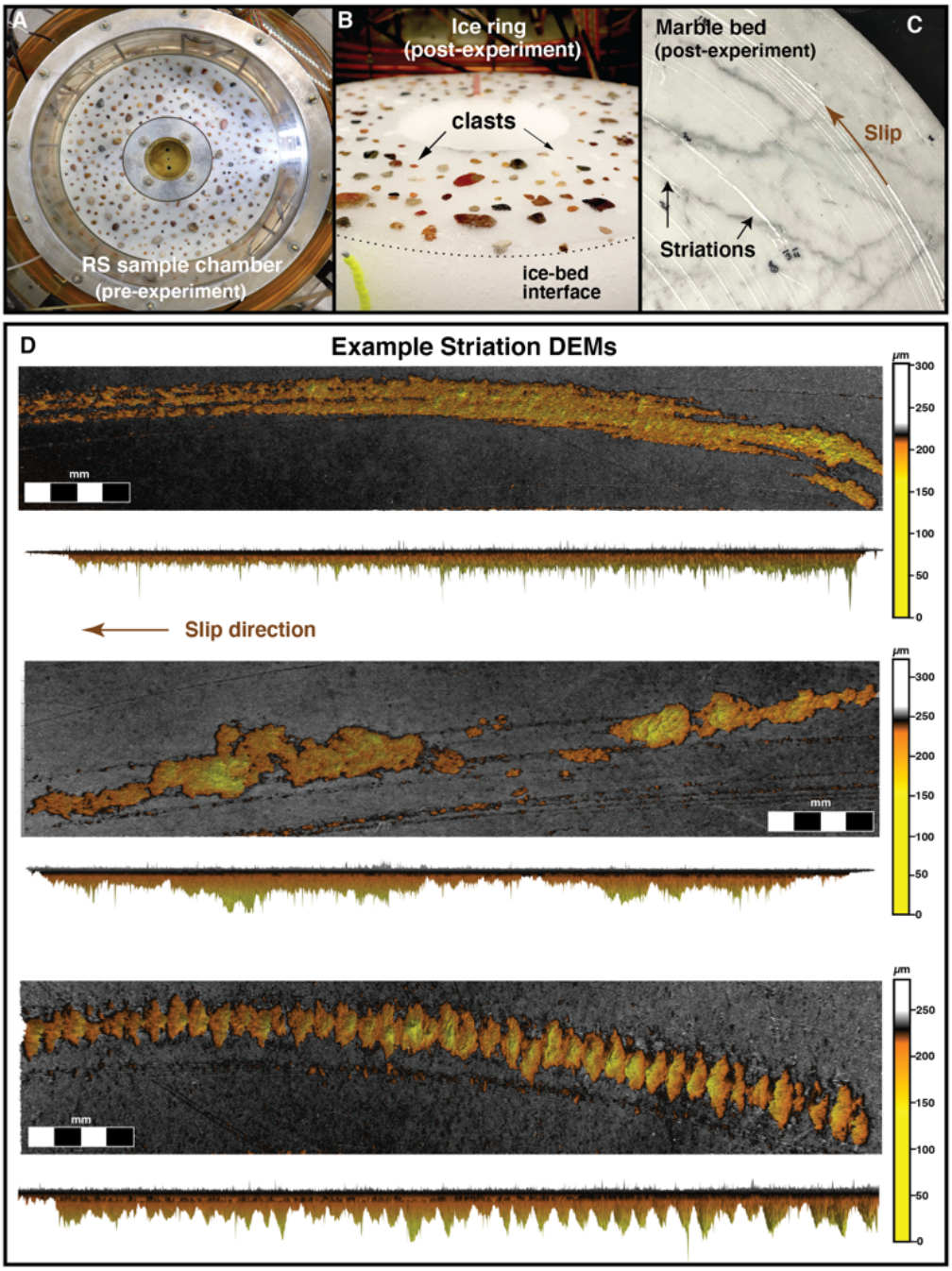

Figure 1. A) Ring shear sample chamber with bed and clasts (no-ice), B) ice ring with entrained clasts, C) striations left on marble bed, D) three example striation DEMs in plan-view and cross-section

Table 1. Run parameters and results†

Exp. Device	Bed Type	A [cm^2]	σ_n [kPa]	τ_r [kPa]	u_s [m/yr]	u_v [mm/yr]	*Disp* [cm]	n_{clast}	n_{stria}	V [mm^3]
RS	M	2513.3	301	1.7	37.5	560	81.04	311	159	78.9
RS	M	2513.3	302	4.2	37.5	780	71.26	311	291	178.7
DS	M	100	200	24.4	200	1460	0.99	50	77	2.45
DS	M	100	200	14.7	200	2086	0.87	50	50	1.65
DS	M	100	200	74.1	200	2094	0.12	100	114	5.85
DS	M	100	200	74.6	200	1600	0.92	100	150	4.47
DS	M	100	200	53.7	200	1749	0.11	200	94	2.85
DS	LS	100	294	13.4	526	944	0.995	12	17	14.6
DS	LS	100	294	45.6	526	750	0.880	12	12	12.2
DS	LS	100	294	93.5	526	50	0.972	12	17	3.93
DS	LS	100	588	138.6	526	1370	0.943	12	15	21.9
DS	LS	100	588	83.8	526	1210	1.102	12	14	37.8
DS	LS	100	588	68.1	526	1270	0.926	12	19	25.7
DS	LS	100	588	64.1	526	795	0.878	12	16	19.2
DS	LS	100	294	76.0	526	584	0.953	12	12	14.9
DS	LS	100	294	82.6	526	115	0.993	12	22	19.9

† Experimental device (RS = ring shear and DS = Direct shear); Bed type (M = marble and LS = limestone); bed area, A; applied normal stess, σ_n; average shear stress, τ_r; ice velocity, u_s; vertical ice velocity, u_v; displacement, *Disp*; number of clasts, n_{clast}; number of striations, n_{stria}; abraded volume, V.

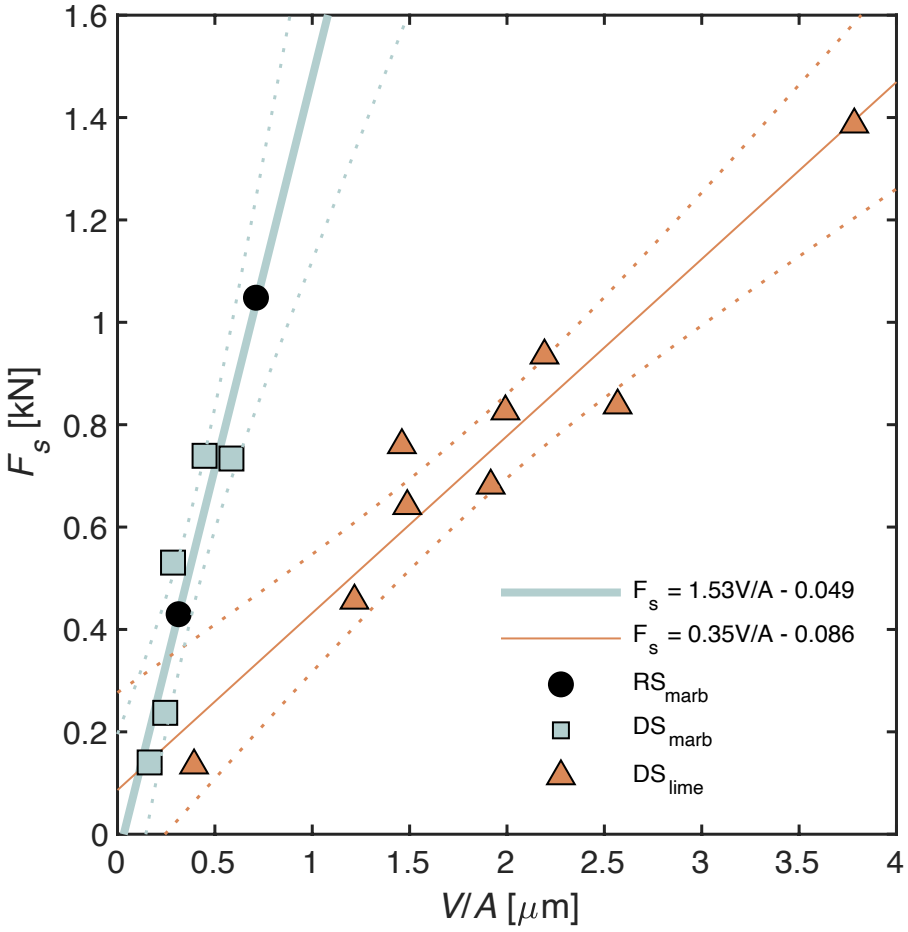

Figure 2. Abraded volume (V) normalized by the area of the bed (A) scales linearly with measured mean shear force (F_s) for both ring shear and direct shear experiments and both clast/bed types. Solid lines are ordinary least squares fits, and dashed lines represent 95% confidence intervals. Standard error of the mean for F_s is smaller than marker height.

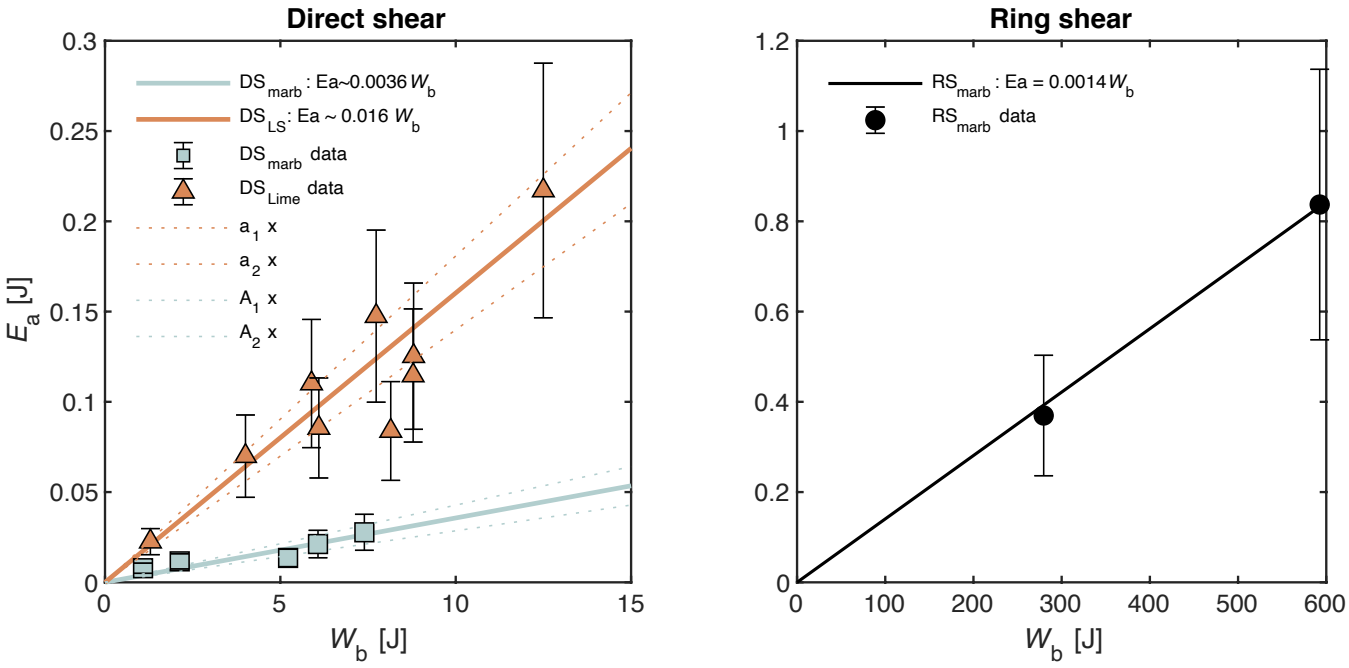

Figure 3. Energy dissipated through abrasion, E_a, increases linearly with the work done during basal slip, W_b, in the A) direct shear and B) ring shear experiments. Solid lines show the weighted least squares fit and dotted lines show the corresponding 95% confidence interval. Error bars denote the median absolute deviation for 20,000 MCMC estimates of E_a.

Since ice slid over smooth planar beds in our experiments, work done during slip, W_b, relates primarily to clast-bed interactions. We calculate W_b by subtracting background drag measured for each experimental apparatus to obtain F_s and then numerically integrating F_s with respect to displacement using the trapezoidal rule. Figure 3 presents this data as work instead of power to facilitate comparison between the RS and DS experiments, which were conducted at different slip speeds. We find abrasion energy, E_A, (Eq. 4–6) increases linearly with W_b for both bed types (Fig. 3) with approximately ~0.14–1% of W_b partitioned into abrasion. Although the estimated uncertainty is large relative to E_A for some data, the implied range represent <1% of W_b and therefore do not meaningfully impact our interpretation

4 DISCUSSION AND CONCLUSIONS

Process-based models that incorporate the fundamental physics of abrasion offer the most comprehensive look into its rates and dependencies (Melanson et al., 2013). Nevertheless, this level of complexity is not feasible for many applications, nor are the physics settled. Implementing a simplified abrasion rule that reduces the problem to one or two unknowns is therefore desirable. Typically, these parameterizations assume $\dot{A}$ scale linearly or nonlinearly with u_s (Herman et al., 2021, references therein), but cannot capture the interdependence of τ_b and u_s. By including τ_b, Hallet's (2011) basal power abrasion law aimed to increase complexity while limiting unknown parameters to a single prefactor. Our experimental work verifies his assumption that rock frictional energy scales the bedrock abrasion rate is correct for a planar bed and we find that an erodibility constant, $K \sim O(10^{-12}–10^{-10}\ \mathrm{Pa}^{-1})$ is a reasonable choice depending on lithology. Given the large hardness contrast between the soft limestone and the angular granite clasts in our experiments, our estimate for K_{ls} serves as a reasonable upper bound.

Though we observe $\dot{A}$ to scale linearly with basal power, drag in our experiments occurred solely from clast/bed interactions, meaning rock friction was the primary contributor to basal shear stress (i.e. $\tau_b \approx \tau_r$). Glacier beds on the other hand have roughness that obstructs ice flow over a wide range of length scales (Anderson, 2014; Woodard et al., 2021). For till-free regions of the bed, resistance to motion is the summed contribution of drag related to viscous deformation and regelation around bed obstacles, $\tau_{ice,}$ and subglacial rock friction (i.e. $\tau_b = \tau_{ice} + \tau_r$). Few constrains exist regarding the relative influence of these two mechanisms, but it undoubtedly depends on bed geometry, slip speed, effective stress, and controls on the contact

force. Model results by Iverson et al. (2019) demonstrated that rock friction did not substantially alter the form of the sliding law for ice sliding on a sinusoidal bed but did increase the magnitude of τ_b. This increase was not strictly linear due to the interplay between cavity geometry and associated controls on F_n. Data presented in their Figs. 7–9 imply $\tau_b u_s = a(\tau_r u_s)^b$, where a ≈ 0.0003–0.2, $b \approx 0.6$–0.9, and a and b increase with increasing clast size or decrease with increasing bed roughness. They calculate F_n, however, using Hallet's (1979) derivation, which subsequent experimental work by Thompson et al. (2020) showed is partially incorrect, meaning further work is needed to constrain the contribution of $\tau_r u_s$ to $\tau_b u_s$ for rough beds. However, as a first approximation for regions with undulating topography, Eq. 3 could be modified to

$$\dot{A} = KCa(\tau_r u_s)^b, \tag{7}$$

where a and b are likely on the lower end of the range implied by their model results.

The linearity we observe between V_a/A and F_s (Fig. 2) signals at a potential method to empirically constrain the proportionality between $\tau_r u_s$ and $\tau_b u_s$. Abraded volume for hard-bedded glaciers may be extrapolated from suspended sediment yields in select cases if subglacial sediment storage is negligible on annual timescales. Knowing i) the relationship between V_a/A–F_s, ii) the area of the catchment, and iii) annual volume of suspended sediment, one can infer integrated τ_r induced by abrading clasts. This would represent a minimum since it does not account for the frictional resistance of non-abrading clasts in contact with the bed, but it could be compared to values of τ_b derived from surface velocities. A source of uncertainty is the percentage of suspended fines produced through comminution versus abrasion when debris abrades beds of the same lithology, which has been suggested to be ~50% of the total volume (Zoet et al. 2013b). Such a study could provide valuable insight into the general magnitude of clast/bed friction, and

perhaps shed light on the discrepancy between high τ_r recorded in-situ (Cohen et al. 2005) and the generally low friction observed in ring shear experiments (Thompson et al., 2020; our Figure S3).

Lastly, we find the percentage of W_b dissipated through abrasion in our experiments was >10x lower than Metcalf's (1979) estimate at Nisqually Glacier. The root of this discrepancy is not clear, though we note most of our variables were measured directly whereas many aspects of their calculation had large uncertainties. Nevertheless, our value for limestone aligns with estimates for faults where the energy dissipated through crushing and gouging rock is ~1% total work done during slip (Fulton and Rathbun, 2011). The rest of W_b was partitioned to other dissipative or radiative processes such as frictional heat generation or elastic radiated energy. Given this miniscule expenditure, it is not necessary to consider abrasion in parameterizations of glacial slip in ice sheet models; however, over geologic timescales, it can dramatically shape glaciated terrain through erosion.

ACKNOWLEDGMENTS

The authors thank Stefanie Dodge and the Wisconsin Natural History Survey for their help with the grain size analysis; Hiroki Sone and Maciej Trzeciak for their insight regarding the CCNBD and UCT experiments; and Neal Lord and Peter Sobel for designing the ring shear device and data collection software. This work is supported by NSF **2017185.**

REFERENCES

Anderson, R.S., 2014, Evolution of lumpy glacial landscapes: Geology, v. 42, p. 679-682. doi.org:10.1130/G35537.1.

Andrews, J.T., 1972, Glacier power, mass balances, velocities and erosion potential: Zeitschrift fur Geomorphologie, v. 13, p. 1-17l.

Benn, D.I. and Evans, D.J., 2014, Glaciers & Glaciation: Routledge. p. 261-332.

Boulton, G.S., 1982, Processes and patterns of glacial erosion: In *Glacial geomorphology*, p. 41-87, Springer, Dordrecht.

Cohen, D., Iverson, N.R., Hooyer, T.S., Fischer, U.H., Jackson, M. and Moore, P.L., 2005, Debris-bed friction of hard-bedded glaciers: Journal of Geophysical Research: Earth Surface, v. 110. doi:10.1029/2004JF000228

Drewry, D.J., 1986, *Glacial geologic processes*. E. Arnold.

Fulton, P.M. and Rathbun, A.P., 2011, Experimental constraints on energy partitioning during stick–slip and stable sliding within analog fault gouge: Earth and Planetary Science Letters, v. 308, p. 185-192, doi:10.1016/j.epsl.2011.05.051.

Hansen, D.D. and Zoet, L.K., 2019, Experimental constraints on subglacial rock friction: Annals of Glaciology, v. 60, p. 37-48, doi:10.1017/aog.2019.47

Hallet, B., 1979, A theoretical model of glacial abrasion. Journal of Glaciology, v. 23, p. 39-50, https://doi.org/10.3189/S0022143000029725.

Hallet, B., 2011, Glacial erosion assessment: Nuclear Waste Management Organization Report NWMO DGR-TR-2011, 18.

Hallet, B., Hunter, L. and Bogen, J., 1996, Rates of erosion and sediment evacuation by glaciers: A review of field data and their implications: Global and Planetary Change, v. 12, p. 213-235, doi:10.1016/0921-8181(95)00021-6.

Hansen, D.D. and Zoet, L.K., 2022, Characterizing sediment flux of deforming glacier beds: Journal of Geophysical Research: Earth Surface, v. 127(4), p. e2021JF006544, doi: 10.1029/2021JF006544.

Herman, F., De Doncker, F., Delaney, I., Prasicek, G. and Kopes, M., 2021, The impact of glaciers on mountain erosion: Nature Reviews Earth & Environment, v. 2, p. 422-435, • doi:10.1038/s43017-021-00165-9.

Iverson, N.R., 1991, Morphology of glacial striae: implications for abrasion of glacier beds and fault surfaces: Geological Society of America Bulletin, v. 103, p. 1308-1316, https://doi.org/10.1130/0016-7606(1991)103<1308:MOGSIF>2.3.CO;2.

Iverson, N.R., Helanow, C. and Zoet, L.K., 2019, Debris-bed friction during glacier sliding with ice–bed separation: Annals of Glaciology, 60, p. 30-36, doi:10.1017/aog.2019.46.

Keller, C.B., Husson, J.M., Mitchell, R.N., Bottke, W.F., Gernon, T.M., Boehnke, P., Bell, E.A., Swanson-Hysell, N.L. and Peters, S.E., 2019. Neoproterozoic glacial origin of the Great Unconformity: Proceedings of the National Academy of Sciences, v. 116, p. 1136-1145, doi:10.1073/pnas.1804350116.

Melanson, A., Bell, T. and Tarasov, L., 2013, Numerical modelling of subglacial erosion and sediment transport and its application to the North American ice sheets over the Last Glacial cycle: Quaternary Science Reviews, v. 68, p. 154-174, doi.org:10.1016/j.quascirev.2013.02.017.

Metcalf, R.C., 1979, Energy dissipation during subglacial abrasion at Nisqually Glacier, Washington, USA: Journal of Glaciology, v. 23, p. 233-246, doi:10.3189/S0022143000029865.

Molnar, P. and England, P., 1990, Late Cenozoic uplift of mountain ranges and global climate change: chicken or egg?: Nature, v. 346, p. 29-34, https://doi.org/10.1038/346029a0.

Nye, J.F., 1957, The distribution of stress and velocity in glaciers and ice-sheets: Proceedings of the Royal Society of London. Series A. Mathematical and Physical Sciences, v. 239, p. 113-133, doi:10.1098/rspa.1957.0026.

Nye, J. F.,1976, Water flow in glaciers: Jökulhlaups, tunnels and veins: Journal of Glaciology. V. 17. P. 181-207, doi:10.3189/S002214300001354X

Raymo, M. E., & Ruddiman, W. F., 1992, Tectonic Forcing of Late Cenozoic Climate. Nature, 359, p. 117-121. http://dx.doi.org/10.1038/359117a0.

Stevens, N.T., Roland, C.J., Zoet, L.K., Alley, R.B., Hansen, D.D. and Schwans, E., 2022, Multi-decadal basal slip enhancement at Saskatchewan Glacier, Canadian Rocky Mountains: Journal of Glaciology, p.1-16, doi:10.1017/jog.2022.45.

Thompson, A.C., Iverson, N.R. and Zoet, L.K., 2020, Controls on subglacial rock friction: Experiments with debris in temperate ice: Journal of Geophysical Research: Earth Surface, v. 125, p. e2020JF005718, doi:10.1029/2020JF005718.

Ugelvig, S.V. and Egholm, D.L., 2018, The influence of basal-ice debris on patterns and rates of glacial erosion: Earth and Planetary Science Letters, v. 490, p. 110-121, doi:10.1016/j.epsl.2018.03.022.

Weertman, J., 1957, On the sliding of glaciers: Journal of Glaciology, v. 3, p. 33-38, doi: 10.3189/S0022143000024709.

White, W.A., 1972, Deep erosion by continental ice sheets: Geological Society of America Bulletin, v. 83, p. 1037-1056, doi.10.1130/0016-7606(1972)83[1037:DEBCIS]2.0.CO;2.

Woodard, J.B., Zoet, L.K., Iverson, N.R. and Helanow, C., 2021, Variations in Hard-Bedded Topography Beneath Glaciers: Journal of Geophysical Research: Earth Surface, 126, p. e2021JF006326. doi.:10.1029/2021JF006326.

Zoet, L.K., Carpenter, B., Scuderi, M., Alley, R.B., Anandakrishnan, S., Marone, C. and Jackson, M., 2013b, The effects of entrained debris on the basal sliding stability of a glacier: Journal of Geophysical Research: Earth Surface, v. 118, p. 656-666, doi.org.10.1002/jgrf.20052.

Supplemental material for "Chapter 3: Subglacial abrasion rates scale with rock-frictional energy during basal slip

DD Hansen[1], J Brooks[1], LK Zoet[1], NT Stevens[1], L Smith[1], C Bate[2], B Jahnke[2]

[1]*Department of Geoscience, University of Wisconsin-Madison, 1215 W. Dayton St., Madison, Wi, 53715*

[2]*Department of Geological Engineering, University of Wisconsin-Madison, 1415 Engineering Dr., Madison, Wi, 53706*

Contains Supplemental Texts:

- S1 Direct Shear: experimental protocol
- S2 Ring shear: experimental protocol
- S3 Measuring abraded volume
- S4 Grain size distribution of rock gouge,
- S5 Surface Fracture Energy
- S6 Estimating E_a and associated uncertainty with a Monte Carlo Markov Chain approach

S1. Direct Shear: experimental protocol

We conducted glacial abrasion experiments using an ELE International direct shear device with a custom sample chamber made of low-thermal conductivity fiberglass (Fig. S1), following the methodology of Hansen and Zoet (2019). Beds of two different lithologies (oolitic Indiana limestone and marble, sized 10 x 10 cm) were slid beneath debris-laden temperate ice over a range of bed-normal forces. When sourcing granitoid clasts from till, carbonate clasts

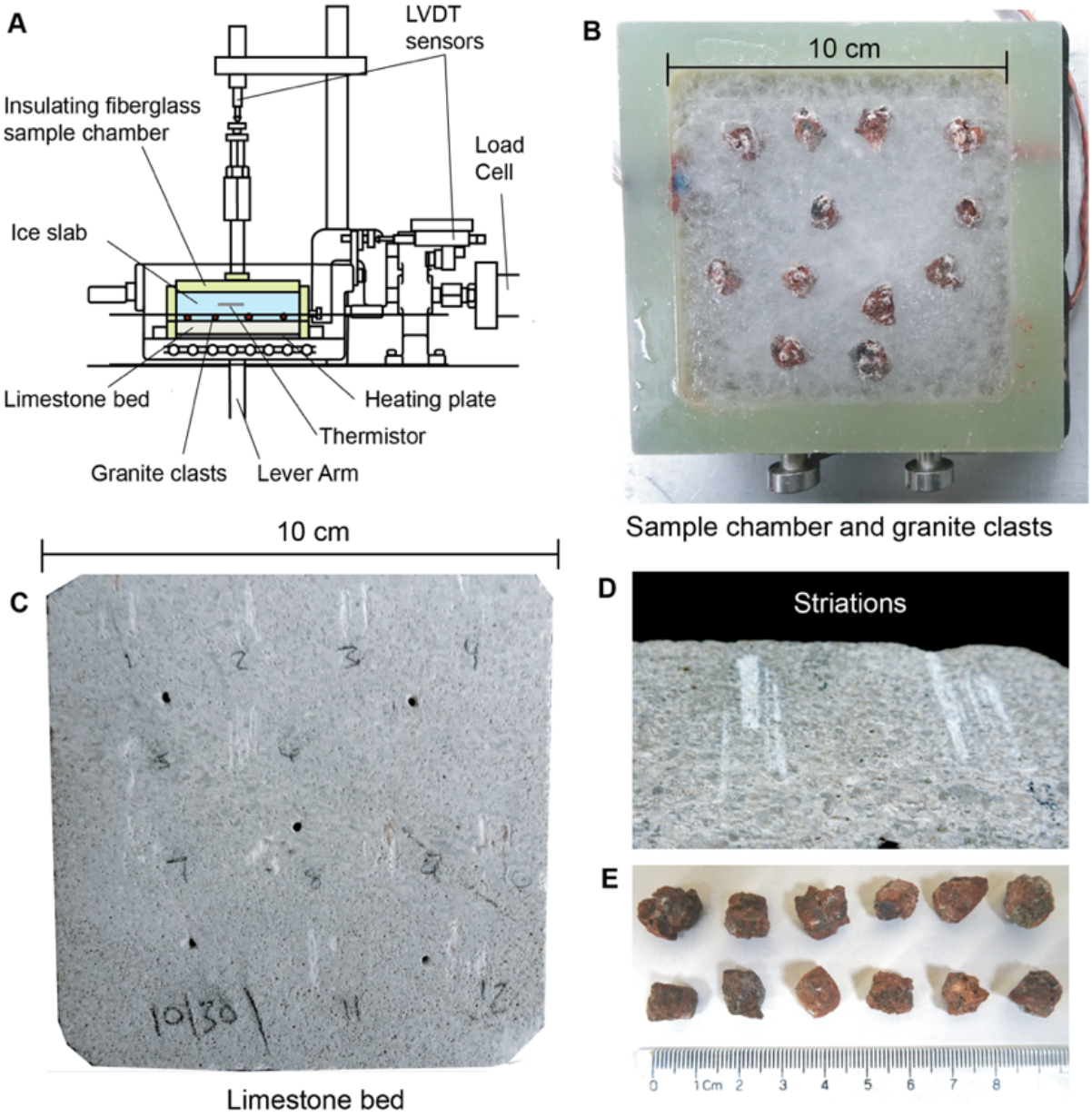

Figure S1. (a) A schematic of the modified direct shear device, (b) debris-laden ice within the insulating sample chamber, (c) a typical limestone bed at the conclusion of an experiment (note that multiple striations are common for a single abrading rock), (d) striations, and (e) 12 representative granite clasts used in our experiments. Figure copied from Hansen and Zoet (2019).

were identified through an acid reaction test and visual inspection and subsequently discarded. Clasts diameters were approximately equal or less than one-tenth the width of the sample chamber and less than half its height to avoid boundary effects (Head, 1989). Further details concerning the direct shear device and the experimental protocol can be found in Hansen and Zoet (2019). Table 1 lists the boundary conditions implemented in these experiments. Values for shear stress τ_r (or shear force, $F_s = \tau_r A$) reported herein represent mean values calculated from the measured drag over the full slip displacement. Normal stresses (σ_n) for the direct shear are applied by weights hung from a lever arm and therefore constant. For each apparatus, we measured a background drag for clean ice, and then subtracted it from the measured shear stress to isolate rock friction ($0.1216\sigma_n$ for limestone and $0.0372\sigma_n$ for marble).

S2 Ring shear: experimental protocol

We also conducted two abrasion experiments in a cryogenic, temperature-controlled ring shear device, hereafter denoted RS1 and RS2 (Fig. S2). This apparatus better approximates subglacial drainage conditions compared to the direct shear and effectively allows unlimited displacement. (For a detailed description of this device refer to Hansen and Zoet, 2022.) We slid rings of debris-laden temperate ice over marble beds at prescribed normal stresses, basal melt rates, and slip speeds (see Table 1 for boundary conditions). For these two experiments, we closely followed the experimental protocol of Thompson et al. (2020) with the following minor deviations: i) we sequentially built our ice ring in 5–10-cm-thick layers of snow and deionized water instead of 1–2 cm-thick layers, and ii) we estimated vertical drawdown solely using the linear variable displacement transducer (LVDT) without tracking beads. Between RS1 and RS2,

there were two differences in methodology. First, in RS2, we froze clasts to the bed in a ~3-mm-thick film of ice

before constructing the ice ring, which may have caused more clasts to be in contact with the bed than in RS1. Second, we recorded temperature in RS2 with four glass bead thermistors installed in the base, 8 in the outer sample chamber walls, and a GEC temperature probe mounted in the glycol/water bath at the level of the ice bed interface; whereas RS1 only had the GEC probe. Since we are not concerned with the relationship between specific controls such as melt rate or debris concentration and abrasion in this study, these differences do not impact on our interpretation.

In poorly drained environments, debris-bed contact forces are primarily controlled by the pressure gradients in thin water films surrounding entrained clasts and the real area of contact between the clasts and the bed, with negligible contribution from ice pressure (Thompson et al., 2020). In similar ring shear experiments, Thompson et al. (2020) reported that ice pressure exerted no influence on contact forces, even though the chamber was connected to atmospheric pressure. They did, however, observe a nonlinear dependence on basal melt rate. Accordingly, we increased the contact force in RS2 relative to RS1 by raising the temperature in the circulating glycol-water bath. This induced a higher melt rate at the interface, and a LVDT recorded drawdown as the sample contracted. For both experiments, the slip speed of basal ice equaled 37.5 m/yr at a radial position that divided the bed into two equal areas (r_{cl} = 0.22 m). Similar to Thompson et al., 2020, the grain size distribution was comprised of three size classes with the number of clasts in each corresponding to a fractal dimension of 2.9 (Hooke and Iverson, 1995). This resulted in an areal debris concentration at the bed of 10% and ~4%

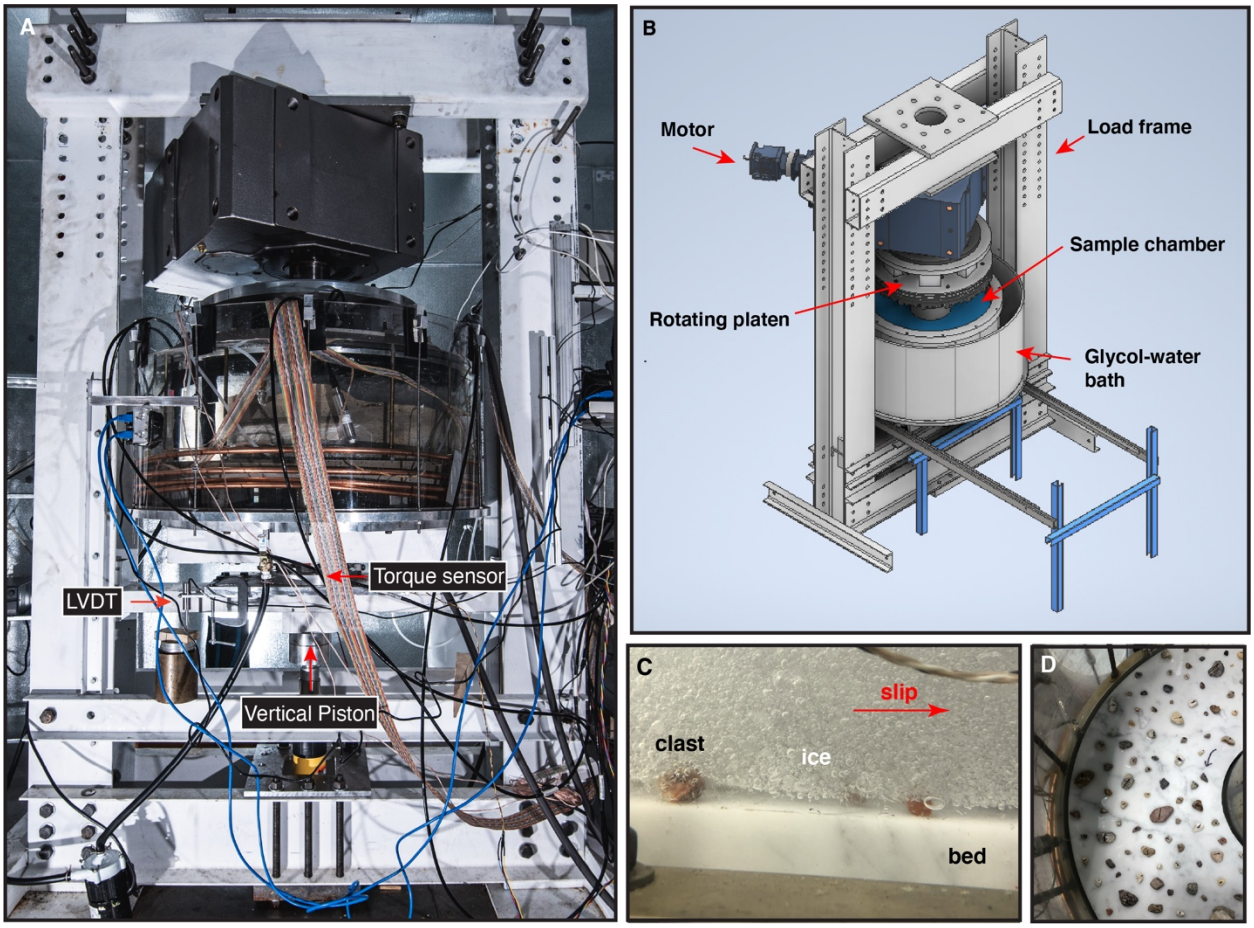

Figure S2. A) Photo of the cryogenic ring shear device. B) design schematic (modified from Dodge et al, 2022). C) clast entrained in ice slipping on a marble bed at the outer sample chamber wall. D) Clasts arrayed on marble bed prior to building the ice ring. (Photo credit: Ethan Parrish)

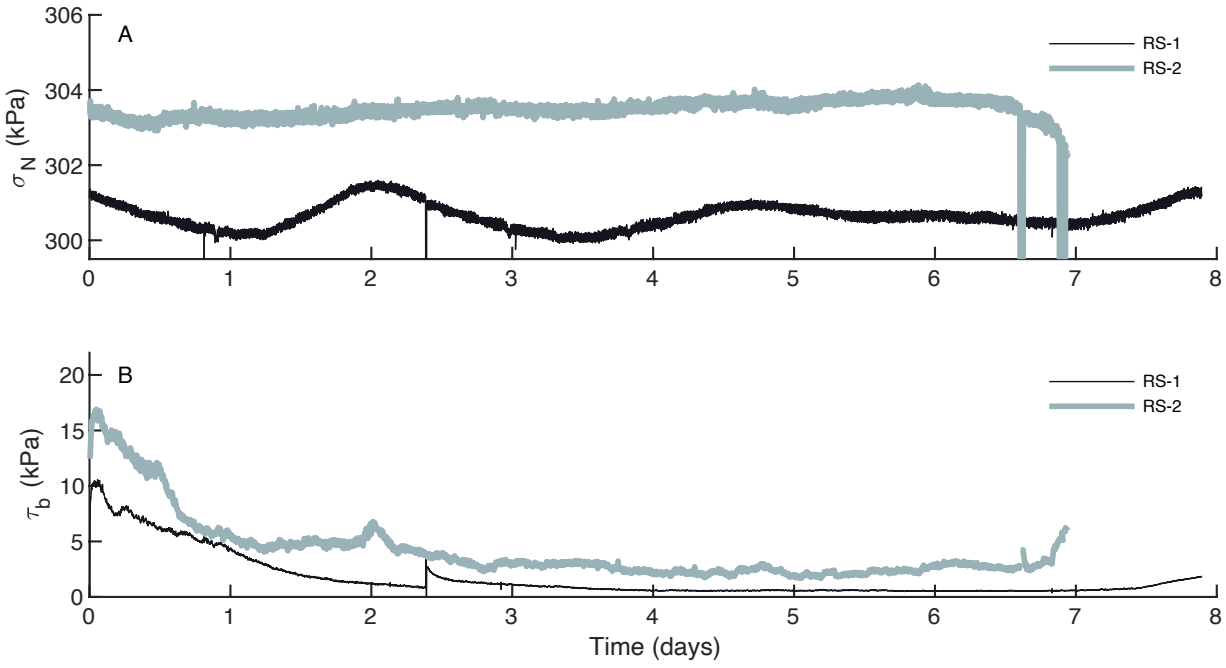

Figure S3. Experimental time series for the two ring shear experiments, RS1 and RS2, showing a) the normal stress applied by a hydraulic ram, and b) the basal shear stress recorded during slip, τ_r. The x-axis denotes time since slip was initialized by rotating the ice ring.

volumetric concentration assuming clasts were similarly spaced across the bed (Thompson et al., 2020). In total, we used 212 small clasts (5-12 mm diameter), 72 medium clasts (12-20 mm), 25 large clasts (20-28 mm). All clasts were igneous or metamorphic and sourced from the same Horicon till.

S3. Measuring abraded volume

We scanned striations with a Nanovea JR 25 white light profilometer to create digital elevation models (DEM) of the abraded surface (Fig. 1). Abraded volume for each surface DEM was calculated using proprietary functions in Nanovea's analytic software, Professional 3D 7.4. To process a scanned surface, we applied the following workflow: First we corrected for any

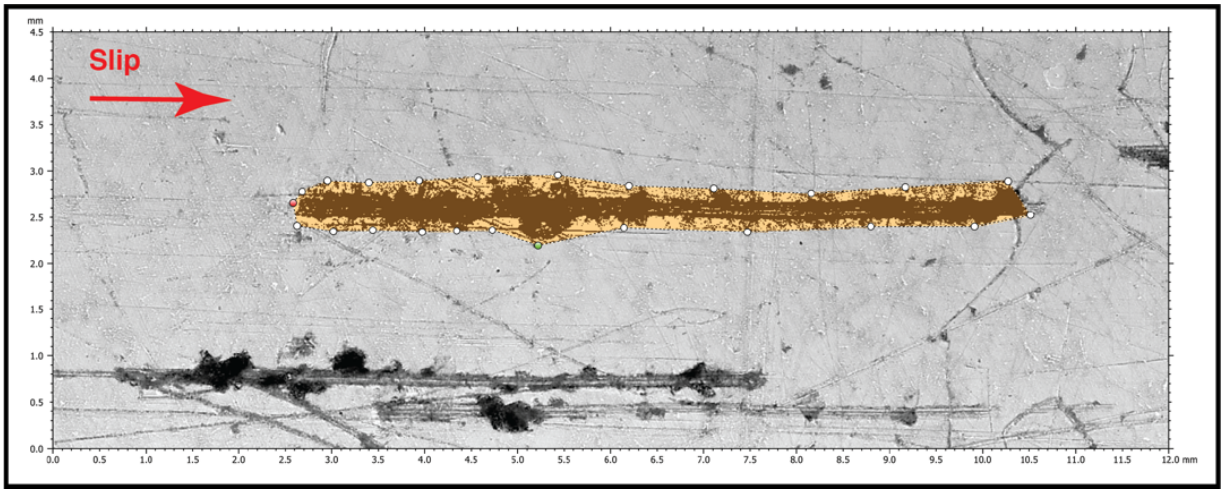

Figure S4. Striations produced in a marble-bed direct shear experiment that illustrate our method for calculating abraded volume. A contour is manually defined around the striation (dotted outline) and a plane is fit to the surrounding surface using ordinary least squares regression. The dark brown shaded region in this contour represents the region where surface elevation lies below this plane (a "hole") and the light orange shading represents the region where surface lies above ("a peak"). Abraded volume is then the volume of the void defined by the projected area of the holes, the elevation of this plane and the underlying surface.

systematic background tilt introduced by unevenness of the scanning platform with a leveling function, which fit a plane to the surface using least squares regression and then subtracted it from the DEM point by point. Next, we identified and replaced spurious points with values interpolated from neighboring valid points. Volume and projected area for each striation were then calculated by manually defining a contour around the boundaries of a striation, fitting a least squares plane to points outside of the user-defined contour, and then subtracting the difference between the surface defined by the contour and this plane (Fig. S4).

The time required to scan the marble ring shear bed at the highest resolution is prohibitive (~1300 hours per experiment), so we scanned the entirety of the marble bed at a lower resolution (20 μm X 150 μm) to mitigate the time cost. Pixel dimensions, however,

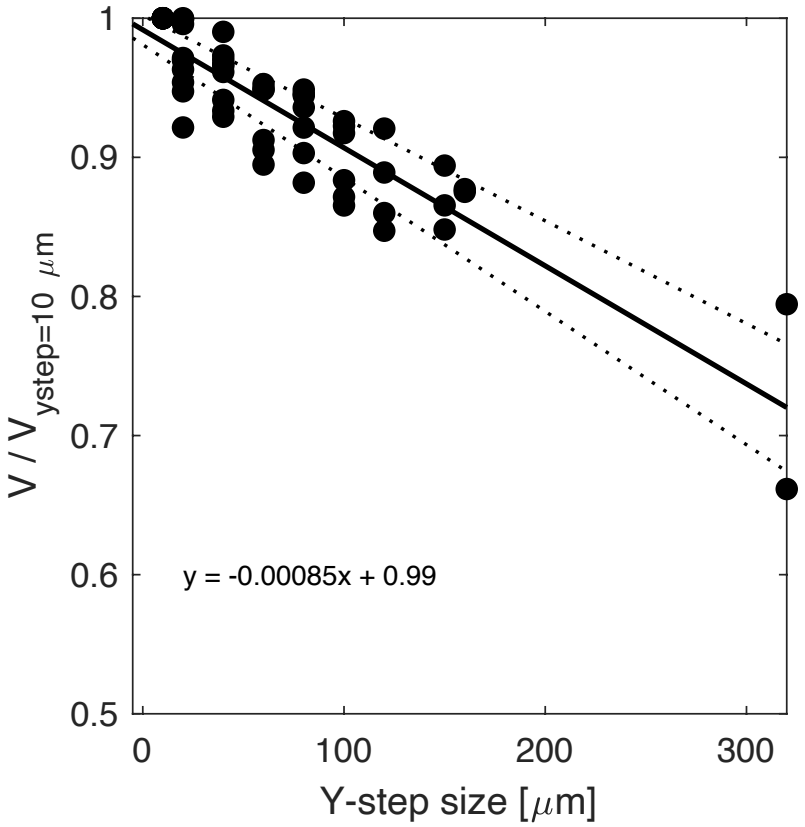

Figure S5. Abraded volume, *V*, normalized by *V* at y-step = 10 μm, decreases with increasing y-step resolution. Solid black line represents the ordinary least squares regression with associated standard error for the slope 5.5 x 10^{-5} μm^{-1} and $r^2 = 0.82$. Dashed lines represent 95% confidence intervals for the fit.

increase at lower resolutions, smoothing roughness elements on the surface and producing more diffuse striation boundaries—factors which both affect the final volume calculation. To correct for this degradation, we estimated the relationship between pixel dimension and abraded volume for a set of nine striations. Individual features were scanned repeatedly at varying y-step sizes (10–150 μm) with a constant x-step of 20 μm. We calculated abraded volume for each set of striations using the method outlined above and normalized each set of volumes by the set value for y-step = 10 μm. An ordinary least squares solution suggests estimated striation volume decreases with y-step resolution at a rate of ~ -0.085% per μm increase in y-step size (Fig. S5).

Therefore, we adjusted our measured volumes by +11.01% in line with a resolution of 20 μm X 20 μm, which was the resolution for most of the direct shear marble bed scans.

S4. Grain size distribution of rock gouge

Surface area created through abrasion is proportional to the grain size distribution of the gouge particles created during shear (Eq. 5). In our experiments, the particulate produced in a single experiment was minuscule and typically below the threshold mass needed for standard grain size analysis, so we conducted a separate set of tests in the direct shear to produce this material (~0.2 g per sample). Clasts (similar to those used in the main experiments) were encased in slabs of epoxy and slid over beds of both lithologies under a range of vertical stresses. Shear resistance in these runs arose solely from rock-rock on friction as no other portion of the slab contacted the bed. Following each experiment, we dusted the abraded slab to collect the particulate on its surface and repeated this process until we obtained the required mass. Between each run, we rotated the epoxy slabs or sanded the bed to prevent clasts from repeatedly abrading the same striation. Grain size distribution of the gouge was analyzed via laser diffraction in a Malvern Mastersizer 2000E at the University of Wisconsin-Milwaukee following standard procedure. Prior to the analysis, particles were dispersed in a 0.05% sodium phosphate solution for at least 24 hours to deflocculate aggregates and then sonicated for at least ten seconds. In total, we collected two gouge samples for the marble bed type (at σ_n = 78.4 and 156.8 kPa), and three samples for the limestone bed (at σ_n = 70, 137, 250 kPa). The grain size distribution for each sample was analyzed three times (Figure S6). We observed no clear trend between the imposed loads and the resultant grain size distribution (Fig. S6). Median grain diameter, D_{50}, ranged between 39–319 μm for the limestone gouge and 39–319 μm for the marble. Differences

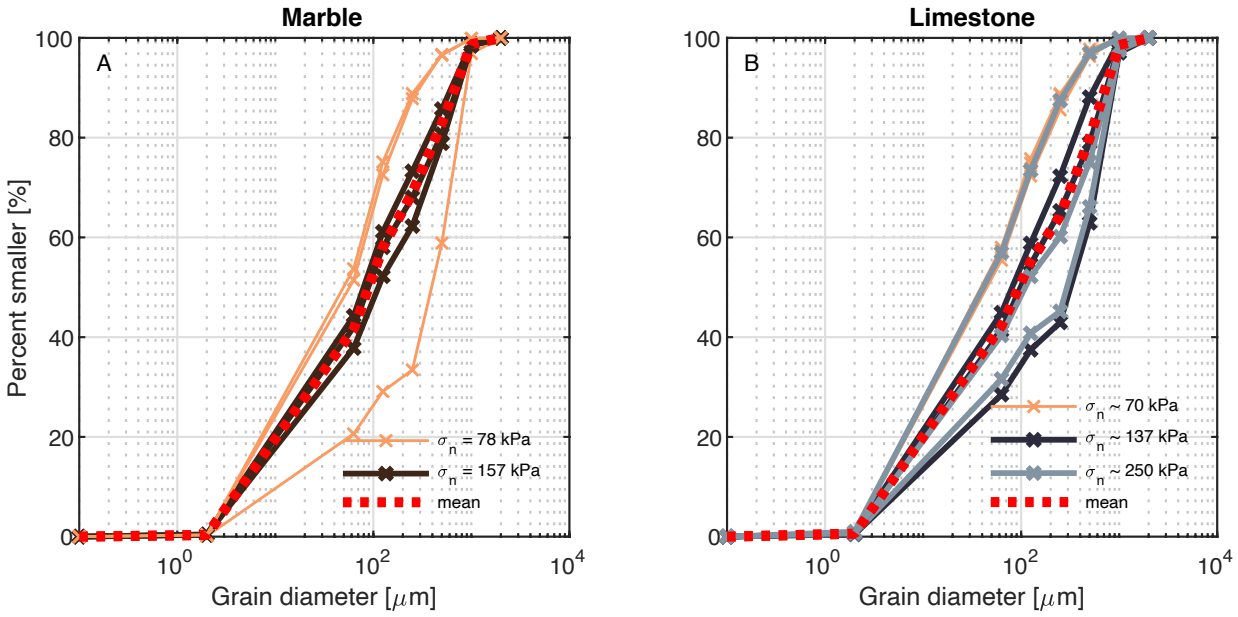

Figure S6. Grain size distribution of the gouge particles produced in epoxy/clast abrasion runs for the marble (a) and limestone (b) beds under different normal loads, F_n. Red dotted curves in each plot show the mean GSDs.

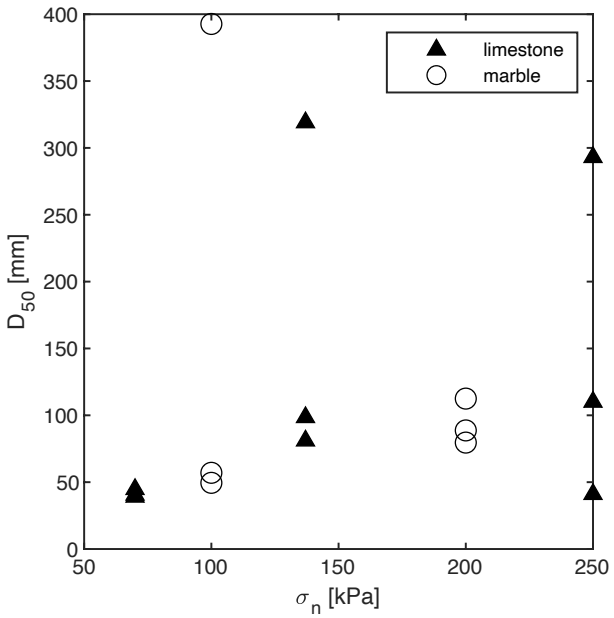

Figure S7. Median grain diameter, D_{50}, versus applied normal stress, σ_n, in the epoxy/clast direct shear runs for the marble (white circles) and limestone (black triangles) beds.

in D_{50} >100 μm measured for a single sample reflects the variable tendency of sand size particles to be mobilized during individual measurements. Therefore, for our purposes in Eq. 5, we opted to randomly sample distributions of each rock type when estimating E_a from 20,000 Monte Carlo Markov Chain simulations (S6). Mean distributions are denoted by dashed red lines in Fig. S6 with D_{50} = 89 μm and 95 μm for marble and limestone gouge respectively.

S5. Surface Fracture Energy

Surface fracture energy of polycrystalline rocks, γ, is the energy consumed during the creation of a new surface per unit area (Nakayama, 1965; Zhang and Ouchterlony, 2022). Irwin (1956) proposed a model for fracture that includes an energy release rate parameter, G, to represent the available energy for an increment of crack extension. When G reaches a critical value—i.e. $G_c = 2\gamma$—fracture occurs (Anderson, 2005). Likewise, Mode I fracture toughness (K_c) describes a material's resistance to fracture propagation (Fowell, 1994) and relates similarly to G_c under mode I loading (Soboyejo, 2003):

$$G_c = \frac{K_c^2}{E'} \tag{S1}$$

where $E' = E/(1-\nu^2)$ for plane strain, E is Young's Modulus, and ν is Poisson's ratio. It therefore follows that under Mode I loading:

$$\gamma = \frac{K_c^2(1-\nu^2)}{2E}. \tag{S2}$$

From this equivalency, we estimated γ for our limestone and marble beds for Eq. 3. We measured K_c with Cracked Chevron Notched Brazilian (CCNBD) disc tests and E and ν with unconfined uniaxial compression tests (UCT). Both sets of experiments were conducted in a

GCTS servo-controlled triaxial apparatus following suggested ISRM protocol (ISRM, 1979; ISRM, 1995).

CCNBD tests methods

We successfully conducted CCNBD tests on four limestone and seven marble samples. Fowell (1994) defined K_c as

$$K_c = \frac{F_{max}}{B \cdot \sqrt{r}} Y_m^*, \quad \text{(S3)}$$

where B and r are the thickness and radius of the notched disc respectively, and F_{max} is the normal force applied to the disc at the moment of failure. Y_m^* is the minimum critical stress intensity factor, which for valid disc geometries is

$$Y_m^* = u \cdot e^{v \cdot \alpha_1}, \quad \text{(S4)}$$

where u and v are geometrical constants listed in ISRM (1995), $\alpha_1 = a_1/R$, and a_1 is one half the outer notch length. Cylindrical discs were cut from longer cores using a high-precision saw and notched with a Dremel tool (Fig. S7A). Average sample dimensions were $2r \sim 37.9$ mm, $B \sim 12.7$ mm, with an outer notch length $2a_1 \sim 26.2$ mm and inner notch length of $\sim 2a_0 \sim 10.4$ mm. We identified F_{max} by plotting applied load versus lateral displacement and identifying the point where an initial stress drop coincided with rapid lateral expansion (Fig. S7 C–D). Parameters u and v were interpolated from the table of values provided in ISRM (1995) to correspond to our specific disc dimensions. Table S1 presents these results.

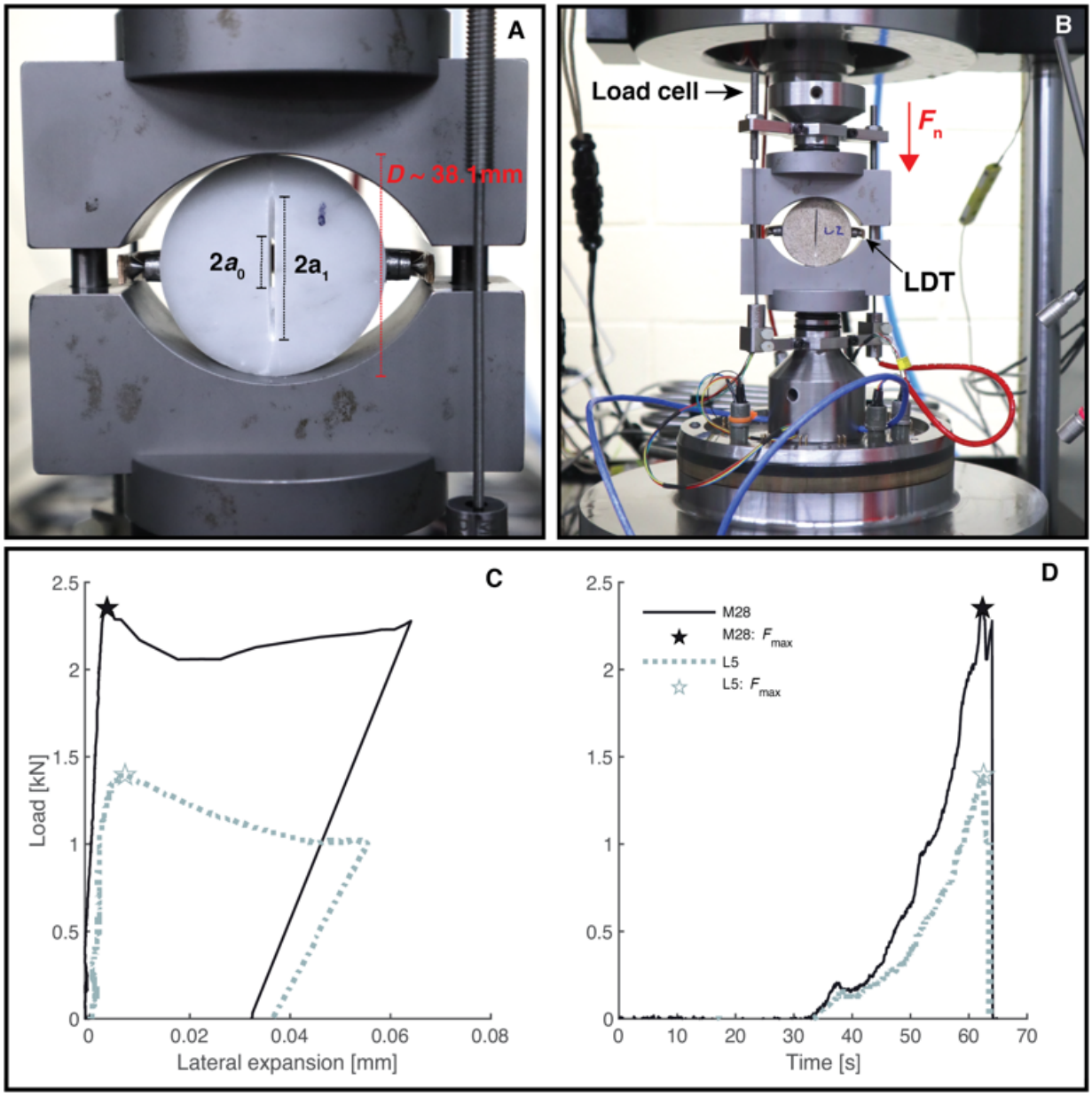

Figure S7. A) Notched disc for CCNBD seated in the loading frame. B) a vertical force, F_n, is applied to the sample, while an LDT records horizontal displacement and an LVDT measures vertical displacement. C) Applied load versus lateral expansion for a representative limestone run (grey dashed line) and a marble run (solid black line). The stars denote the point of failure, F_{max}, identified as the point where a sudden drop in load occurs simultaneously with rapid horizontal expansion. D) A timeseries of the applied load for the same two runs. Stars represent the same F_{max} in S7 C.

Table S1. Summary of CCNBD tests parameters and results†

ID	Rock	$2a_0$ [mm]	$2a_1$ [mm]	B [mm]	$2r$ [mm]	F_{max} [kN]	K_c [MPa m$^{0.5}$]
L3	LS	11.72 ± 0.051	26.77 ± 0.051	12.68 ±0.013	37.90 ± 0.064	1.42	0.788
L4	LS	11.74 ± 0.013	26.66 ± 0.88	12.84 ± 0.089	37.89 ± 0.013	1.35	0.738
L5	LS	11.56 ± 0.076	26.02 ± 0.13	12.65 ± 0.051	37.91 ± 0.10	1.395	0.745
L6	LS	7.45 ± 0.076	25.54 ± 0.99	13.03 ± 0.051	37.85 ± 0.013	1.174	0.573
M1_1	M	10.6 ± 0.3	26 ± 0.0	12.5 ± 0.0	38.0 ± 0.0	2.12	1.17
M1_3	M	10.23 ± 0.1	26 ± 0.0	12.5 ± 0.0	38. 0 ± 0.0	1.797	1.17
M2_1	M	9.13 ± 0.07	26.19 ± 0.65	12.53 ±0.04	37.97 ± 0.3	2.1	1.12
M2_3	M	10.40 ± 0.32	26.48 ± 0.58	12.95 ± 0.02	37.91 ± 0.04	2.8	1.47
M2_6	M	10.81 ± 0.15	26.59 ± 0.32	13.38 ± 0.08	37.89 ± 0.00	2.103	1.09
M2_7	M	10.31 ± 0.34	26.04 ± 0.16	12.12 ± 0.04	37.89 ± 0.03	1.715	0.952
M2_8	M	10.58 ± 0.22	26.08 ± 0.9	12.44 ± 0.18	37.88 ± 0.02	2.352	1.29

†Sample ID; Rock type (M=marble and LS=limestone); Outer notch length, $2a_0$; inner notch length $2a_1$; sample thickness, B; sample diameter, $2R$; load at moment of fracture, F_{max}; minimum critical stress intensity factor, Y_m^*; Fracture toughness, K_c. For parameters $2a_0$, $2a_1$, B; and $2R$, "±" denotes the range of 2–3 measurements.

Estimating Young's Modulus and Poisson's ratio

We conducted unconfined uniaxial compression tests to determine the elastic parameters of the marble and limestone beds (Young's modulus, E, and Poisson's ratio, v). We tested three cylindrical samples for each bed type (average length: $L \sim 50.60$ mm, and average outer diameter: $D \sim 25.55$ mm; see Table S2), which were cored from larger blocks and ground to size on a precision surface grinder (Fig. S8A). Prior to loading, samples were jacketed in a polyolefin heat shrink for platen stability and fixed between two steel loading platens with a 25.4 mm diameter. Two diametrically opposed LVDTs mounted parallel to the sample's axis recorded longitudinal compression, while two lateral displacement transducers (LDTs) mounted at 90˚offsets recorded horizonal expansion as the rock deformed (Figure S8 B). At the start of each test, a constant seating stress of 1 MPa was applied to the sample over a 60 s interval. Axial load was then increased at a constant rate of 40 MPa/min, while we monitored for signs of sample failure. Once the sample begin to yield plastically, axial load was ramped down to 1 MPa at a

rate of -40 MPa/min (except for sample Marb1, which was ramped down over a ten-minute interval instead). Two limestone samples ultimately failed under load whereas the rest remained intact.

For a linear elastic rock under uniaxial compression, $E = \sigma_n/\varepsilon_l$, where σ_n is the applied normal stress, $\varepsilon_l = \Delta L/L$ is the longitudinal strain, and ΔL is the change in sample length. By convention, σ_n and ε_l are negative in compression. We take the average of the two LVDT records for ΔL and subtract the deformation of the loading platens using a pre-determined fit. Poisson's ratio is $v = -\varepsilon_t/\varepsilon_l$, where $\varepsilon_t = \Delta D//D$ is the transverse strain, and ΔD is the change in sample diameter (average of two LDT records). We estimate E and v by computing the ordinary least squares solution over an interval where the relationships are approximately linear (i.e. no plastic deformation) (Figure S8 C–F). For marble, the mean values were $E_m = 54.13 \pm 6.050$ and $v_m = 0.3342 \pm 0.0523$, and for limestone $E_{ls} = 23.02 \pm 10.02$ and $v_{ls} = 0.2196 \pm 0.1189$ (where "±" denotes the range of three samples). Table S2 presents these results.

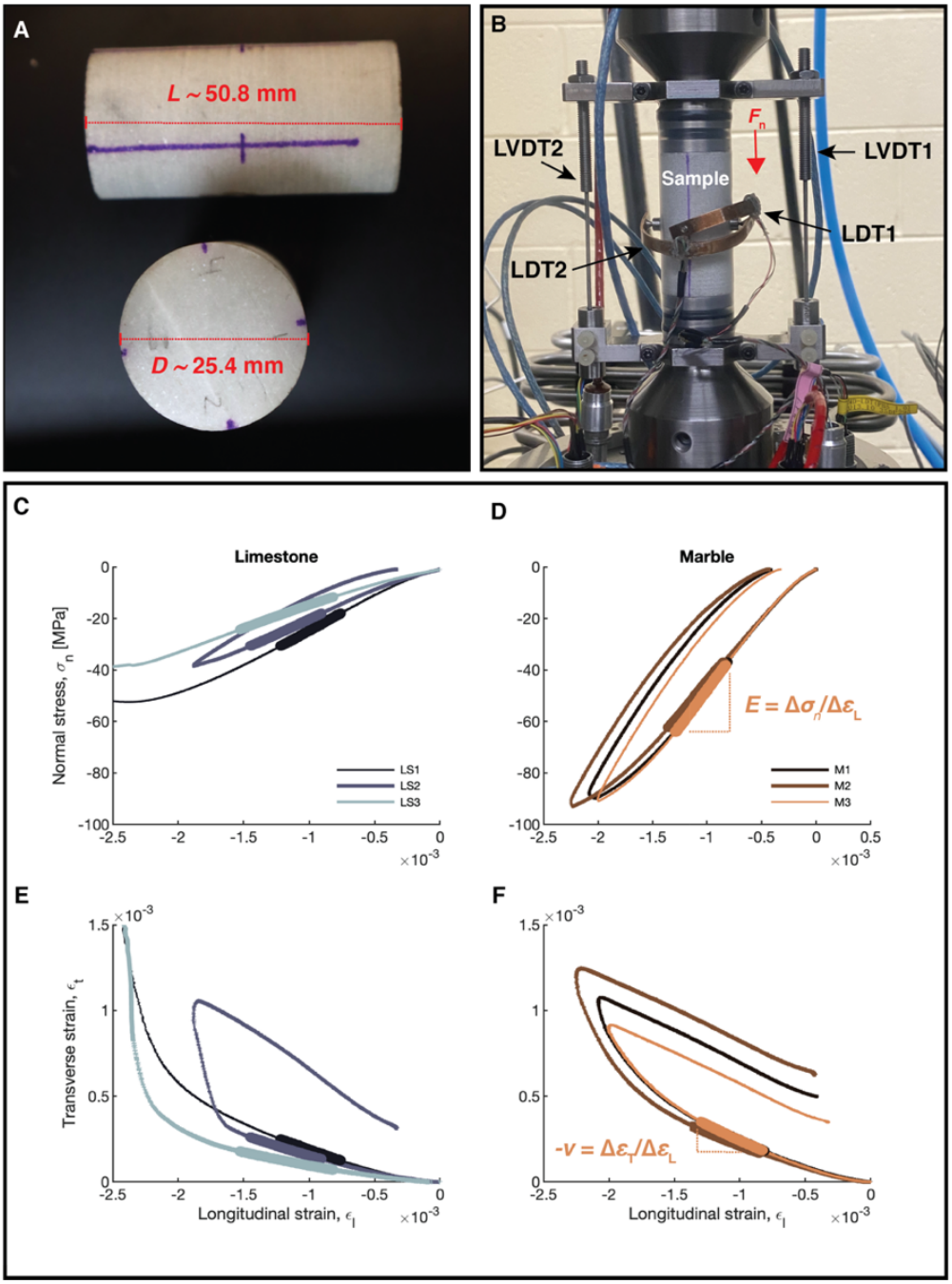

Figure S8. A) sample dimensions, B) the loading apparatus applied a vertical load, F_n, to the sample while LVDTs and LDTs measure vertical and horizontal displacement, respectively. C–D) Longitudinal strain, ε_l, versus applied normal stress, σ_n. E–F) Longitudinal strain versus transverse strain. Thicker line segments show the interval over which E and ν were estimated with an ordinary least-squares solution.

Table S2. Summary of unconfined uniaxial compression tests and results.

ID	L [mm]	D [mm]	*E* [GPa]	*v*
LS1	50.44 ± 0.05	25.37 ± 0.24	27.82 ± 0.02115	0.2705 ± 0.0003043
LS2	50.53 ± 0.05	25.55 ± 0.01	23.44 ± 0.01465	0.2366 ± 0.0002521
LS3	50.61 ± 0.02	25.49 ± 0.14	17.80 ± 0.01033	0.1516 ± 0.0001862
Marb1	50.60 ± 0.05	25.60 ± 0.16	55.42 ± 0.02213	0.3424 ± 0.0002639
Marb2	50.81 ± 0.03	25.71 ± 0.02	50.46 ± 0.02509	0.3039 ± 0.0002449
Marb3	50.65 ± 0.03	25.58 ± 0.15	56.51 ± 0.02931	0.3562 ± 0.0002739

†Sample ID; Rock type (Marb=marble and LS=limestone); Sample length, L; Sample diameter, D; Young's modulus, E; and Poisson's ratio, v . For parameters L and D, "±" denotes the range of four and three measurements, respectively. Otherwise "±" states the standard error associated with the ordinary least squares solution.

S6. Estimating E_a and associated uncertainty with a Monte Carlo Markov Chain approach

Calculations of E_a using Eq. 3 Eq. 3–5 and S1–S4 incorporated numerous experimental measurements with small sample sizes (generally $n \leq 5$); however, each sample has known observational uncertainties. To propagate experimental uncertainties through this system of equations, we used a Monte Carlo Markov Chain (MCMC) approach with 20,000 simulations for each experimental geometry and lithology, randomly drawing perturbed values from prior distributions of individual measurements (Table S3). We described observed parameter values using uniform distributions for length-scale measurements (L, D, $2a_0$ $2a_1$, $2r$, and B), scaling distributions by relevant measurement precision, along with roughness prefactor R (Eq. 5), which ranges from 3–5 (Fulton and Rathbun, 2011). For parameter estimates E and v obtained from linear regression of experimental data, we used Gaussian prior distributions centered on the regression slope value (F_n–ΔL and ΔD–ΔL space) and scaled by the modeled slope variance. The slopes were combined with estimates of D, L, and A to obtain E and v. Perturbed grain-size

values were drawn from empirical distributions in Fig. S6, and all prior distributions are documented in the data repository with repeat measurements. Rather than averaging repeat measurements, we drew perturbed samples from individual, randomly selected measurement prior distributions. We also randomly selected a single K_c, E, and ν from the set of possible values computed for the sample set (i.e. marble versus limestone). This mitigated biases in the posterior distributions of E_a that could arise from small sample averaging. Posterior distributions of E_a are all skewed right (Fig. S9), so we use the median and median absolute deviation (MAD) to calculate reported values in the main text.

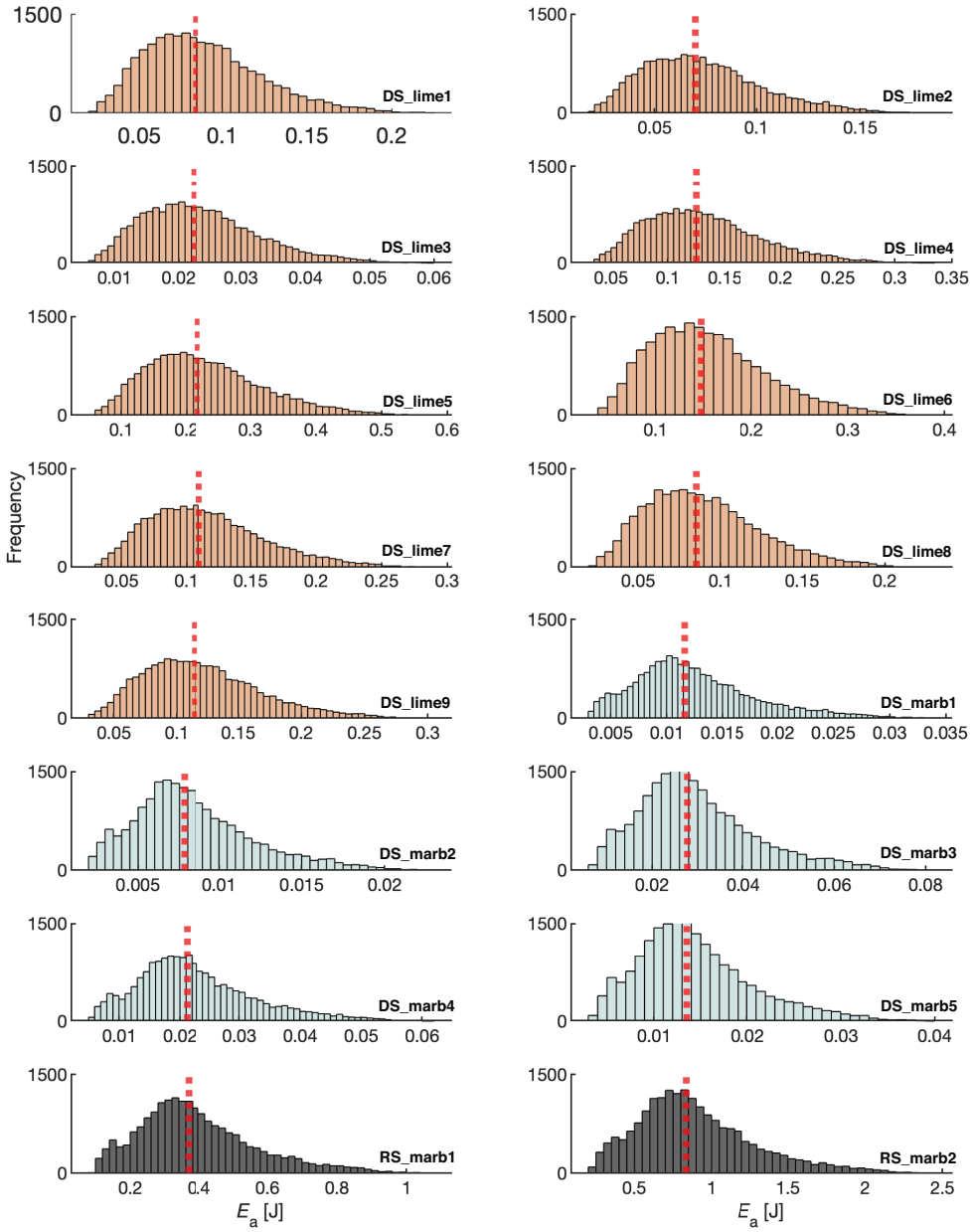

Figure S9. Frequency of estimated abrasion energy, E_a, computed with 20,000 MCMC runs for the limestone-bed direct shear experiments (copper), marble-bed direct shear experiments (grey), and marble-bed ring shear experiments (black). Red dashed lines denote the median of the set.